

**QUASI 1D METAL OXIDE
NANOSTRUCTURES FOR ELECTRONIC
AND OPTO-ELECTRONIC APPLICATIONS**

**A THESIS SUBMITTED TO THE
UNIVERSITY OF PUNE
FOR THE DEGREE OF DOCTOR OF PHILOSOPHY**

**IN
PHYSICS**

**BY
MEENAL SUDHEER DEO**

**DR. (MRS.) JYOTI P. JOG
(RESEARCH GUIDE)**

**DR. SATISHCHANDRA B. OGALE
(RESEARCH CO-GUIDE)**

**POLYMER SCIENCE AND ENGINEERING DIVISION
PHYSICAL AND MATERIALS CHEMISTRY DIVISION
NATIONAL CHEMICAL LABORATORY
PUNE – 411 008
INDIA**

NOVEMBER 2013



सीएसआयआर-राष्ट्रीय रासायनिक प्रयोगशाला

(वैज्ञानिक तथा औद्योगिक अनुसंधान परिषद)

डॉ. होमी भाभा मार्ग, पुणे - 411 008. भारत



CSIR-NATIONAL CHEMICAL LABORATORY

(Council of Scientific & Industrial Research)

Dr. Homi Bhabha Road, Pune - 411008. India

CERTIFICATE

This is to certify that the work presented in the thesis entitled "QUASI 1D METAL OXIDE NANOSTRUCTURES FOR ELECTRONIC AND OPTO-ELECTRONIC APPLICATIONS" by MEENAL SUDHEER DEO, submitted for the degree **Doctor of Philosophy in Physics** was carried out under our supervision at the Polymer Science and Engineering Division and Physical and Materials Chemistry Division, National Chemical Laboratory, Pune, 411008, India. All the materials from other sources have been duly acknowledged in the thesis.

Dr. (Mrs.) Jyoti P. Jog

(Research Guide)

Dr. Satishchandra Ogale

(Research co-Guide)

Date: 14/11/2013

Place: NCL, Pune



Communication
Channels

NCL Level DID : 2590
NCL Board No. : +91-20-25902000
EPABX : +91-20-25893300
: +91-20-25893400

FAX

Director's Office : +91-20-25902601
COA's Office : +91-20-25902660
COS&P's Office : +91-20-25902664

WEBSITE

www.ncl-india.org


Declaration by the candidate

I hereby declare that the thesis entitled “QUASI 1D METAL OXIDE NANOSTRUCTURES FOR ELECTRONIC AND OPTO-ELECTRONIC APPLICATIONS” submitted for the degree Doctor of Philosophy in Physics to the University of Pune, has been carried out by me at the Polymer Science and Engineering Division, and Physical and Material Chemistry Division of National Chemical Laboratory, Pune under the joint supervision of Dr. (Mrs.) Jyoti P. Jog and Dr. Satishchandra B. Ogale. Such material as has been obtained by other sources has been duly acknowledged in this thesis. The work is original and has not been submitted in part or full by me for any other degree or diploma to other University.

Date: 14/11/2013

National Chemical Laboratory

Pune – 411 008


Meenal Sudheer Deo
(Research Student)

DEDICATED
TO
MY
MOTHER...



Acknowledgements

There are so many people, whose support, encouragement and inspiration are very much obligatory to accomplish major achievements in life, especially, if it involves the elements of fulfilling one's cherished dreams. For me, this thesis is such an important destiny and I am indeed indebted to lot of people for their well wishes and blessings for completing this journey. I take this opportunity to acknowledge and extend my sincere gratitude towards all those people who have been involved, directly or indirectly, to make the research work described in this thesis possible.

I am grateful to my research Guide Dr. Jyoti P. Jog for her guidance throughout this work. It has been a great privilege to work under her able guidance and valuable scientific advice over the past four years. I also wish to express my heartfelt gratitude to her for motherly care, and friendly support throughout this journey.

I would also like to express my deepest gratitude to Dr. Satishchandra Ogale, my co-supervisor for giving me an opportunity to work in his dynamic laboratory environment. His innovative thinking, consistent guidance and highly spirited attitude have inspired me to conduct and complete my doctoral research quite efficiently. He has not only grafted my scientific skills and knowledge but also molded me into a better person. He has been a constant source of motivation and encouragement throughout these years. It has been a pleasure to work in a group led by his never ending energy, ideas and motivation.

I am really grateful to both Dr. Jog and Dr. Ogale for their critical comments and tremendous efforts in preparing this dissertation. I would also like to thank Dr. Sarika, Rohan, Mandakini, Shruti, Anil and Vishal for their help in the improvement in this thesis.

I would like to acknowledge Department of Science and Technology (DST) and Council for Scientific and Industrial Research (CSIR) for the scholarships provided for my research work, and last but not the least, the Govt. of India for the research fellowship and travel grants. I express my sincere thanks to Dr. S. Sivaram, former Director of CSIR-NCL, Dr. Sourav Pal, Director, CSIR-NCL, the Head, Polymer Science and Engineering Division, and Dr. Anil Kumar, the Head, Physical and Materials Chemistry Division, for providing the infrastructure and facilities for

performing research at CSIR-NCL and for their whole-hearted help and constant support from the very first days at National Chemical Laboratory. I would like to thank the technical and non-technical staff of the Physical and Materials Chemistry division and Center for Materials Characterization for their help. I would also like to thank all the staff members of Students Academic Office for their time-to-time help.

I take this opportunity to thank Dr. S. I. Patil, Head, Department of Physics, University of Pune for his scientific and administrative inputs. A special thanks to Prof. Beatrice Hannoyer and Prof. Xavier, University of Rouen, France for providing TEM facility and Dr. B. B. Kale Centre for Materials for Electronics Technology (C-MET), Pune for the FESEM facility.

I deeply acknowledge my laboratory friends and seniors Dr. Hrushikesh, Dr. Sneha, Dr. Kashinath, Dr. Anup, Dr. Mukesh, Dr. Sarfraj, Dr. Rajesh, Dr. Vivek Dhas, Dr. Subas, Dr. Tushar, Dr. Prasad, Dr. Abhimanyu, Dr. Sarika, Dr. Arif, Dr. Vivek Antad, Dr. Harish, Dr. Ashish, Dr. Parvez, Mandakini, Shruti, Reshma, Lily, Onkar, Vishal, Datta, Anil, Abhik, Rohan, Dipti, Dhanya, Pooja, Shraddha, Mukta, Rounak, Pradeep, Aniruddha, Satyawar, Satish, Yogesh, Wahid, Umesh, Subhra, Ketaki, Nilima, Aparna, Minakshi, Rupali, Divya, Pravarthana, Upendra, Sambhaji, Sumit, Kush, Tanya, Chetan, Prashant, Dhanalakshmi, Sachin, Usman for providing me a wonderful working environment. I also acknowledge the support of my other divisional friends Dr. Bhaskar, Dhanraj, Joyshish and Mangesh.

I don't have words to express my feelings towards my Aai – Baba whose love, support, care and blessings have made me what I am today. My deep thanks to my sister, Amruta, who is always supportive and inspiring for me since my childhood. I would like to also thank my brother-in-law Mayuresh and my sweet little nephew Adeesh. I would also like to thank my sister's in-laws and all other relatives in Pune for providing me homely atmosphere.

I would like to take this opportunity to acknowledge all my teachers throughout my life, especially Wayangankar Madam, Marathe Madam, Dhayagude Madam and Late Dr. Dhayagude Sir, for their knowledge, inspiration, blessing and belief in me which motivated me.

It gives me an immense pleasure to thank my close friends Anuja, Garima, Deepti and Harshitha, whose love, support and guidance gave me strength to face ups and downs during this journey. I express my sincere thanks to my room-mates Deepa, Ranja, Rani, Megha, Sharada, Chayanika who made my stay in Pune memorable.

Meenal Deo

List of Abbreviations

0D	Zero- Dimensional
1D	One- Dimensional
2D	Two- Dimensional
3D	Three- Dimensional
SPR	Surface Plasmon Resonance
CNT	Carbon Nanotube
SWNT	Single Wall Carbon Nanotube
MWNT	Multi Wall Carbon Nanotube
PL	Photoluminescence
VLS	Vapor-Liquid-Solid
LED	Light Emitting Diode
DMS	Dilute Magnetic Semiconductor
CCD	Charged Coupled Device
TE	Thermoelectric
PEC	Photo-electrochemical
EMF	Electromotive Force
NHE	Normal Hydrogen Electrode
RHE	Reversible hydrogen electrode
CVD	Chemical Vapour Deposition
MBE	Molecular Beam Epitaxy
DC	Direct Current
RF	Radio Frequency
PLD	Pulsed Laser Deposition
XRD	X-ray Diffraction

FWHM	Full Width at Half Maximum
TEM	Transmission Electron Microscopy
HRTEM	High Resolution TEM
SAED	Selected Area Electron Diffraction
SEM	Scanning Electron Microscopy
FESEM	Field Emission SEM
SE	Secondary Electrons
BSE	Backscattered Electrons
AES	Auger electron spectroscopy
EDAX / EDS	Energy Dispersive analysis of X-rays
CB	Conduction Band
VB	Valence Band
UV-VIS	Ultraviolet-Visible
IR	Infra-red
DRS	Diffuse Reflectance Spectroscopy
UHV	Ultra High Vacuum
CV	Cyclic Voltammetry
IS	Impedance Spectroscopy
XPS	X-ray Photoelectron Spectroscopy
EIS	Electrochemical Impedance Spectroscopy
ITO	Indium Tin Oxide
I-V	Current – Voltage
FE	Field Emission
MO	Methyl Orange
F-N	Fowler-Nordheim
LSV	Linear Sweep Voltammogram

Abstract

The research and development of electronic and optoelectronic devices leads to direct impact on our modern society, as most of them are used in day-to-day life. The rapid miniaturization and compact architecture of these devices has led to tremendously enhanced performance and cost reduction, but are restricted mainly to silicon based devices. Hence, the demand for other earth-abundant and cost effective materials with improved functionality and enhanced performance is growing. Metal oxides are considered to be promising candidates in this respect because the range of electronic and optical properties they support is remarkable. Also, quasi-1D nanostructures have emerged as an important class of materials which facilitate, through controlled growth, making of novel electronic and optoelectronic devices. The work on quasi-1D metal oxide nanostructures has witnessed considerable expansion during the past few years with fields such as field effect transistors, p-n junction diodes, sensors, solar energy conversion, etc. acquiring centre stage. Formation of heterojunction using such quasi-1D metal oxides widens the application domain even further due to the integration of properties of both the materials and novel interface effects.

In the research work presented in this thesis, we have focused on the synthesis of p-type cuprous oxide (Cu_2O) nanoneedles and their heterojunctions with ZnO and TiO_2 using simple synthesis protocols. These materials have been studied for a few applications covering important current areas such as photo-sensing, field electron emission, photocatalysis and water splitting for hydrogen generation, etc. This background forms the brief introduction to the thesis and is presented in **Chapter 1**.

In **Chapter 2**, a brief overview of the synthesis and thin film deposition methods for metal oxides are presented. Furthermore, a general outline of the instruments and methods used for the characterization of these nanomaterials for their potential applications are also presented.

Chapter 3 discusses the synthesis of cuprous oxide nanoneedles directly on copper substrate. The details of the further studies for photodetector application by making p- Cu_2O nanoneedles/n-ZnO nanorods flip-chip heterojunction device have also been discussed. We have also observed that the nanowire heterojunction photo-

response is far stronger as compared to a thin film heterojunction made of the same materials.

To further improve the properties of the heterojunction, an interesting $\text{Cu}_2\text{O}/\text{ZnO}$ hetero-nanobrush assembly has been fabricated, which is discussed in **Chapter 4**. The hetero-nanobrushes show excellent field electron emission performance and photocatalytic activity. The detailed mechanism is studied and discussed in this chapter.

In **Chapter 5**, we have presented and discussed the results of photo-electrochemical water splitting using cuprous oxide nanoneedles on copper as photocathode. The effect of TiO_2 capping of Cu_2O nanoneedles on the photo-electrochemical activity is also discussed in this chapter.

Chapter 6 summarizes the work described in this thesis by presenting the salient features of the work and also mentioning the possible avenues for future work.

Table of Contents

Chapter 1: Introduction.....	1 - 42
1.1 Introduction.....	2
1.2 Properties of Nanomaterials.....	3
1.2.1 Electronic Properties.....	3
1.2.2 Optical Properties.....	5
1.2.3 Surface effects.....	7
1.2.4 Magnetic Properties.....	8
1.3 Quasi 1D Materials.....	9
1.3.1 Properties of quasi 1D nanomaterials.....	11
1.3.2 Synthesis methods for quasi 1D nanostructures.....	14
1.3.3 Heterojunctions.....	17
1.4 Metal Oxide Nanomaterials.....	20
1.4.1 Cuprous Oxide (Cu ₂ O).....	21
1.4.2 Zinc Oxide (ZnO).....	22
1.5 Applications of Metal Oxide Nanoparticles.....	23
1.5.1 Photodetector.....	24
1.5.2 Field Emission.....	26
1.5.3 Photocatalysis.....	28
1.5.4 Photo-electrochemical (PEC) Water Splitting.....	30
1.6 Outline of the thesis.....	34
1.7 References.....	35
Chapter 2: Experimental Methods and Characterization Techniques.....	43 – 63
2.I Deposition Techniques.....	44
2.I.1 Electrochemical Synthesis.....	44
2.I.2 Pulsed Laser Deposition (PLD).....	45
2.II Materials Characterization Techniques.....	48
2.II.1 X-Ray Diffraction (XRD).....	49
2.II.2 Scanning Electron Microscopy (SEM).....	51
2.II.3 Transmission Electron Microscopy (TEM).....	53

2.II.4 UV-VIS Spectroscopy.....	55
2.II.5 Field Emission Measurements.....	57
2.II.6 Cyclic Voltammetry (CV).....	58
2.II.7 Impedance Spectroscopy (IS).....	59
2.III References.....	62

Chapter 3: Strong Photo-Response in a Flip-Chip Nanowire p-Cu₂O/n-ZnO heterojunction.....64 – 80

3.1 Introduction.....	65
3.2 Experimental.....	66
3.2.1 Synthesis of Cu ₂ O Nanoneedles on Copper and ZnO nanorods on ITO/Glass.....	66
3.2.2 Thin Film Deposition of Cu ₂ O & ZnO by PLD.....	67
3.2.3 Characterization.....	67
3.3 Results and Discussion.....	68
3.3.1 Study of copper in basic solution.....	68
3.3.2 Characterization of Cu ₂ O Nanoneedles.....	70
3.3.3 Electrical properties of p-Cu ₂ O/n-ZnO heterojunction.....	72
3.4 Conclusion.....	79
3.5 References.....	79

Chapter 4: Cu₂O/ZnO Hetero-nanobrush: Hierarchical assembly, Field Emission and Photocatalytic Properties.....81 - 97

4.1 Introduction.....	82
4.2 Experimental Section.....	83
4.2.1 Synthesis of Cu ₂ O/ZnO hetero-nanobrush on copper.....	83
4.2.2 General Characterizations.....	84
4.2.3 Field Emission and Photocatalysis experiments.....	85
4.3 Results and Discussion.....	85
4.3.1 Characterization of Cu ₂ O/ZnO Heterostructure.....	85
4.3.2 Field Emission studies.....	88
4.3.3 Photocatalysis.....	92

4.4	Conclusion	94
4.5	References	95

Chapter 5: Evaluation of cuprous oxide nanoneedle photocathode for photo-electrochemical activity.....98 - 112

5.1	Introduction	99
5.2	Experimental	100
	5.2.1 Synthesis.....	100
	5.2.2 Characterization.....	101
	5.2.3 TiCl ₄ treatment.....	101
	5.2.4 Photoelectrochemical measurements.....	101
5.3	Results and discussion	101
	5.3.1 Characterization of Cu ₂ O nanoneedles.....	101
	5.3.2 Mott – Schottky Plot.....	104
	5.3.3 Photo-electrochemical Measurements.....	105
	5.3.4 Photo-stability of Cu ₂ O nanoneedles electrode.....	106
	5.3.5 Effect of TiO ₂ coating.....	108
5.4	Conclusion	109
5.5	References	110

Chapter 6: Conclusion and Future Scope.....113 - 117

6.1	Summary of the thesis	114
6.2	Scope for future work	115

Appendix - I: Fabrication of Anatase TiO₂ Nanofibers by Electrospinning for Dye and Quantum Dots Sensitized Solar Cells.....118 - 130

A-I.1	Introduction	119
A-I.2	Experimental	120
	A-I.2.1 Synthesis of Electrospun TiO ₂ Nanofibers.....	120
	A-I.2.2 Fabrication of photoanode for DSSC.....	121
	A-I.2.3 Deposition of CdS quantum dots.....	122

A-I.3 Results and discussion	122
A-I.3.1 Characterization of TiO ₂ nanofibers	122
A-I.3.2 Photovoltaic characterizations of DSSC	124
A-I.3.3 Characterization of CdS sensitized TiO ₂ film	127
A-I.3.4 Photovoltaic characterizations of CdS Sensitized solar cell	128
A-I.4 Conclusion	129
A-I.5 References	129

Appendix – II: A Hybrid Photodetector based on ZnO Nanorods/Agarose Gel with Giant Response in UV-Visible.....	131 – 133
---	------------------

Appendix – III: Plasmonic Au / ZnFe₂O₄ / ZnO triple heterojunction photoanode for solar photo-electrochemical water splitting.....	134 – 136
---	------------------

List of Publications	137 – 138
-----------------------------------	------------------

Chapter 1

Introduction

This chapter gives an introduction to the growing field of nanoscience and nanotechnology. We have presented an overview of recent trends in nanotechnology followed by the discussion on the properties of nanomaterials. The properties of quasi-1D nanomaterials have also been discussed, as they represent a special class in nanomaterials that form the emphasis of this thesis. Besides this, we have emphasized the use of quasi-1D metal oxide nanomaterials in various (especially optoelectronic) applications.

1.1 Introduction

Materials have always played an extremely important role in the progress of human civilization for many centuries^[1]. They have been the vehicles for translating ideas and dreams into reality by harnessing application sectors of human interest. In the last few decades ‘nanomaterials’ and various advanced material systems based thereupon have been attracting a great deal of attention of the scientific community in view of several emergent novel application domains that are getting unfolded recently.

Nanomaterials are engineered atomic and molecular structures with at least one of their dimension less than about 100 nm. Nanotechnology, which utilizes such materials, possesses tremendous potential to address many scientific and technological challenges, since the properties of these materials can be tuned by controlling their size, properties and interactions. Nanotechnology deals with the cheaper, faster and better products, by making them ‘small’, with entirely new physical phenomena of interest to science and technology^[2].

Actually ‘Nano’ is a Greek word; meaning dwarf. Mathematically a ‘Nano’ means one billionth. Thus, $1 \text{ nm} = 10^{-9} \text{ m}$. To get a sense of the nano scale, a human hair measures about 80,000 nanometers across. Another way to put this is just ten hydrogen atoms in a line make up one nanometer. Nanostructures are the smallest solid (or condensed matter) entities which are practically possible to make^[3]. The length scale comparison of different materials/entities is shown in figure 1.1. Two principal factors cause the properties of nanomaterials to differ significantly from other materials: increased surface to volume ratio and dominance of quantum effects. These factors can change or enhance chemical reactivity, and electronic, optical, mechanical, magnetic, and transport characteristics. Thus, most of the fundamental properties of materials show significant change in the nanoscale range.

The interest in nanomaterials has grown tremendously since last few years because of our increased ability and improved understanding to study and manipulate materials at smaller length scales. During the last few years, there have been more directed efforts towards controlled synthesis of inorganic/organic nanomaterials of

specific sizes, different shapes, and stoichiometric compositions, and explorations of their novel technological applications ^[4].

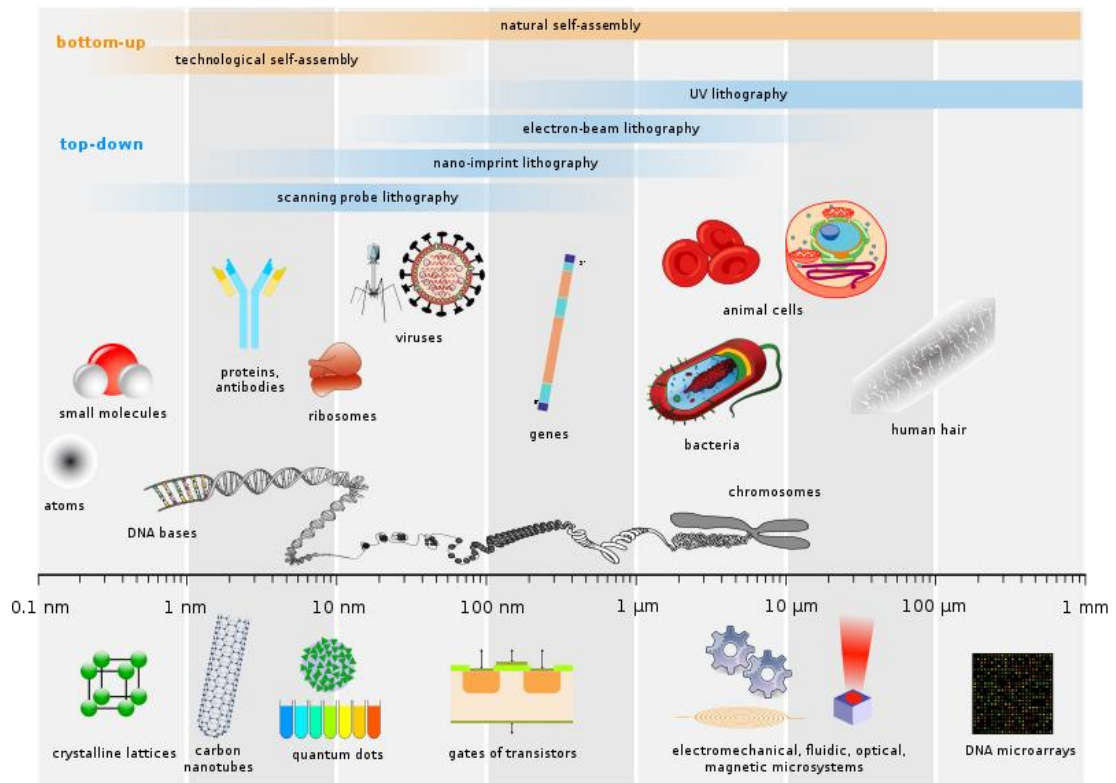


Figure 1.1: Materials on different length scales [taken with permission from Guillaume Paumier, Wikimedia Commons; ref. 3 (b)]

1.2 Properties of Nanomaterials

The wide range of physical properties afforded by size tuning of nanocrystals and their applications in electronics, optics, and bio-medicines have drawn attention of scientists from various disciplines. The changes in the properties of the materials at nanoscale are the consequences of two major effects: First, the number of surface atoms increases tremendously in nanomaterials and second, the electronic structure of the material transforms because of ‘quantum size effect’ ^[5].

1.2.1 Electronic Properties

When materials become smaller, their electronic and optical properties deviate substantially from those of bulk materials. In a bulk crystalline material, electrons occupy effectively continuous energy bands, while at the other end of the length scale represented by individual atoms and molecules the electronic states are

discrete. The electronic structure of a nanomaterial falls between these two extremes, as shown in figure 1.2. Thus, as we go from bulk to nano, the energy transactions become discrete, measured as quanta, rather than continuous as in bulk materials. This situation of fairly discrete energy levels is called quantum confinement or quantum size effect. The confinement really means confining the motion of the otherwise freely moving electrons to one or more confined dimensions ^[6].

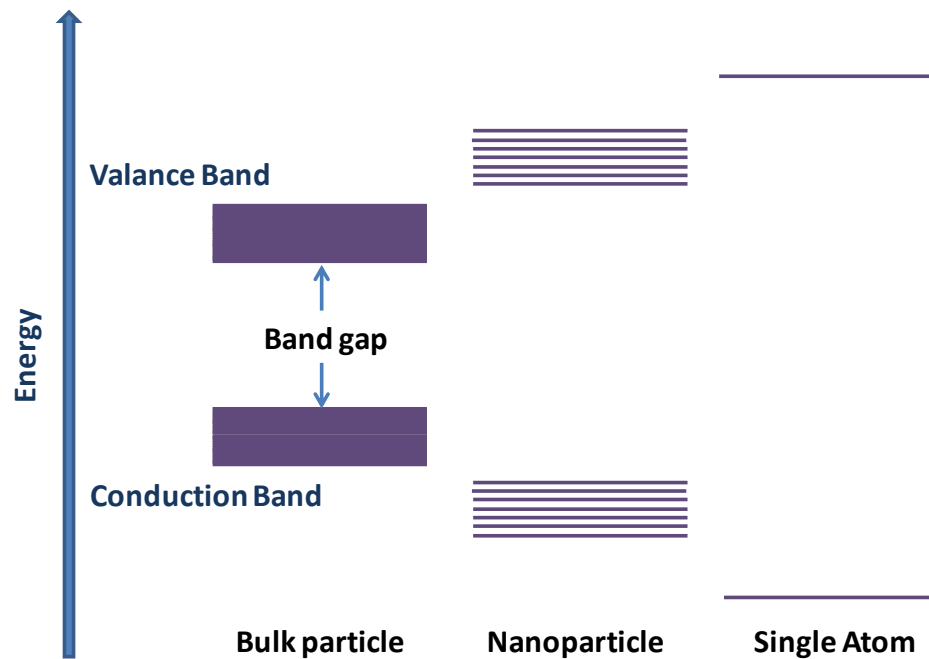


Figure 1.2: Electronic energy states for a bulk particle, a nanoparticle and a single atom

Figure 1.3 shows the density of states in (a) metal and (b) semiconductor nanocrystal. In semiconductors, the electronic and optical properties are governed by their electronic density of states and the band gap. The Fermi level lies at the center of the band, whereby the edges of the bands dominate the low-energy optical and electrical behaviour. When the particle size is decreased, the number atoms in the particle also gets decreased. The band structures in solids are formed by overlap of atomic orbitals. As the number of atoms is decreased, density of states is thus decreased and discrete energy levels result somewhat similar to atoms. Moreover due to localization over a small space (particle in a box) the allowed energy levels are pushed up. Such particle size effects are more dramatic on the nanoscale because the physical length scales for comparison are on that scale. The quantum size effect is

defined usually in terms of its Bohr exciton (bound electron-hole pair) radius. The quantum size effect dominates when particle size reaches below the material's Bohr exciton radius. For example, with the decrease in particle size the band gap of CdS increases from 2.5 to 4.5 eV. However in the case of metals, the band gap is zero due to overlap of valance and conduction bands, and the Fermi level lies at the center of the band. The relevant energy level spacings are very small and at temperatures above a few Kelvin, the electrical and optical properties are similar to those of a continuum, even in very small sizes (tens or hundreds of atoms). However, a bunch of just a few metal nanoparticles (rather clusters) can show insulating behaviour due to the changes in the electronic structure. This transition is called the size-induced metal–insulator transition.

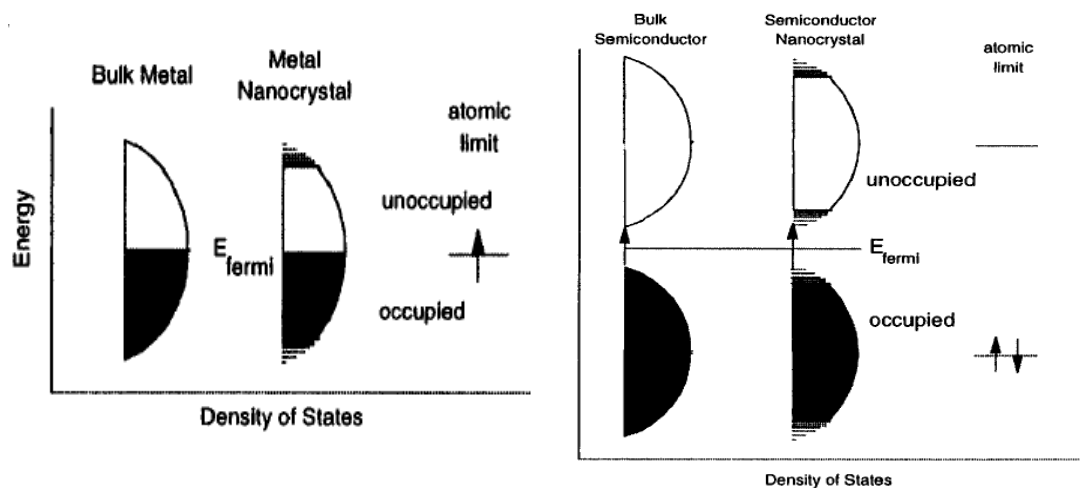


Figure 1.3: Density of states in (a) bulk metal, metal nanocrystals and (b) bulk semiconductor, semiconductor nanocrystal [Printed with permission from ACS; ref. 5]

1.2.2 Optical Properties

The optical properties of nanomaterials evolve in a very interesting manner because of their size as well as shape. The optical properties of semiconducting materials are mainly governed by their band gap. When a material is illuminated with photon of energy greater than its band gap, then by absorbing the photon an electron is excited to conduction band leaving behind a hole in valance band. These electrons and holes interact with each other due to their opposite charges and form bound pairs known as excitons. When the electron and hole recombine, energy is released (equal

to its band gap) in the form of light. This phenomenon is known as photoluminescence. Thus, the semiconductor absorbs wide range of photons but emits light wavelength equivalent to its band gap minus the exciton binding energy. As the electronic structure changes at the nanoscale, typically below the Bohr exciton radius, i.e., to a few nanometers, when the size of a semiconductor is reduced to the same order, quantum confinement effect occurs. Hence the excitonic and luminescence properties of semiconducting materials are modified depending on their size ^[7, 8]. Size tunable absorption spectra and emitted colors of CdSe quantum dots are shown in figure 1.4. In some cases, the luminescence occurs because of the enhanced surface trapped states on semiconducting nanoparticle.

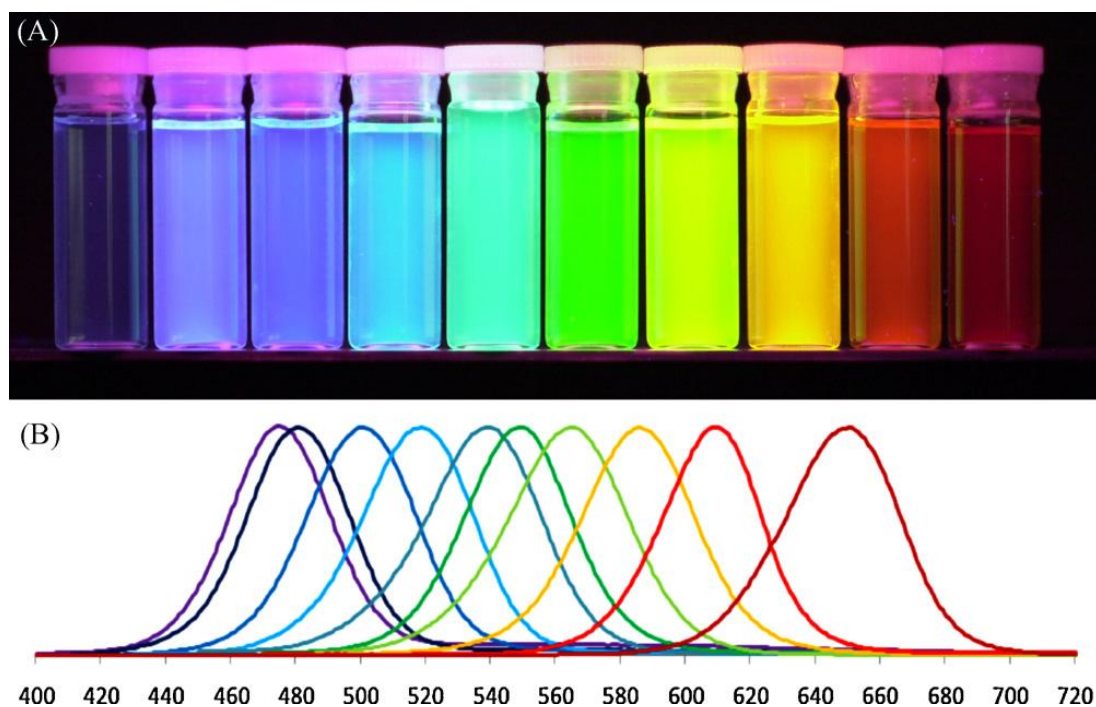


Figure 1.4: Size dependent (A) emitted colors and (B) optical absorption of CdSe quantum dots [With a permission from Elsevier; ref. 8]

Metal nanoparticles, on the other hand, show unique interaction with light. When a metal nanoparticle is irradiated with light, the electric field causes the conduction band electrons to oscillate coherently. The amplitude of this oscillation reaches to maximum at a particular frequency. This phenomenon is called as Surface Plasmon Resonance (SPR), which causes strong absorption of incident light. Noble metal (Au, Ag and Pt) nanoparticles are known to show SPR in visible and near IR region within

certain size limit of particles ^[9]. The SPR strongly depends on the shape of the metal nanoparticles. In case of nanorods, the SPR splits into two modes: longitudinal mode and transverse mode corresponding to the length of nanorod and across the diameter, respectively ^[10].

Due to these exciting optical properties, nanomaterials are used for biological detection and imaging ^[11] and several optoelectronic devices such as semiconductor light-emitting diodes, photodetectors, solar cells ^[12].

1.2.3 Surface effects

Surface atoms of a particle have fewer adjacent coordinating atoms as compared to the core atoms. Also, dangling bonds are present at the surface. Hence they are chemically more active than the core atoms in an attempt to satisfy these bonds. Due to this the surface of a material determines the material characteristics like catalytic activity, reactivity, etc. As the size of the particle decreases, a larger number of its constituent atoms occupy the surface (shown in figure 1.5) due to very high surface to volume ratio ^[6, 13].

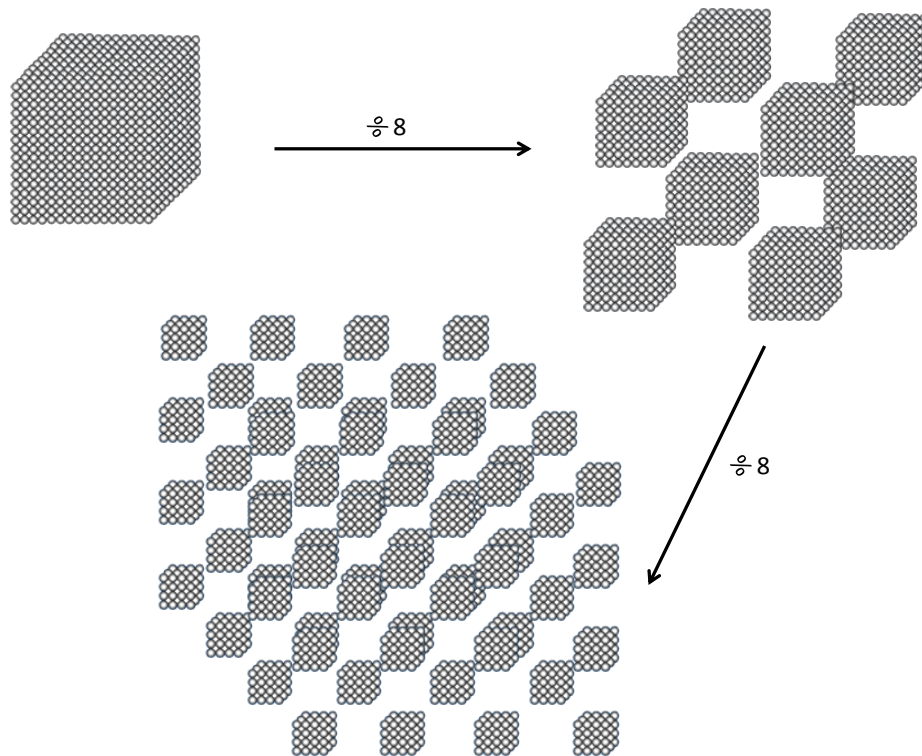


Figure 1.5: Decrease in the particle size leads to increase in surface area, therefore increased surface area to volume ratio of the nanoparticles

The reason behind this can be understood from a simple calculation given below:

Consider a spherical particle of size of diameter D . It is easy to see that for such a particle the surface to volume ratio = $(S/V) = (6/D)$. This ratio being inversely proportional to size D , as the size of the particle decreases, the surface to volume ratio increases significantly. Therefore surface effects become highly prominent in nanosystems.

The surface atoms distinctly contribute to free energy. The smaller is the nanoparticle, larger is the contribution made by surface energy of the system. Thus, we can observe changes in some specific properties such as decrease of melting temperature, solid – solid phase transition, etc. ^[5, 14] in the case of the nanoparticles in order to minimize the energy.

1.2.4 Magnetic Properties

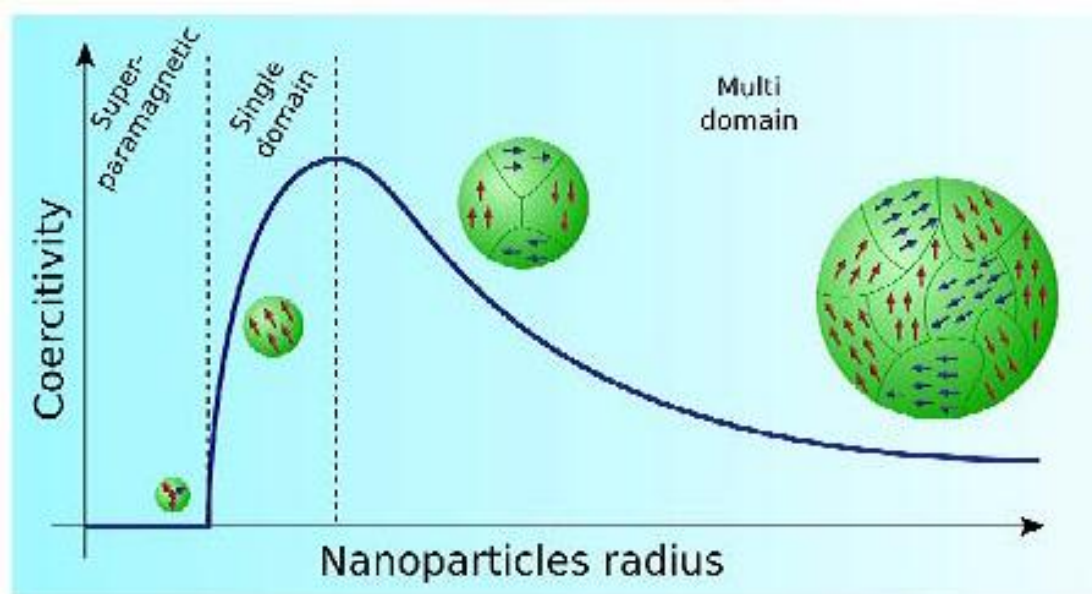


Figure 1.6: Dependence of coercivity on the nanoparticle size. Multi-domain, single domain and superparamagnetic regions are shown (printed with permission: ref. 15(b))

Materials show very interesting magnetic properties as well by synthesizing them on the nanoscale. The reduction in size could enhance the magnetic behaviour of a magnetic system or induce magnetism for some nonmagnetic materials. In a

ferromagnetic material, there exist magnetic domains. As the size of the particle is reduced below a critical value, it becomes single magnetic domain particle as shown in figure 1.6. By reducing the size further, a state is attained where the coercivity becomes zero. This is the state where the particle becomes ‘superparamagnetic’ [15]. At this stage the particle size is so small that the thermal effects dominate and the thermal energy $k_B T$ is enough to overcome the anisotropy barrier KV . This results in the rotation of the magnetization spontaneously giving an average zero magnetization when no external field is applied. It occurs below a specific temperature called as the blocking temperature (T_B). This can be understood from the equation $KV = 25 k_B T_B$ where K , V and k_B are the effective uniaxial anisotropy energy per unit volume, the volume of a single particle and Boltzmann constant, respectively.

From the equation, it can be seen that as the particle size decreases, the effective magnetic anisotropy energy (KV) also decreases. For a given particle, K , V and k_B would be constant and the thermal energy would be a function of the blocking temperature. Above the blocking temperature, the thermal energy is sufficient to flip the spins in the magnetic material; hence the material does not show any hysteresis loop. In the case of superparamagnetic materials, a plot of the magnetization (M) and the ratio of the magnetic field and the temperature (H/T) produces a universal curve for all temperatures above T_B .

The 1D nanomaterials have shape anisotropy, which may induce a magnetic easy axis along say the nanowire axis, resulting in high coercivity fields, which are inversely proportional to the diameter of nanowires. The magnetic nanoparticles can be used in various biomedical applications like drug delivery and hyperthermia.

1.3 Quasi 1D Materials

Nanomaterials can be classified into three types: 2D, 1D and 0D. In principle, such structures exhibit different density of electronic states predicted by simple ‘particle in a box’ model [5], as shown in figure 1.7, depending on their quantization dimensions. These ideal quantized structures are often called as quantum wells (2D), quantum wires (1D) and quantum dots (0D). The quantum wires have two quantum-confined directions and one unconfined direction available for free motion of

electrons. Such a system is possible when the diameter of the wire is comparable to the de Broglie wavelength of electrons, typically ~ 10 nm. Specifically, it would also involve relevant length scale, e.g. the Fermi wavelength, Bohr exciton radius, coherence length, or scattering length in comparison with the dimension of these nanostructures^[3, 16]. Practically, we work with the 1D nanostructures with diameter of about few tens or hundreds of nanometers; therefore we call such structures as “quasi” 1D nanostructures.

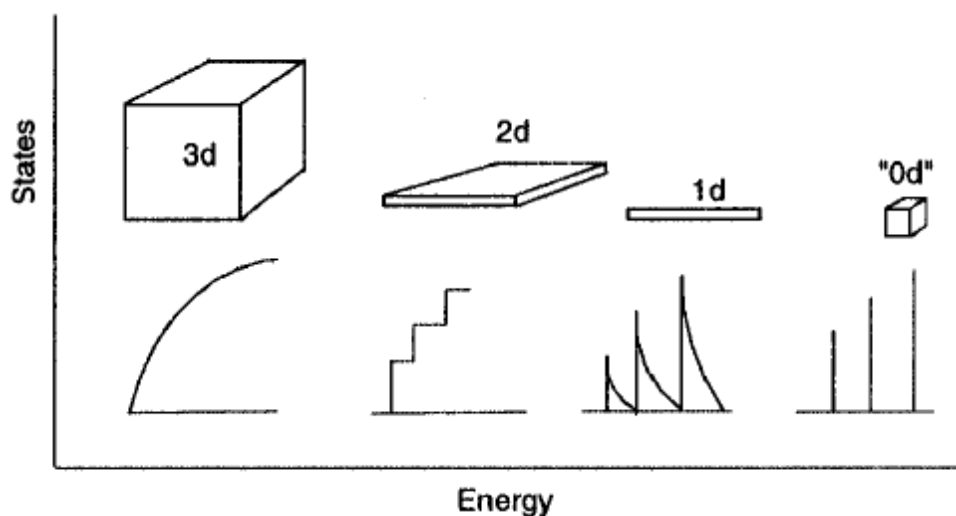


Figure 1.7: Change in the electronic band structure depending on the quantization dimensions (Printed with permission from ACS; ref. 5)

Quasi one dimensional (1D) materials are a special class in nanomaterials family. They are highly elongated, anisotropic structures with high aspect ratio (length to diameter ratio). Nanowires, nanotubes and nanorods are a few examples of them. Figure 1.8 shows some of our lab-synthesized quasi 1D metal oxide nanostructures, as examples. Since the discovery of carbon nanotubes by Ijima^[17], there has been a great interest in the field of quasi 1D structured materials. 1D nanostructures possess many interesting optical, electrical and magnetic properties as compared to their bulk 3-D crystalline counterparts. Such properties would directly lead to their applications for various nanoscale electronic and optoelectronic devices. The increased surface-to-volume ratio and increased aspect ratio make them useful in catalytic and sensing applications^[18].

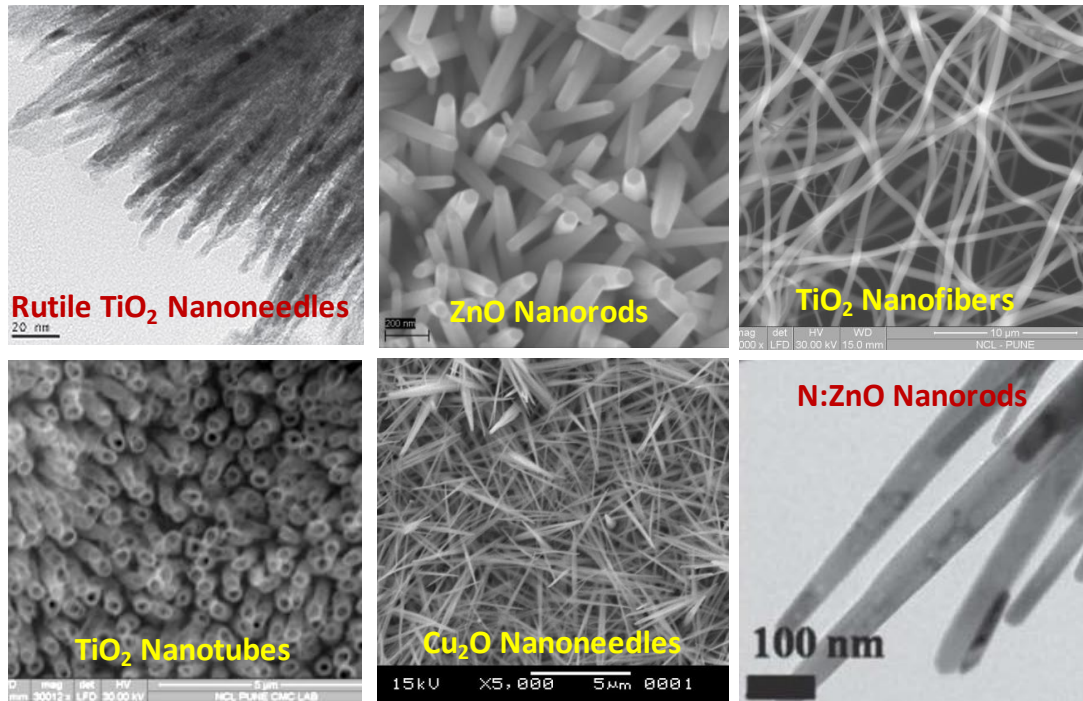


Figure 1.8: Lab synthesized quasi 1D Metal Oxide Nanostructures

1.3.1 Properties of quasi 1D nanomaterials

1D nanostructures show very interesting electronic, optical and chemical properties because of the high aspect ratio, quantum confinement effects and very high surface area ^[19]. This new class of shaped materials with controlled alignment, composition and crystallinity are of great interest to a variety of applications.

1.3.1.1 Mechanical and Thermal Properties:

One-dimensional nanostructures show a variety of interesting and useful mechanical properties. The mechanical properties of materials are governed by the grain boundaries. A single crystalline nanomaterial experiences drastic reduction of grain boundaries leading to less number of defects. In principle, single crystalline 1D nanostructured materials approach the theoretical limit of strength, stiffness and toughness of materials due to the reduction in the number of defects per unit length ^[20]. Their high stiffness and strength lend them to applications in tough composites as nanoscale actuators, force sensors and calorimeters.

Thermal conduction via phonons is expected to be significantly reduced in 1D nanostructure. When the dimensions of a 1D structure approach the mean free path

of phonons, the phonon confinement effects start playing a key role. The thermal conductivity is reduced due to this, relative to bulk values by scattering of phonons by surfaces and interfaces. Furthermore, roughening of nanowire surface also plays an important role in the reduction of thermal conductivity. Such a size-dependent thermal conductivity shows advantages for thermoelectric (TE) materials. Just by adjusting the diameter (<50 nm) of the thermoelectric material, the thermal conductivity can be greatly reduced and the thermoelectric figure of merit (ZT) can be increased to >1 ; which is useful for potential thermoelectric materials ^[21].

1.3.1.2 *Electronic Transport Properties*

The electronic transport properties of 1D nanostructures are mainly important for the design and fabrication of electronic devices at the nanoscale. The transport properties of the 1D material are mainly governed by its diameter (as it can give information about quantum size effect), crystal quality, surface states, and the crystallographic orientation (for materials with anisotropic material parameters such as the carrier mobility) ^[22].

The electronic transport properties for 1D nanostructures can be categorized as: ballistic transport and diffusive transport. The most remarkable phenomenon observed in case of some nanowires is the ballistic transport. It can take place when the electrons travel along the nanowire without any scattering. Ballistic transport can be observed when the mean free path of the electrons is much larger than the nanowire length, and the nanowire is defect-free. Generally, ballistic transport is observed for very short quantum wires. This phenomenon has been observed for the case of metallic single walled carbon nanotubes (SWNTs) over ~ 1 μm length. On the other hand, there is no observation of ballistic transport in the case of multiwalled carbon nanotubes (MWNT) and semiconducting SWNT, because of the presence of large barriers to conduction along their lengths ^[23].

For most of the practical nanowires, with length much larger than the carrier mean free path and diameter of a few tens of nanometers, the electrons (or holes) undergo numerous scattering events when they travel along the length. In this case, the electronic transport is the diffusive transport, and the conduction is dominated by carrier scattering within the nanowires, due to phonons (lattice vibrations), boundary

scattering, lattice and other structural defects, and impurity atoms. It is believed that, the quasi 1D nanostructure may still provide a direct channel for electric transport because of less grain boundaries or their complete absence; which is very useful for phenomena such as photovoltaic devices, e.g. dye sensitized solar cells, based on nanowires ^[24]. For efficient electronic devices, synthesis of single crystalline 1D nanostructures with minimum defects density is still an essential requirement, to minimize scattering due to structural defects.

1.3.1.3 Optical Properties

The most striking optical property in quasi 1D semiconductors is the lasing action. Nanowires with flat ends can act as optical resonance cavities, which lead to generation of coherent light at the nanoscale. When the aligned nanowires are pumped with a laser, the light emission is observed normal to the end surface plane. This spontaneous emission mainly originates from the radiative recombination of excitons to generate a photon. The emission peak is observed when the excitation power exceeds a threshold value ^[25]. Although the lasing action has been observed for ZnO and GaN nanowires, this concept of formation of optical resonance cavity can be expandable to many other single-crystalline, well-faceted nanowires.

In addition, the 1D nature often induces a highly polarized light emission along the longitudinal direction, as observed from isolated InP nanowires ^[26]. There exists anisotropy in the PL emission for the nanowires measured in parallel and perpendicular to the axis of nanowires. Such a large polarization response could be used to fabricate polarization-sensitive nanoscaled photodetector. Metal nanowires show two Surface Plasmon Resonance (SPR) modes, corresponding to transverse and longitudinal excitation. The longitudinal modes are tunable depending on the diameter of nanowire.

1.3.1.4 Photoconductivity

Optical switches are very important nanoscale devices for the memory applications. The high sensitivity opto-electronic switches can be constructed by controlling the photo-conductance of 1D nanostructures ^[27]. The light-induced high resistance state to low resistance state transition facilitates these nanostructures to

toggle from OFF to ON state. Electronic conductivity in semiconductor 1D nanostructures is substantially enhanced by exposing them to photons of energy greater than their band gaps. The photoconductivity in oxides can also be controlled by chemisorbed surface oxygen species.

1.3.2 Synthesis methods for quasi 1D nanostructures

For the synthesis of 1D nanostructures several strategies are followed such as: (i) use of templates (with 1D morphologies) to direct the formation of nanowires, (ii) super-saturation control to modify the growth habit of a seed, (iii) use of capping agents to kinetically control the growth rates of the various facets, (iv) the use of the anisotropic crystallographic structure of the solid to facilitate 1D nanowire growth, and (v) self-assembly of zero-dimensional (0D) nanostructures ^[19, 28]. Some of the synthesis methods are discussed in brief here.

1.3.2.1 Template-Assisted Synthesis

In this method, a host structure with pore morphology – the template – is filled with a chosen material, which adopts the pore morphology to form nanowires or nanotubes on the removal of the template material ^[29]. Generally, Anodized Aluminium Oxide (AAO) or polycarbonate membranes with cylindrical pore structures are used as templates. The diameter of nanowires can be controlled by controlling pore diameter, which can be varied from <10 nm to 200 nm. Sometimes, some already existing nanowires are also used as templates to generate nanowires or nanotubes of other materials which might be difficult to directly synthesize otherwise.

Filling of the pores is possible either via solution (simply by capillary filling), by electrochemical deposition or via the gas phase. The electrochemical deposition is most widely used method for this purpose, provided that the template is stable in the chosen electrolyte and under the applied electric field. For the vapour deposition, Physical Vapour Deposition (PVD) or Chemical Vapour Deposition (CVD) technique is used. By using this method we can get single crystalline nanowires of the desired material. After the deposition process, the selective removal of template is done by chemical etching or annealing treatment in order to get the resulting nanostructure.

1.3.2.2 Vapour-Liquid-Solid (VLS) Technique

Vapour – Liquid – Solid (VLS) is one of the most popular methods for nanowire synthesis, mainly used for single crystalline growth. In this process, the anisotropic growth is carried out in presence of a catalyst in molten state. The vapours of source material prefer to absorb on this catalyst in liquid state, which then becomes saturated with a gaseous precursor to form an alloy. When this alloy becomes supersaturated, nanowire of the source material starts growing by precipitation at the liquid-solid interface ^[30]. An elemental wire or a compound wire depending on the precursor can be synthesized. The diameter of the nanowire depends on the size of the catalyst nanoparticle. Nanowires grow as long as active catalyst is supplied and the growth temperature is maintained.

This is essentially the method proposed for whisker growth from the vapour. Generally, laser ablation, CVD or thermal evaporation is used to generate vapours of the desired material for nanowire growth. Growth temperature is a critical parameter which should be set between the eutectic point of the alloy and melting point of the nanowire material ^[31].

1.3.2.3 Electrochemical Deposition

In Electrochemical deposition or electrodeposition, solid material is deposited on an electrode in the presence of dissolved precursors by applying electric field. The electrochemical deposition method is a low-cost and scalable method but can be used only for the deposition of conducting and semiconducting materials. When the deposition is confined inside the porous membrane (template), nanorods or nanowires can be prepared. Electrodeposition has also been explored for the synthesis of nanowires of oxide semiconductors and conductive polymers without using templates ^[32]. Such growth of nanowires is a self-propagating process. When electric field is applied, depending on the polarity of the electrode, the material gets reduced/oxidized on the electrode leading to the nucleation of the species. The addition of capping agents or directing agents will direct further growth by adsorbing on specific crystallographic planes, leading to 1D morphology. In some cases, like in ZnO, selective adsorption of growing units on specific planes due to the polar surface leads to the formation of nanorods morphology. Electrochemical deposition

technique is greatly advantageous over the others because by simply adjusting the applied current, bath chemistry and temperature, the morphology and thickness of the film can be tuned.

1.3.2.4 Electrospinning

Electrospinning is a very simple technique to form nanofibers, though it is mainly used for polymer nanofibers synthesis^[33]. By combining it with conventional sol-gel processing, it also provides a versatile technique for producing ceramic nanofibers with either a solid, porous, or hollow structures^[34].

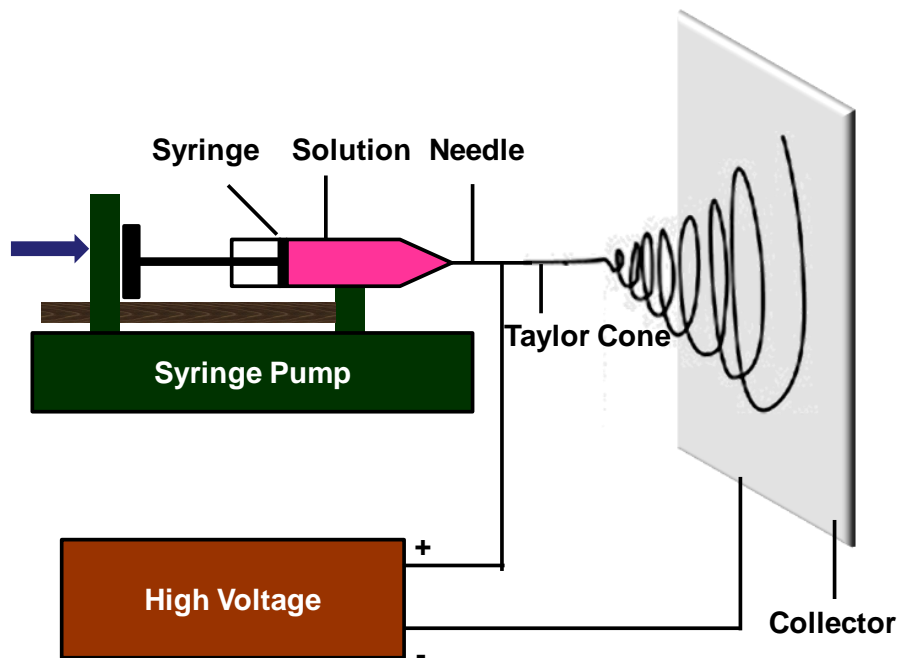


Figure 1.9: Schematic diagram of electrospinning setup

Figure 1.9 shows schematic diagram of electrospinning set up. There are basically three components to perform the process: a high voltage supply, a syringe (containing solution) with a needle of small diameter, and a metal collector. One electrode is placed at the needle attached with syringe containing spinning solution/melt and the other attached to the collector. In most cases, the collector is simply grounded. In the electrospinning process a high voltage (normally 1 to 30 kV) is applied at the needle containing polymer solution. This induces a charge on the surface of the polymer droplet. As a result, the polymer drop experiences two major electrostatic forces: repulsion between surface charges and external electric field.

Under these forces, the drop gets distorted into conical form, known as Taylor cone. Once the applied electric field increases the threshold value, the electrostatic forces overcome the surface tension of the polymer solution and thus a liquid jet ejects from the nozzle. This jet then elongates and the solvent evaporates to form fibers which are collected on the grounded metallic collector plate. The fiber diameter can be controlled by adjusting the applied electric field, flow rate and the viscosity of the polymer solution.

1.3.2.5 Solution based methods

The main advantages of solution based methods for the fabrication of quasi 1D structures are their high yield, low cost and ease of fabrication. Anisotropic growth of crystals induced by different surface energies lead to the formation of 1D nanostructures. However, not many materials have anisotropic crystal structures. Therefore, to grow 1D nanostructures with specific orientation, capping reagents are extensively used to break the growth symmetry. The capping reagents get adsorbed selectively on specific surfaces reducing their growth, which leads to the crystal growth along the other uncapped directions ^[3, 19, 31].

One of the commonly used solution-based fabrication techniques is the solvothermal method. A typical solvothermal process includes a mixture of precursor and a reagent for regulating or templating crystal growth like amines, and subsequent reactions under elevated temperatures and pressures. In hydrothermal method, an autoclave is used to speed up the growth and assembly.

1.3.3 Heterojunctions

Individual, homogeneous semiconducting nanowires have been previously used as field effect transistors, photodetectors, and bio/chemical sensors, while more sophisticated devices such as light-emitting diodes and complementary logic devices have been constructed by assembling both n- and p-type semiconducting nanowires into crossed junctions ^[35]. Interestingly, formation of heterostructures with components having different functionalities with favourable band alignment can not only lead to a functional integration of the properties of both the materials but also to novel interface effects and phenomena, and thus prove to be more useful for

constructing new-concept nanoscale functional devices ^[36]. The different ways of making heterojunctions of 1D nanostructures are as follows:

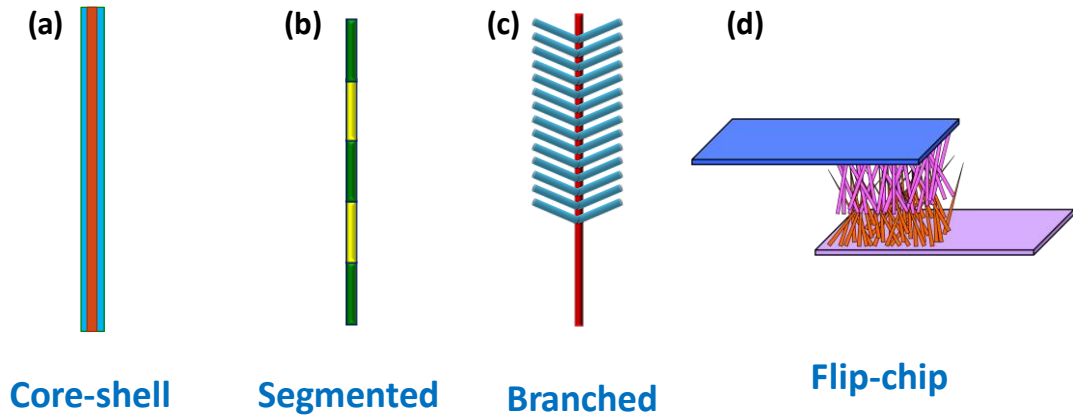


Figure 1.10: Types of heterojunctions using 1D nanostructures

1.3.3.1 Core – Shell Structure

A solid nanowire (core), fully covered with another material (shell), forms a core-shell structure or radial nanowire heterostructure ^[37], as shown in figure 1.10 (a). Several types of core/shell structure have been synthesized, such as semiconductor/oxide, metal/oxide, oxide/oxide, oxide/polymer, etc. In some of core-shell assemblies, the shell layer is deposited as a protecting layer for the core nanostructure. Atomic Layer Deposition (ALD) technique can be used for uniform deposition of shell layer on pre-grown core nanowire. ALD is a very good technique for layer-by-layer deposition of a desired material, giving rise to precise control on the thickness of the shell layer. The design and synthesis of functional core-shell semiconductor heterostructure are very important for constructing new functional devices such as p–n junctions, LED and photovoltaic cells, etc.

1.3.3.2 Segmented (Superlattice) Structure

The concept of thin film superlattice can be extended in nanostructured form as shown in figure 1.10 (b). This can greatly increase the versatility and power of the nanostructured building units in newer electronic and photonic applications, including thermoelectrics, nano-barcodes, injection lasers, and engineered one-dimensional waveguides ^[38]. There are a number of ways of making the segmented

structures, VLS method being the most effective amongst them. Generally, a catalyst common to two different materials could be used to grow a nanowire superlattice structure by modulating the reactants during growth.

1.3.3.3 Hierarchical branched nanostructure

The most popular and effective method of preparation of 1D heterojunctions is the hierarchical branched nanostructures (or 3D branched structures). Their synthesis is possible by simple chemical routes, which lead to increasing interest in these complex 3-D hierarchical branching nanowire structures (figure 1.10 (c)). In addition to other properties of 1D heterojunctions, they show multiple junctions formation. They also promise to improve the solar energy harvesting than that of simpler 1D nanowire arrays by intensely scattering light that is not absorbed, resulting in a longer effective path for light to travel through the absorber layer. This results in a good current density in opto-electronic devices. Just as trees in the natural world expose large surfaces for effective photosynthesis, these extensively branched structures have large area to harvest solar light and increased scattering that improves light absorption ^[39]. The high surface area can also increase the number of interactions between surface catalytic centres in PEC cells ^[40]. The incorporation of such hierarchical nanostructures into a solar conversion device is a dramatic departure from the conventional paradigm of planar junction solar cells and is quite a challenging research frontier.

1.3.3.4 Flip – Chip Arrangement

When two 1D nanostructures are grown separately on different substrates, we can make heterojunction of them by Flip-chip arrangement, as shown in figure 1.10 (d). The concept of flip-chip interconnection method in micro-patterning can be used here for heterojunction of two 1D structures. Although researchers have used this flip-chip arrangement in fabrication of devices like photodetectors and resistive switching ^[41], the method is not explored for other electronic devices effectively.

The major advantage of this arrangement is that the 1D nanostructures can be grown on any desired substrate by any suitable route. Sometimes, formation of heterojunction by other methods is not possible due to incompatibility of precursors

and/or formation temperature. In such cases, junction formation by flip-chip method is an easy task.

1.4 Metal Oxide Nanomaterials

The need for alternative non-silicon materials for electronic applications has led to extensive studies of metal oxides as they offer a broad and rich range of physical properties ^[42]. The important strength of the oxides is their ability to exhibit very wide range of functionalities due to their fascinating magnetic, dielectric, piezoelectric, semiconducting, superconducting, as well as various other physical, chemical, electrochemical, catalytic properties and often a combination of them ^[43]. Moreover, generally these materials have good chemical stability. The metal oxide research and development includes design and fabrication of thin films, their heterostructures and engineered nanomaterials that exhibit either enhanced or multiple functionalities than the existing technologies. Understanding and controlling the properties and behaviour of a wide range of oxide materials at the nanoscale is now a major theme in materials research.

Amongst the various metal oxides, there is one technologically very important group of materials, namely the transition metal oxides. Transition metal oxides are the compounds composed of transition metals and oxygen atoms. A special characteristic of these materials is the existence of more than one oxidation states of transition metal ions which can convert to one another ^[44]. Because of this, these materials have extremely varied electronic properties, ranging from insulating to metallic, and exhibit several interesting phenomena such as superconductivity and metal-insulator transitions. Due to such wide range of properties immense research is being done to manipulate such properties for a variety of applications.

In our studies, we have synthesized some 1D transition metal oxide nanostructures, of p-type Cu_2O , n-type ZnO , TiO_2 and their heterojunctions. They are further studied for applications such as photodetectors, field electron emitters, photocatalysis, and water splitting.

1.4.1 Cuprous Oxide (Cu_2O)

Copper has two oxide phases, cupric oxide (CuO) and cuprous oxide (Cu_2O). Interestingly, Cu_2O is one of the first known semiconducting materials and some early electronic devices like rectifying diode and solar cell were constructed using Cu_2O in 1920s^[45], long before silicon became the standard norm. In the history of semiconductor physics, Cu_2O is one of the most studied materials, and many experimental observations and semiconductor applications have been demonstrated first in this material. The most practical thing about Cu_2O is its ease and cost-effectiveness of preparation. The single crystal can be prepared by simple oxidation of copper at high temperature while thin films can be grown simply by electro-deposition or sputtering. Additionally Cu_2O is composed of two very abundant and non-toxic elements.

Cu_2O is one of the very few p-type oxides with a band gap of ~ 2.17 eV. The p-type conductivity is mostly caused by copper vacancies^[46], where the acceptor-type energy level is situated at ~ 0.3 eV above the valence band edge in single crystal Cu_2O . Cuprous oxide (Cu_2O) crystallizes in a cuprite structure i.e. cubic structure with the Cu atoms arranged in a fcc sublattice and the O atoms in a bcc sublattice, where one sublattice is shifted by a quarter of the body diagonal. The crystal structure of Cu_2O consists of two interpenetrated and independent cristobalite like lattices as seen in Figure 1.11. Cu_2O has a lattice constant $a=4.27$ Å.

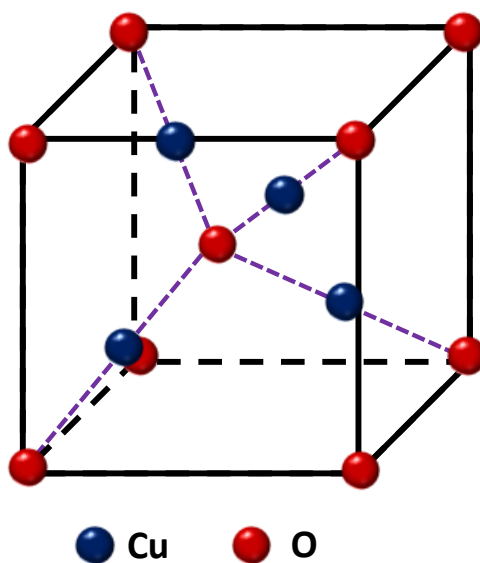


Figure 1.11: Crystal structure of cuprous oxide

Cu₂O shows many interesting characteristics for electronic and opto-electronic applications such as a good absorption coefficient ^[47] for the light having energy above the band-gap (which is of the order of 10⁴ cm⁻¹ at ~500 nm), a good hole mobility at room temperature, (which is reported ~100 cm² V⁻¹ S⁻¹ for a single crystal Cu₂O), minority carrier diffusion length of ~1-2 μm etc ^[48]. The resistivity of Cu₂O is strongly dependent on the post annealing processes, and can vary from a few tens of Ω-cm to 10¹⁴ Ω-cm ^[49].

Cu₂O is considered as good material for many electronic devices. It has attracted much attention with doping of magnetic impurities like Mn or Co as a dilute magnetic semiconductor (DMS) ^[50]. This class of materials is very important because of the potential use of both the charge and spin properties of electrons for spintronic devices. Observations of room temperature ferromagnetism in the Al and Co co-doped Cu₂O film have been reported with Curie temperatures far greater than room temperature ^[51]. Another recent technological application using Cu₂O films is the fabrication of low-cost non-volatile memories, based on the effect of the resistive switching ^[52]. Also, Cu₂O has always been considered a material suitable for the realization of low cost solar cells, as its theoretical efficiency is ~15% ^[53]. It has been widely studied for optoelectronic applications like photo-catalysis ^[54], Li-ion batteries ^[55], photo-electrochemical cells ^[56], photo-sensors ^[57], etc.

1.4.2 Zinc Oxide (ZnO)

Nanostructured inorganic crystals with tunable morphology are desirable in many potential applications in the fields of energy conversion, electronics, catalysis, optics, chemical sensing, and medicine. Controlled growth of hierarchical crystal architectures has received particular attention recently to support application demands because more complex structures enable greater control over material and device properties ^[58]. Since Zinc Oxide (ZnO) is a wide band gap (3.37 eV) semiconductor material it has attracted a great deal of attention for its potential uses in UV light emitters, field emission, piezoelectric transducers, gas sensors, optical waveguides, transparent conductive films and dye-sensitized solar cells, etc. In terms of structural properties, ZnO is a polar crystal with a number of alternating planes composed of tetrahedrally coordinated O²⁻ and Zn²⁺ ions, stacked alternately along the c-axis. Thus, a ZnO crystal consists of a positively charged plane (001)

terminated with zinc and a negatively charged plane terminated with oxygen. ZnO has been prepared by a number of methods such as the reaction of zinc salts with base, chemical bath deposition, thermal decomposition, hydrothermal synthesis, sol-gel methods, template methods including the use of alumina membranes, microwave synthesis method and vapour phase transport, giving rise to particles of various shapes and sizes. So far, numerous forms of nanostructured ZnO with different morphologies such as nanowires, nanosheets, nanotubes, and nanoflowers have been fabricated ^[58(a)].

1.5 Applications of Metal Oxide Nanoparticles

Energy, Environment and Health are perhaps the most critical and interrelated fields of human concern at the present time. The development of advanced functional materials with novel set of properties is considered the key to address and resolve them. Metal oxide nanoparticles, because of their diverse set of interesting properties, have been explored for tremendous range of applications (figure 1.12) including energy conversion and storage, photocatalysis and for efficient electronic and magnetic devices. In the current research work, we have focused on a few electronic and opto-electronic applications of 1D metal oxide nanostructures, which are discussed in the following sections:

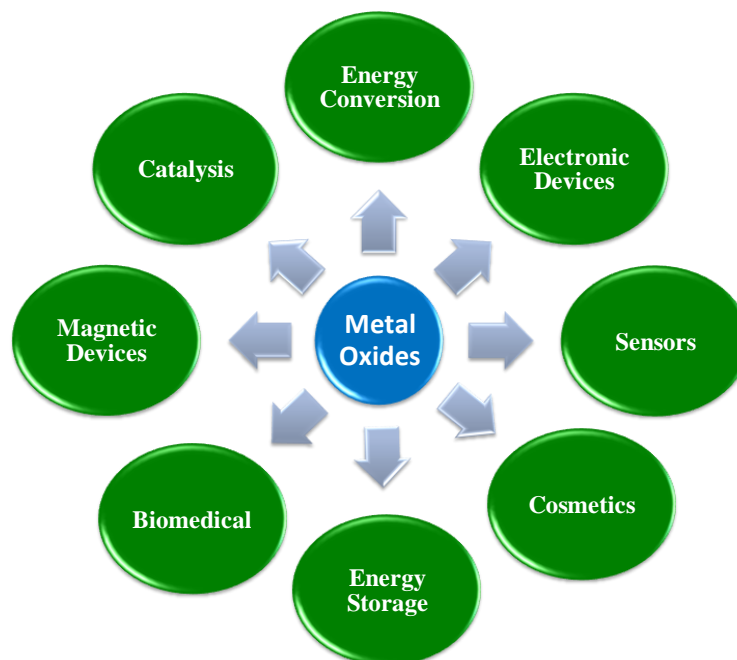


Figure 1.12: Tremendous range of applications of metal oxide nanoparticles

1.5.1 Photodetector

Photodetectors are used in variety of applications ranging from photo-switches to Charged Couple Devices (CCD) for imaging of astronomical objects. They are basically semiconductor devices that can detect an optical signal and convert it into an electrical signal. The operation of a general photodetector basically includes three processes: (1) carrier generation by incident light, (2) carrier transport and/or multiplication, and (3) extraction of carriers as terminal current to provide the output signal ^[59]. Three types of photodetectors are generally used: photoconductors, photodiodes and phototransistors. Out of these we will focus on the details about working mechanism and figures of merits for photodiodes, since they form an important portion of this thesis.

➤ Basic operation mechanism of photodiodes

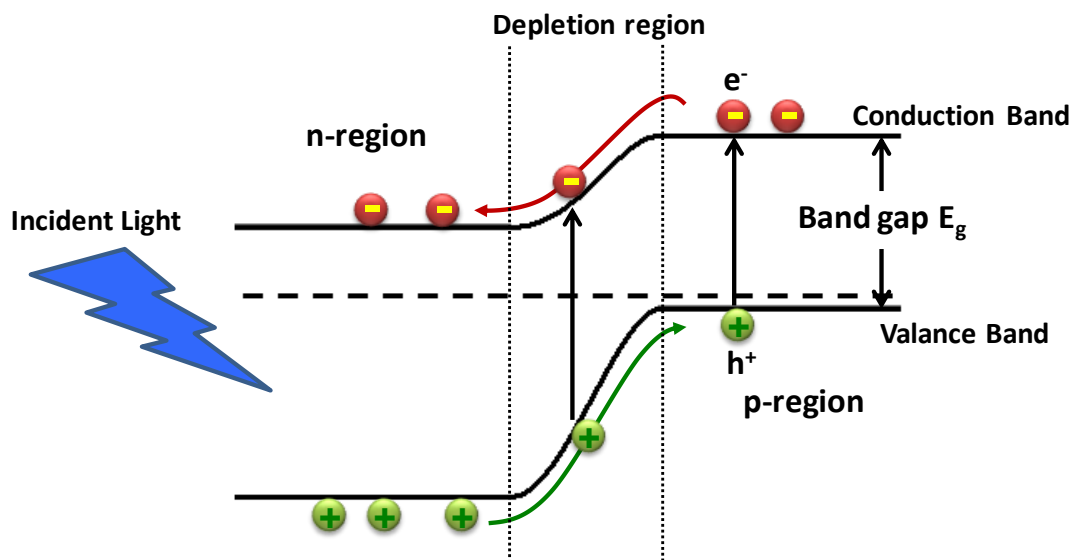


Figure 1.13: Operation mechanism of p-n junction photodiode

When two materials (p and n type semiconductors or metal/semiconductor) come into contact with each other, charge transfer takes place because of Fermi level mismatch so as to equilibrate it. This leads to the formation of a depletion layer at their interface. When the light of the energy greater than or equal to the band gap of one of the semiconductors strikes a photodiode, there is formation of electron-hole pair, in the semiconductor region or depletion region as shown in figure 1.13. In the depleted region, because of the built-in electric field, separation of the photo-

generated minority charge carriers takes place i.e. electrons from p-region are diffused to the n-region and holes from n-region are diffused towards p-region ^[60]. This results in the flow of current through external circuit at a certain applied bias. This current is a combination of various mechanisms like diffusion current in the bulk p and n regions, generation-recombination current in the depletion region, surface current from surface states, tunnelling current, etc.

➤ **Figures of merit**

As the photodetectors have practical applications in various fields like compact-disc players, optical-fiber communications, surveillance of rockets or intercontinental ballistic missiles, remote sensing, etc., they have to satisfy stringent requirements such as high sensitivity at the operating wavelength, good current response and minimum noise. There are a few parameters or figures of merit, which define a good photodetector ^[61]. These are as follows:

1. Quantum efficiency (η): Quantum efficiency is defined as the fraction of photons of a given wavelength that contributes to the current. It is governed by the absorption of light in the material and its conversion to electrical signal after avoiding losses of charge carriers due to recombination. Thus more the absorption coefficient and less the recombination, more is the quantum efficiency at a particular wavelength. For an ideal photodetector, the quantum efficiency should be 1 (or 100% if defined in terms of percentage).
2. Responsivity (R_λ): It is the ratio of the photocurrent to the incident optical power. In other words, it is the measure of the effectiveness to convert specific light power to the electric current.

It is determined as,

$$R_\lambda = \frac{\lambda \eta}{h c} qg$$

Where, η is the quantum efficiency of the photodetector at given wavelength (λ), q is the electron charge, h is the Planck's constant, c is velocity of light and g is the photoconductive gain.

3. Signal-to-noise ratio: As good photocurrent is important, minimum noise is also important, as it will determine the minimum detectable signal. Increased dark current due to the external applied bias and thermal generation of charge carriers

mainly contribute to noise. It is related to the detectivity (D) of the photodetector as,

$$D = R_\lambda \left(\frac{A_0 \Delta f}{I_n} \right)^{1/2}$$

Where, Δf is the frequency bandwidth, A_0 is the optical area and I_n is the noise current of the photodetector.

4. Response time: The response time of a photodetector is measured in two parts: rise time and reset time. The rise time is defined as the time taken by the photodetector to reach 90% of maximum photocurrent and the reset (recovery) time taken to reach $1/e$ times (37%) of the maximum photoresponse current. For a good photodetector, both the rise and recovery times should be as low as possible, typically in nanoseconds to a few microseconds.

1.5.2 Field Emission

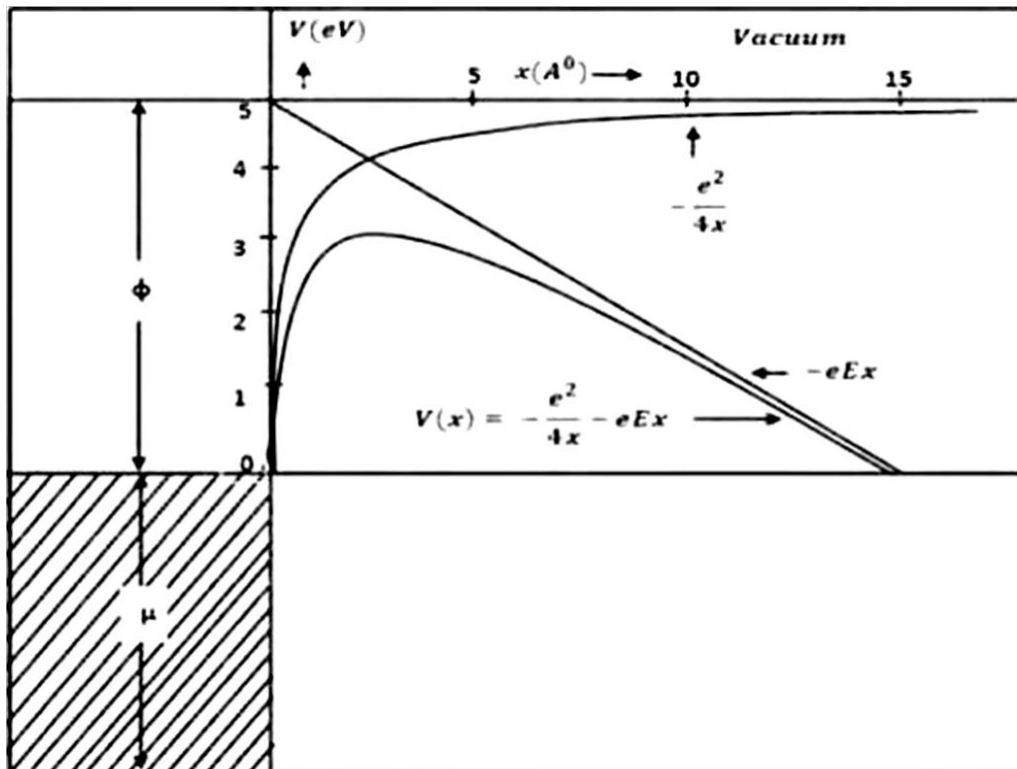


Figure 1.14: Schematic diagram of potential energy (V) of an electron as a function of distance x from the electron emitter surface. [Taken from ref. 62]

Nanowires have gained significant attention in last few years for the technologically important application of flat panel displays, for which cold cathodes or field electron emitters can be used as an alternative to thermionic emitters. The conventional thermionic emitters are associated with high power dissipation due to high cathode temperature, which discards their long term use. The field emission sources or guns are also used in scanning electron microscopy and electron beam lithography because of their small optical size.

Field emission, also known as field electron emission or cold cathode emission, is the tunnelling (ejection) of electrons from a metal or semiconductor surface in presence of high electric fields, typically of the order of $10^7 - 10^8$ V/cm. In order to produce such high electric fields using reasonable potentials, the emitter is typically formed into a tip with a very small apex radius of curvature. The high electric field induces field emission by narrowing the potential barrier at the solid-vacuum interface sufficiently for electrons to have a high probability of tunneling from the solid into the vacuum ^[62]. An overview of this potential barrier (V) narrowing phenomenon is given by Figure 1.14, showing the dependence of potential energy (V) of an electron as a function of the distance x from the electron emitter surface. From figure 1.14 it is seen that, as the applied electric field (E) between the cathode and anode is increased (thereby increasing the electric field strength), the negative slope of the potential barrier will increase, becoming narrower. It is a unique quantum-mechanical effect of electrons tunnelling from a condensed matter into a vacuum. The quantitative description of field emission is known as Fowler-Nordheim (F-N) theory ^[63], relating the emission current density to the applied electric field. The Fowler-Nordheim (F-N) equation for metals is given by,

$$J = \left(\frac{A\beta^2 E^2}{\phi} \right) \exp \left(- \frac{B \phi^{3/2}}{\beta E} \right)$$

Where, constants $A=1.54 \times 10^{-6}$ A eV V⁻² and $B= 6.83 \times 10^3$ eV^{-3/2} V μm⁻¹ ^[64], J is the current density, E is the applied electric field, φ is the work function of emitting material and β is field enhancement factor. Field emission theory for semiconductors could be more complicated. Great amount of research have been

conducted since the introduction of F-N theory to characterize the field emission characteristics of various geometries and dimensions of field emitters.

1D nanostructures are known to be ideal field emitters due to their small tip radii and large aspect ratio. Even for a low applied voltage, the local electric field at the tip is boosted up to a high value due to this particular geometry of the nanorods or nanowires^[65]. Aligned nanowires with a high packing density can again significantly enhance the field emission behaviour and make them more suitable for practical applications. Heterojunctions, especially hierarchical branched nanostructures^[66], are also of interest for their potential use in field electron emission. There are a few additional properties that the materials to be investigated must possess *viz.* vacuum compatibility, high mechanical strength, resistance to ion bombardment (due to residual gases in the vacuum chamber) and low work function. Zinc oxide is the most studied material in this regard because of its ease of formation of the branched nanostructure and other functional properties^[67].

1.5.3 Photocatalysis

Semiconductor based photocatalysis has attracted much attention due to its potential for pollutant degradation in the presence of sunlight^[68]. Photocatalysis is based on semiconducting materials e.g. TiO₂ nanoparticles as light activated catalyst for the degradation of organic pollutants. When nanoparticles are irradiated with photons of energy corresponding or exceeding the band gap energy of the semiconductor, an electron is promoted from valence band into conduction band leaving behind a hole. The excited electrons and holes then migrate to the surface of the nanoparticles. These electrons and holes react with adsorbed molecules (electron acceptors and donors) on the surface. The valence band holes act as powerful oxidants, whereas the conduction band electrons are good reductants. The mechanism of photocatalysis using a semiconducting nanoparticle is shown schematically in figure 1.15.

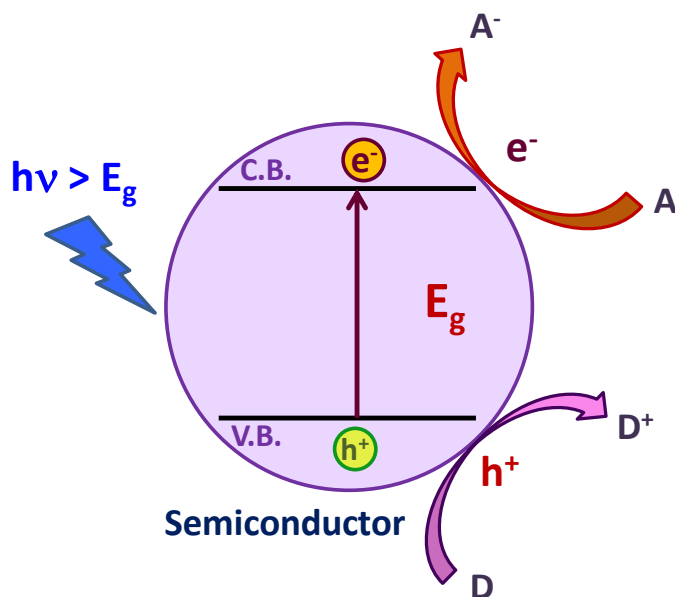
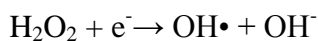
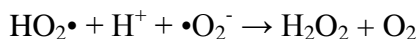
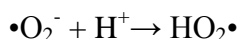
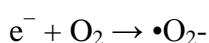
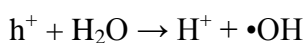


Figure 1.15: Mechanism of the photocatalysis using semiconducting nanoparticle

The hole is a strong oxidant which reacts with water molecule or OH^- adsorbed on the surface to form the hydroxyl radicals ($\text{OH}\cdot$). The electron reduces the oxygen adsorbed on the surface to form the superoxide anion ($\cdot\text{O}_2^-$). This can subsequently react with water to form the hydroxyl radical again ^[69]. The processes are summarized below:



Hydroxyl radicals are themselves very powerful oxidants, and can easily oxidize any organic species, ultimately to carbon dioxide and water.

Large number of electrons and holes, before coming to the surface, recombine dissipating the energy in the form of heat or emitted light. To avoid this recombination, some strategies such as loading of co-catalyst like Pd, RuO_2 on the semiconductor surface, making a composite with noble metal nanoparticles like Au

or Ag ^[70], and making heterojunctions with other semiconductors are followed. Heterojunction formation facilitates separation of charges which can improve the photocatalytic activity ^[71]. Also, it is advantageous to use nanoparticles with hierarchical morphologies because they have very high surface area, which is beneficial for photocatalytic activity ^[72].

1.5.4 Photo-electrochemical (PEC) Water Splitting

Hydrogen, being considered as a clean and efficient energy source, is proposed to be used instead of fossil fuels in the near future. Hydrogen is a potential fuel for non-polluting vehicles, aircrafts and domestic heating. The recent development of vehicles powered by fuel cells which use hydrogen as a fuel will definitely reduce the emission of greenhouse gases. So far, hydrogen has been produced from methane using steam reforming, which leads to emission of CO₂. For a viable and sustainable hydrogen economy, efficient and economical water splitting is the key factor ^[73]. Water splitting is a common term for chemical reaction in which water is split into oxygen and hydrogen. By a simple electrolysis, water can be split by applying a constant voltage in an electrolysis cell, which consists of two electrodes, cathode and anode, where reduction and oxidation reactions simultaneously take place forming H₂ (at cathode) and O₂ (at anode). However, water electrolysis using the electricity generated by burning of fossil fuels is also not environment friendly. Therefore generation of hydrogen by directly using solar energy is a viable option. There are two ways for hydrogen generation by solar energy: one is photocatalytic water splitting, which is also known as direct water splitting and another is photo-electrochemical water splitting. Photo-electrochemical cell carries out electrolysis of water in presence of light. This cell is comprised of a semiconductor (used as one of the electrodes) that absorbs solar energy and generates charge carriers (electrons and holes) to split water molecules. This process of photo-electrolysis integrates solar energy collection and water electrolysis, therefore it is considered as the most efficient renewable method for hydrogen production ^[74].

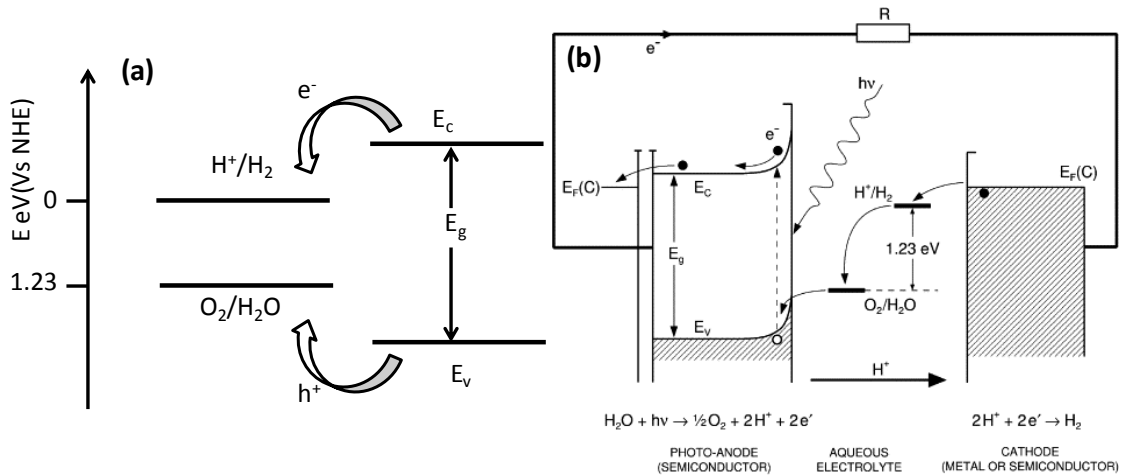
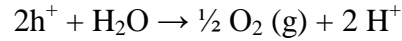


Figure 1.16: (a) Requirement of band alignment of the material with respect to water oxidation and reduction levels for overall water splitting (b) Electrical circuit showing the charge transfer in the within the PEC cell formed with semiconductor photoanode and metallic cathode [Printed with permission from Elsevier; ref. 74 (d)]

The spontaneous water splitting requires that the conduction band of the semiconductor should be above (i.e. more negative) the reduction potential of water, which is favourable for electron transfer for reduction of water to hydrogen and valance band is below (i.e. more positive) the oxidation potential, which is favourable for oxidation of water to oxygen, as shown in figure 1.16 (a). However in most of the n-type semiconductors the conduction band lies below the reduction potential of water. Thus a barrier is created at semiconductor-electrolyte interface which retards spontaneous water splitting. For these systems, external electrical bias is required for water splitting.

Let us consider a photo-electrochemical cell consisting of n-type semiconductor electrode (photoanode) and a metal counter electrode (commonly platinum is used so as to prevent corrosion and dissolution products). When the photoanode is illuminated with photons having energy ($h\nu$) greater than or equal to the band gap of semiconductor, then formation of electrons and holes takes place in the conduction and valance band of the semiconductor, respectively. At the interface between the photoanode and electrolyte, the photogenerated holes are transferred and react with the water leading to the formation of oxygen and hydrogen ions.



Gaseous oxygen is evolved at the photoanode and the hydrogen ion travels through the electrolyte to the cathode. At the same time, the photogenerated electrons are transferred to the cathode through external circuit; which reacts at the electrode-electrolyte interface with the hydrogen ion to evolve gaseous hydrogen. This process is shown in figure 1.16 (b) ^[75].

Under standard conditions, water can be electrolyzed at a potential of 1.23 V, which is derived from the relationship between water splitting threshold energy (E_t) and standard Gibbs free energy per mole of the reaction (ΔG^0):

$$E_t = \frac{\Delta G^0 (H_2O)}{2 N_A}$$

Where, ΔG^0 is equal to 237.141 kJ/mol and N_A is Avogadro's number which is equal to 6.023×10^{23} /mol, which results to the value of threshold energy as 1.23 eV. Therefore, water splitting can take place when the electromotive force of the cell (EMF) is equal to or larger than 1.23 V. In most cases, the generated EMF is less than 1.23 V. For example, TiO_2 , the most studied material as photoanode, generates voltage of ~0.7-0.9 V under solar light illumination in a photo-electrochemical cell. Hence water splitting can be performed only in the presence of external electric bias.

The materials used for water splitting should satisfy a few functional semiconducting and electrochemical properties for a good efficiency of PEC cell; which are as follows:

➤ **Band gap**

Band gap is a critical parameter for choosing the material for PEC; since only those photons absorbed by the material can be used for conversion (energy greater than or equal to its band gap). Theoretically the minimum band gap of ~1.23 eV is required to split the water molecule. In practice, for a good PEC material, this band gap requirement differs due to the losses caused by recombination and resistance of the PEC cell. Considering all the losses and a requirement of maximum absorption of light in the solar spectrum, the optimal energy for conversion is ~2 eV ^[75, 76].

➤ Semiconductor – Electrolyte interface and flat-band potential

When a semiconductor is immersed in the liquid electrolyte, a charge transfer occurs at the semiconductor/electrolyte interface so as to equilibrate Fermi energy of the semiconductor (E_f) and redox potential of the electrolyte. This charge transfer results in the formation of space-charge layer at the semiconductor surface forming a potential barrier. On the electrolyte side, a layer of opposite charges is induced known as ‘Helmholtz layer’. The height of this barrier is known as ‘Helmholtz barrier’. The efficiency of the PEC cell depends on this barrier as it is determined by the properties of the photo-electrode as well as the nature of the electrolyte ^[77].

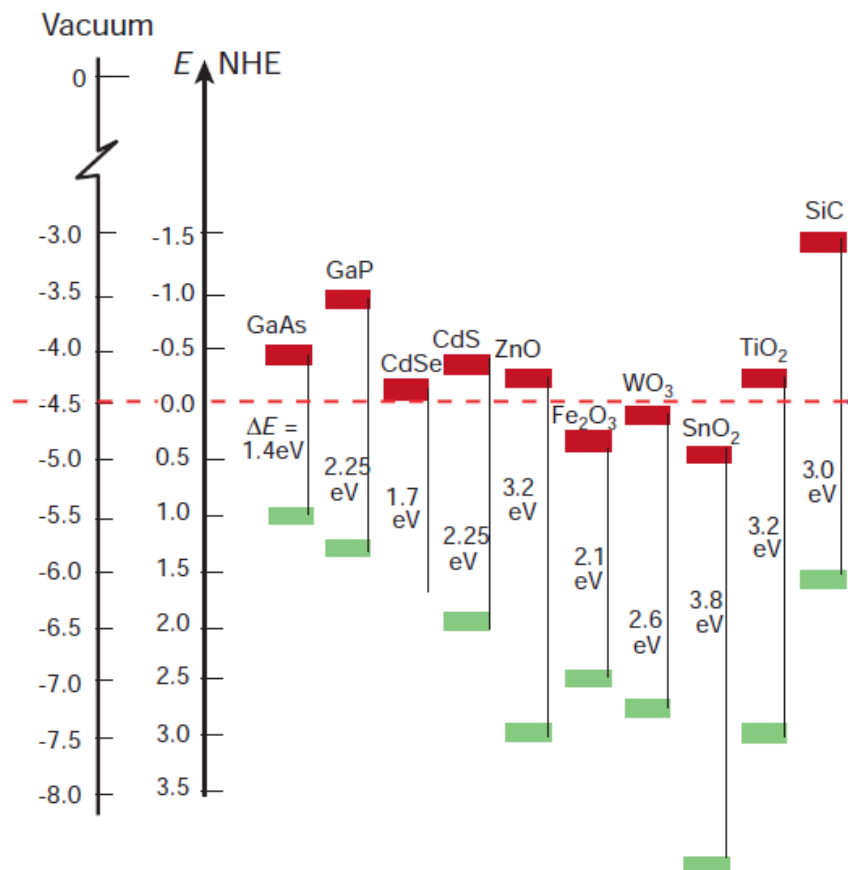


Figure 1.17: Band positions of semiconductors in contact with aqueous electrolyte of pH 1 [printed with permission from Nature, ref. 77 (a)]

The flat band potential, another useful quantity, is the potential which has to be applied at the semiconductor/electrolyte interface in order to make the bands flat. The flat band potential helps to determine the positions of conduction and valance

band edges of the photo-electrode with respect to the electrolyte. This can be measured experimentally by ‘Mott-Schottky plot’. Figure 1.17 shows the band positions of some semiconducting materials in contact with aqueous electrolyte of pH=1 vs. normal hydrogen electrode (NHE) and vacuum.

➤ **Electrical resistance**

The major sources of energy losses in the PEC cell are the electrical resistance of the photo-electrode, metallic counter electrode and electrical connections. In order to minimize the efficiency, the electrical resistances must be minimized. The electrical resistance of semiconducting photo-electrode is much higher than that of counter electrode and other electrical connections. Hence, the photo-electrode should be of high conductivity, which depends on the charge carrier density and their mobility.

➤ **Corrosion resistance**

The photo-electrode must be resistant to the corrosion reactions in the PEC cell that basically occur due to electrochemical reactions and photo-corrosion. The corrosion results in the degradation of the photo-electrode i.e. change in its chemical composition and properties, thereby its long term use becomes impossible. Many materials, which have other suitable properties for efficient photo-electrode, are not corrosion resistant. In electrochemical process, corrosion is observed due to excess or unwanted charge transfer at the electrode-electrolyte interface leading to anodic or cathodic decomposition. Therefore attempts have been made to protect such semiconductors from corrosion by deposition of suitable thin protective layers.

1.6 Outline of the thesis

Based on the background discussed above, the present thesis work was planned to explore the synthesis of quasi 1D metal oxide nanostructures and their heterojunction assemblies by employing novel routes for electronic and opto-electronic applications such as photodetection, Field Electron Emission, photocatalysis and photo-electrochemical hydrogen generation.

The outline of the thesis is as follows:

The important properties of nanomaterials, especially of quasi 1D nanomaterials and some of their applications have been discussed in **Chapter 1**.

In **Chapter 2**, a brief overview of the synthesis and thin film deposition methods for metal oxides are presented. Furthermore, a general outline of the instruments and methods used for the characterization of these nanomaterials for their potential applications are also presented.

Chapter 3 discusses the synthesis of cuprous oxide nanoneedles directly on copper substrate. The details of the further study for photodetector application by making p-Cu₂O nanoneedles/n-ZnO nanorods flip-chip heterojunction device has also been discussed. We have also observed that the nanowire heterojunction photo-response is far stronger as compared to a thin film heterojunction made of the same materials.

Chapter 4 discusses the fabrication of an interesting Cu₂O/ZnO hetero-nanobrush assembly. The hetero-nanobrushes show excellent field electron emission performance and photocatalytic activity. The detailed mechanism is studied and discussed in this chapter.

In **Chapter 5**, we have presented and discussed the results of photo-electrochemical water splitting using cuprous oxide nanoneedles on copper as photocathode. The effect of TiO₂ capping of Cu₂O nanoneedles on the photo-electrochemical activity is also discussed in this chapter.

Chapter 6 summarizes the work described in this thesis by presenting the salient features of the work and also mentions the possible avenues for future work.

1.7 References

1. Rolf E. Hummel, "*Understanding Materials Science: History, Properties, Applications*", Springer, 2nd ed. **2005**.
2. Chris Binns, "*Introduction to Nanoscience and Nanotechnology*", Wiley, **2010**.

3. (a) Bharat Bhushan, “*Springer Handbook of Nanotechnology*”, Springer, 3rd ed. **2010** (b) “*Biological and technological scales compared*” by Guillaume Paumier, Philip Ronan, NIH, Artur Jan Fijałkowski, Jerome Walker, Michael David Jones, Tyler Heal, Mariana Ruiz, Science Primer (National Center for Biotechnology Information), Liquid_2003, Arne Nordmann and The Tango! Desktop Project, under Creative Commons BY-SA 2.5, from Wikimedia Commons:http://commons.wikimedia.org/wiki/File:Biological_and_technological_scales_compared-en.svg
4. C. N. R. Rao, Achim Muller, Anthony K. Cheetham, “*The Chemistry of Nanomaterials*”, John Wiley & Sons, **2006**.
5. A. P. Alivisatos, *J. Phys. Chem.* **1996**, 100, 13226-13239.
6. Emil Roduner, *Chem. Soc. Rev.*, **2006**, 35, 583–592.
7. A. P. Alivisatos, *Science*, **1996**, 271, 933 – 937.
8. Pavel Zrazhevskiy, Xiaohu Gao *Nano Today*, **2009**, 4, 414 – 428.
9. (a) Adam M. Schwartzberg and Jin Z. Zhang, *J. Phys. Chem. C*, **2008**, 112, 10323 – 10337 (b) Jin Z. Zhang, Cecilia Noguez, *Plasmonics*, **2008**, 3, 127–150 (c) Susie Eustis and Mostafa A. El-Sayed, *Chem. Soc. Rev.*, **2006**, 35, 209–217 (d) Xiaohua Huang, Svetlana Neretina, and Mostafa A. El-Sayed, *Adv. Mater.*, **2009**, 21, 4880–4910.
10. (a) Colleen L. Nehl, Jason H. Hafner, *J. Mater. Chem.*, **2008**, 18, 2415–2419 (b) K. Lance Kelly, Eduardo Coronado, Lin Lin Zhao, George C. Schatz, *J. Phys. Chem. B*, **2003**, 107, 668-677.
11. (a) Ivan H. El-Sayed, Xiaohua Huang, and Mostafa A. El-Sayed, *Nano Lett.*, **2005**, 5, 829-834 (b) Xiaohua Huang, Prashant K Jain, Ivan H. El-Sayed, Mostafa A. El-Sayed, *Nanomedicine*, **2007**, 2, 681 – 693.
12. (a) Vivek Dhas, Subas Muduli, Wonjoo Lee, Sung-Hwan Han, Satishchandra Ogale, *Appl. Phys. Lett.* **2008**, 93, 243108 (b) Hyunbong Choi, Wei Ta Chen, Prashant V. Kamat, *ACS Nano*, **2012**, 6, 4418–4427 (c) Jifa Qi, Xiangnan Dang, Paula T. Hammond, Angela M. Belcher, *ACS Nano*, **2011**, 5, 7108–7116 (d) Suljo Linic, Phillip Christopher, David B. Ingram, *Nature Mater.*, **2011**, 10, 911 – 921.
13. G. Cao, “*Nanostructures and Nanomaterials: Synthesis, Properties and Applications*”, Imperial College Press, **2004**.

14. A. N. Goldstein, C. M. Echer, A. P. Alivisatos, *Science*, **1992**, 256, 1425 – 1427.
15. (a) Diandra L. Leslie-Pelecky, Reuben D. Rieke, *Chem. Mater.* **1996**, 8, 1770-1783 (b) Abolfazl Akbarzadeh, Mohammad Samiei and Soodabeh Davaran, *Nanoscale Research Letters* **2012**, 7, 144.
16. (a) Jiangtao Hu, Teri Wang Odom, Charles M. Lieber, *Acc. Chem. Res.*, **1999**, 32, 435-445 (b) Rupesh S. Devan , Ranjit A. Patil , Jin-Han Lin , Yuan-Ron Ma, *Adv. Funct. Mater.* **2012**, 22, 3326–3370 (c) Yury Gogotsi “*Nanotubes and Nanofibers*”, Taylor and Francis Group CRC Press, **2006**.
17. Sumio Iijima, *Nature*, **1991**, 354, 56 – 58.
18. (a) Tianyou Zhai, Liang Li, Ying Ma, Meiyong Liao, Xi Wang, Xiaosheng Fang, Jiannian Yao, Yoshio Bando and Dmitri Golberg, *Chem. Soc. Rev.*, **2011**, 40, 2986–3004 (b) Yun-Ze Long, Miao Yu, Bin Sun, Chang-Zhi Gu, Zhiyong Fan, *Chem. Soc. Rev.*, **2012**, 41, 4560–4580 (c) Nripan Mathews, Binni Varghese, Cheng Sun, Velmurugan Thavasi, Bjorn P. Andreasson, Chornghaur H. Sow, Seeram Ramakrishna, Subodh G. Mhaisalkar, *Nanoscale*, **2010**, 2, 1984–1998 (d) Hongtao Huang, Bo Liang, Zhe Liu, Xianfu Wang, Di Chen and Guozhen Shen, *J. Mater. Chem.*, **2012**, 22, 13428 (e) Allon I. Hochbaum, Peidong Yang, *Chem. Rev.*, **2010**, 110, 527–546 (f) Tianyou Zhai, Xiaosheng Fang, Meiyong Liao, Xijin Xu, Haibo Zeng, Bando Yoshio, Dmitri Golberg, *Sensors*, **2009**, 9, 6504-6529 (g) Guozhen Shen, Po-Chiang Chen, Kounghmin Ryu and Chongwu Zhou, *J. Mater. Chem.*, **2009**, 19, 828–839 (h) Zhong Lin Wang, *Adv. Mater.*, **2003**, 15, 432 – 436.
19. (a) Y. Xia, P. Yang, Y. Sun, Y. Wu, B. Mayers, B. Gates, Y. Yin, F. Kim, H. Yan, *Adv. Mater.*, **2003**, 15, 353 (b) Matt Law, Joshua Goldberger, Peidong Yang, *Annu. Rev. Mater. Res.*, **2004**, 34, 83–122.
20. Xihong Peng, “*Nanowires - Recent Advances*”, InTech, **2012**.
21. Allon I. Hochbaum, Renkun Chen, Raul Diaz Delgado, Wenjie Liang, Erik C. Garnett, Mark Najarian, Arun Majumdar, Peidong Yang, *Nature*, **2008**, 451, 163 – 168.
22. L. C. Lew Yan Voon, Yong Zhang, B. Lassen, M. Willatzen, Qihua Xiong, P. C. Eklund, *J. Nanosci. Nanotech.*, **2008**, 8, 1–26.

23. A. Bachtold, M. S. Fuhrer, S. Plyasunov, M. Forero, Erik H. Anderson, A. Zettl, Paul L. McEuen, *Phys. Rev. Lett.*, **2000**, 84, 6082 – 6085.
24. (a) Gyu-Chul Yi, Book - “*Semiconductor Nanostructures for Optoelectronic Devices: Processing, Characterization and Applications*”, Chapter 11 - Semiconductor Nanowires for Solar Cells, Springer Publisher Berlin Heidelberg, **2012** (b) Thomas J. Kempa, Robert W. Day, Sun-Kyung Kim, Hong-Gyu Park, Charles M. Lieber, *Energy Environ. Sci.*, **2013**, 6, 719 – 733 (c) Miao Yu, Yun-Ze Long, Bin Sun, Zhiyong Fan, *Nanoscale*, **2012**, 4, 2783 – 2796.
25. (a) ruoxue Yan, daniel Gargas, peidong Yang, *Nature Photonics*, **2009**, 3, 569 – 576 (b) P. Yang, H. Yan, S. Mao, R. Russo, J. Johnson, R. Saykally, N. Morris, J. Pham, R. He, H.-J. Choi, *Adv. Funct. Mater.*, **2002**, 12, 323–331.
26. Jianfang Wang, Mark S. Gudixsen, Xiangfeng Duan, Yi Cui, Charles M. Lieber, *Science*, **2001**, 293, 1455-1457.
27. Hannes Kind, Haoquan Yan, Benjamin Messer, Matthew Law, Peidong Yang, *Adv. Mater.*, **2002**, 14, 158 – 160.
28. (a) C.N.R. Rao, F.L. Deepak, Gautam Gundiah, A. Govindaraj, *Progress in Solid State Chemistry* **2003**, 31, 5–147 (b) E. Comini, C. Baratto, G. Faglia, M. Ferroni, A. Vomiero, G. Sberveglieri, *Progress in Materials Science*, **2009**, 54, 1–67.
29. Tianyou Zhai, Jiannian Yao, “*One-Dimensional Nanostructures: Principles and Applications*”, John Wiley & Sons, **2012**.
30. R. S. Wagner, W. C. Ellis, *Appl. Phys. Lett.*, **1964**, 4, 89 – 90.
31. N. Wang, Y. Cai, R.Q. Zhang, *Materials Science and Engineering R*, **2008**, 60, 1–51.
32. Guangwei She, Lixuan Mu, Wensheng Shi, *Recent Patents on Nanotechnology*, **2009**, 3, 182-191.
33. (a) Dan Li, Younan Xia, *Adv. Mater.*, **2004**, 16, 1151 – 1170 (b) Andreas Greiner, Joachim H. Wendorff, *Angew. Chem. Int. Ed.* **2007**, 46, 5670 – 5703 (c) Zheng-Ming Huang, Y.-Z. Zhang, M. Kotaki, S. Ramakrishna, *Composites Science and Technology* **2003**, 63, 2223–2253.
34. (a) Xiaofeng Lu, Ce Wang, Yen Wei, *Small*, **2009**, 5, 2349–2370 (b) R. Sahay, P. Suresh Kumar, R. Sridhar, J. Sundaramurthy, J. Venugopal, S. G.

- Mhaisalkar, S. Ramakrishna, *J. Mater. Chem.*, **2012**, 22, 12953 (c) Dan Li, Jesse T. McCann, Younan Xia, Manuel Marquez, *J. Am. Ceram. Soc.*, **2006**, 89, 1861–1869.
35. Yu Huang, Xiangfeng Duan, Yi Cui, Lincoln J. Lauhon, Kyoung-Ha Kim, Charles M. Lieber, *Science*, **2001**, 294, 1313 – 1317.
36. (a) Hai-Feng Zhang, Chong-Min Wang, and Lai-Sheng Wang, *Nano Lett.*, **2002**, 2, 941-944 (b) Yat Li, Jie Xiang, Fang Qian, Silvija Gradecak, Yue Wu, Hao Yan, Douglas A. Blom, Charles M. Lieber, *Nano Lett.*, **2006** 6, 1468-1473 (c) Fang Zhang, Yong Ding, Yan Zhang, Xiaoling Zhang, Zhong Lin Wang, *ACS Nano*, **2012**, 6, 9229–9236 (d) Ritesh Agarwal, *Small*, **2008**, 4, 1872–1893.
37. (a) Gyu-Chul Yi, Book - “*Semiconductor Nanostructures for Optoelectronic Devices: Processing, Characterization and Applications*”, Chapter 5 - Semiconductor Nanowire Heterostructures: Controlled Growth and Optoelectronic Applications, Springer Publisher Berlin Heidelberg, **2012** (b) L. J. Lauhon, Mark S. Gudiksen, Charles M. Lieber, *Phil. Trans. R. Soc. Lond. A*, **2004**, 362, 1247–1260 (c) Lincoln J. Lauhon, Mark S. Gudiksen, Deli Wang, Charles M. Lieber, *Nature*, **2002**, 420, 57 – 61.
38. Mark S. Gudiksen, Lincoln J. Lauhon, Jianfang Wang, David C. Smith, Charles M. Lieber, *Nature*, **2002**, 415, 617 – 620 (b) Yiyang Wu, Rong Fan, Peidong Yang, *Nano Lett.*, **2002**, 2, 83 – 86.
39. (a) Mutong Niu, Feng Huang, Lifeng Cui, Ping Huang, Yunlong Yu, Yuansheng Wang, *ACS Nano*, **2010**, 4, 681–688 (b) Meng Shang, Wenzhong Wang, Ling Zhang, Songmei Sun, Lu Wang, Lin Zhou, *J. Phys. Chem. C* **2009**, 113, 14727–14731 (c) Yanghui Sun, Qing Zhao, Jingyun Gao, Yu Ye, Wei Wang, Rui Zhu, Jun Xu, Li Chen, Jian Yang, Lun Dai, Zhi-min Liao Dapeng Yu, *Nanoscale*, **2011**, 3, 4418 – 4426.
40. Jian Shi, Xudong Wang, *Energy Environ. Sci.*, **2012**, 5, 7918
41. (a) Lijie Li, Yan Zhang, Zhengjun Chew, *Nano-Micro Lett.*, **2013**, 5, 159-162 (b) Ren-Jen Lin, Yung-Yu Hsu, Yu-Chih Chen, Syh-Yuh Cheng, Ruoh-Huey Uang, *55th Electronic Components and Technology Conference Proceedings.*, **2005**, 66 – 70.
-

42. (a) C. Noguera, “*Physics and Chemistry at Oxide Surfaces*”, Cambridge University Press: Cambridge, UK, **1996** (b) H. H. Kung, “*Transition Metal Oxides: Surface Chemistry and Catalysis*”, Elsevier: Amsterdam, **1989** (c) V. E. Henrich, P. A. Cox, “*The Surface Chemistry of Metal Oxides*”, Cambridge University Press: Cambridge, UK, **1994** (d) A. F. Wells, “*Structural Inorganic Chemistry*”, 6th ed., Oxford University Press: New York, **1987**.
43. (a) H. H. Kung, “*Transition Metal Oxides: Surface Chemistry and Catalysis*”, 1st ed., Elsevier science publisher: New York, **1989** (b) P. Poizot, S. Laruelle, S. Grugéon, L. Dupont, J-M. Tarascon, *Nature*, **2000**, 407, 496 (c) T. Gershon, *Materials Science and Technology*, **2011**, 27, 1357.
44. R. W. G. Wyckoff, “*Crystal Structures*”, 2nd ed., Wiley: New York, **1964**.
45. E. H. Kennard, E. O. Dieterich, *Phys. Rev.*, **1917**, 9, 58–63.
46. (a) Hannes Raebiger, Stephan Lany, Alex Zunger, *Phys. Rev. B*, **2007**, 76, 045209 (b) A. F. Wright, J. S. Nelson, *J. Appl. Phys.*, **2002**, 92, 5849 – 5851 (c) Michael Nolan and Simon D. Elliott, *Phys. Chem. Chem. Phys.*, **2006**, 8, 5350–5358.
47. Philip W. Baumeister, *Phys. Rev.*, **1961**, 121, 359 – 362
48. C.A. Dimitriadis, L. Papadimitriou, N.A. Economou, *Journal of Materials Science Letters*, **1983**, 2, 691 -693.
49. A. E. Rakhshani, *Solid-State Electronics*, **1986**, 29, 7-17.
50. Hannes Raebiger, Stephan Lany, Alex Zunger, *Phys. Rev. Lett.*, **2007**, 99, 167203.
51. S. N. Kale, S. B. Ogale, S. R. Shinde, M. Sahasrabuddhe, V. N. Kulkarni, R. L. Greene, T. Venkatesan, *Appl. Phys. Lett.*, **2003**, 82, 2100 – 2102.
52. A. Chen, S. Haddad, Y. C. Wu, Z. Lan, T. N. Fang, S. Kaza, *Appl. Phys. Lett.*, **2007**, 91, 123517.
53. L. C. Olsen, F. W. Addis, W. Miller, *Solar Cells*, **1982**, 7, 247 – 279.
54. Haolan Xu, Wenzhong Wang, Wei Zhu, *J. Phys. Chem. B*, **2006**, 110, 13829-13834.
55. Dequan Liu, Zhibo Yang, Peng Wang, Fei Li, Desheng Wang, Deyan He, *Nanoscale*, **2013**, 5, 1917 – 1921.
56. Adriana Paracchino, Vincent Laporte, Kevin Sivula, Michael Grätzel and Elijah Thimsen, *Nature Materials*, **2011**, 10, 456 – 461.

57. Kajari Das, S. K. De, *Journal of Luminescence*, **2009**, 129, 1015–1022.
58. (a) T. L. Sounart, J. Liu, J. A. Voigt, J. Hsu, E. D. Spoerke, Z. Tian, Y. Jiang, *Adv. Funct. Mater.*, **2006**, 16, 335 (b) Z. R. Tian, J. Liu, J. A. Voigt, B. Mckenzie, X. Huifang, *Angew. Chem., Int. Ed.*, **2003**, 42, 413 (c) X. Wang, C. J. Summers, Z. L. Wang, *Nano Lett.*, **2004**, 4, 423 (d) H. Cao, J. Y. Xu, D. Z. Zhang, S. H. Chang, S. T. Ho, E. W. Seelig, X. Liu, R. P. H. Chang, *Phys. Rev. Lett.*, **2000**, 84, 5584 (e) D. M. Bagnall, Y. F. Chen, Z. Zhu, T. Yao, S. Koyama, M. Y. Shen, T. Goto, *Appl. Phys. Lett.*, **1997**, 70, 2230 (f) V. Dhas, S. Muduli, W. Lee, S-H Han, S. Ogale, *Appl. Phys. Lett.*, **2008**, 93, 243108.
59. S. M. Sze, “*Physics of Semiconductor Devices*”, Wiley Eastern Limited, New Delhi, 2nd Edition, **1981**.
60. M. Razeghi, A. Rogalski, *J. Appl. Phys.*, **1996**, 79, 7433 – 7473.
61. Cesare Soci, Arthur Zhang, Xin-Yu Bao, Hongkwon Kim, Yuhwa Lo, Deli Wang, *J. Nanosci. Nanotechnol.*, **2010**, 10, 1 – 20.
62. Abbass Hashim, Book - “*Nanowires - Implementations and Applications*”, Chapter 24 - “*Field Emission from Nanowires*”, Dilip S. Joag, Mahendra A. More, Farid Jamali Sheini, InTech, **2011**.
63. R. H. Fowler, L. Nordheim, *Proc. R. Soc. Lond. A*, **1928**, 119, 173 – 181.
64. (a) Robert Gomer, “*Field Emissions and Field Ionization*”, Harvard University Press, Massachusetts, **1961** (b) Robert Gomer, *Surface Science*, **1994**, 299/300, 129-152.
65. C. J. Lee, T. J. Lee, S. C. Lyu, and Y. Zhang, H. Ruh, H. J. Lee, *Appl. Phys. Lett.*, **2002**, 81, 3648 – 3650.
66. Yunho Baek, Yoonho Song, Kijung Yong, *Adv. Mater.*, **2006**, 18, 3105–3110.
67. Z. Wang, J. Gong, Y. Su, Y. Jiang, S. Yang, *Cryst. Growth Des.*, **2010**, 10, 2455–2459.
68. (a) Hua Tong, Shuxin Ouyang, Yingpu Bi, Naoto Umezawa, Mitsutake Oshikiri, Jinhua Ye, *Adv. Mater.*, **2012**, 24, 229–251 (b) M. Nageeb Rashed, “*Organic Pollutants - Monitoring, Risk and Treatment*”, InTech Publishers, **2013**.
69. Ken-ichi Okamoto, Yasunori Yamamoto, Hiroki Tanaka, Masahi Tanaka, Akira Itaya, *Bull. Chem. Soc. Jpn.*, **1985**, 58, 2015–2022.

70. Hua Wang, Tingting You, Weiwei Shi, Jinghong Li, Lin Guo, *J. Phys. Chem. C*, **2012**, 116, 6490–6494.
71. (a) Jingbo Mu, Bin Chen, Mingyi Zhang, Zengcai Guo, Peng Zhang, Zhenyi Zhang, Yangyang Sun, Changlu Shao, Yichun Liu, *ACS Appl. Mater. Interfaces*, **2012**, 4, 424–430 (b) Mutong Niu, Feng Huang, Lifeng Cui, Ping Huang, Yunlong Yu, Yuansheng Wang, *ACS Nano*, **2010**, 4, 681–688.
72. (a) Jiaguo Yu, Yaorong Su, Bei Cheng, *Adv. Funct. Mater.*, **2007**, 17, 1984–1990 (b) Fang Lu, Weiping Cai, Yugang Zhang, *Adv. Funct. Mater.*, **2008**, 18, 1047–1056.
73. Miller, E. L., “*Solar Hydrogen Production by Photoelectrochemical Water Splitting: The Promise and Challenge*”, in “*On Solar Hydrogen & Nanotechnology* (ed L. Vayssieres)”, John Wiley & Sons, Ltd, Chichester, UK, **2010**.
74. (a) Allen J. Bard, Marye Anne Fox, *Acc. Chem. Res.*, **1995**, 28, 141–145 (b) Antonio Currao, *Chimia* **2007**, 61, 815–819 (c) Roel van de Krol, Yongqi Liang, Joop Schoonman, *J. Mater. Chem.*, **2008**, 18, 2311–2320 (d) J. Nowotny, C.C. Sorrell, T. Bak, L.R. Sheppard, *Solar Energy*, **2005**, 78, 593–602 (e) Xiaobo Chen, Shaohua Shen, Liejin Guo, Samuel S. Mao, *Chem. Rev.*, **2010**, 110, 6503–6570.
75. T. Bak, J. Nowotny, M. Rekas, C.C. Sorrell, *International Journal of Hydrogen Energy* **2002**, 27, 991 – 1022.
76. Bruce D. Alexander, Pawel J. Kulesza, Iwona Rutkowska, Renata Solarska, Jan Augustynski, *J. Mater. Chem.*, **2008**, 18, 2298–2303.
77. (a) Michael Grätzel, *Nature*, **2001**, 414, 338 – 344 (b) Krishnan Rajeshwar, Robert McConnell, Stuart Licht, “*Solar Hydrogen Generation: Toward a Renewable Energy Future*”, Springer New York, **2008** (c) Krishnan Rajeshwar, “*Fundamentals of Semiconductor Electrochemistry and Photoelectrochemistry*” *Encyclopedia of Electrochemistry*, **2007**.

Chapter 2

Experimental Methods and Characterization Techniques

This chapter presents a brief description of nanomaterials synthesis and thin film deposition methods employed in the research work. The deposition methods include electrochemical and pulsed laser deposition. This is followed by a discussion on various experimental tools employed to characterize the structural, optical and electrical properties of the synthesized nanomaterials.



Section – I

2.I Deposition Techniques

Over the past decades researchers have developed various techniques for synthesis and characterization of nanomaterials. Synthesis of nanomaterials is the most crucial and challenging step for the efficient use of these nanomaterials for several potential applications, as their morphologies and other relevant properties are strongly influenced by the synthesis methods and protocols.

A facile synthesis protocol for multi-functional metal oxides with desirable control on size, shape and phase evolution is still a challenging task for scientists. Soft chemical and electrochemical routes have attracted attention in this context, as they allow precise control over the synthesis parameters throughout the reaction, from the molecular precursors to the final product at low processing temperatures. These routes allow formation of nanomaterials with high purity and compositional homogeneity. The advantages of these approaches include: (i) wet chemical control on oxidation states, (ii) ability to template various nanostructures, (iii) relatively low process cost, (iv) ability to form nano, meso and micron sized particles. In the present research work, electrochemical synthesis method was used to synthesize Copper Oxide nanoneedles. The following section describes the details of the protocols employed.

For many technological applications, materials are needed to be in the form of thin films. Various deposition techniques are known to form thin films of oxide materials such as pulsed laser deposition (PLD), chemical vapor deposition (CVD), DC and RF sputtering, molecular beam epitaxy (MBE), Spray Coating, Spin-coating, etc. In the present research work PLD technique was utilized to form thin films of metal oxides. The following section describes the details of the PLD deposition method and the parameters used for film formation in this work.

2.I.1 Electrochemical Synthesis

Electrochemical synthesis is a very effective technique for the synthesis of anisotropic nanostructures^[1], such as nanorods, nanowires and nanotubes of various material types from metals to polymers^[2,3]. It is a facile and low cost technique, and operates at a low temperature. Electrochemical synthesis is performed by passing

current between two or more electrodes separated by an electrolyte, where an electrochemical reaction occurs between the electrode and the electrolyte leading to the formation of a film on the electrode surface. The reaction is either oxidation or reduction of reactants or the electrode itself; therefore it can be controlled by fine tuning of the operating voltage and/or current passing through the electrodes. Another important parameter that affects the deposition quality and rate is the reaction bath composition. Electrochemical deposition is a low temperature reaction and is generally limited by the boiling point of the electrolyte. The success of the electrochemical synthesis depends on number of factors such as choice of electrochemical bath, mode of deposition – potentiostatic or galvanostatic, temperature, concentration, pH and composition of bath, etc. By controlling these parameters, oxides, hydroxides, nitrides and even ternary oxides can be formed. The only limiting factor is that, the electrochemical deposition / synthesis can be performed only on conducting substrates.

For the synthesis of 1D nanostructures primarily two electrochemical methods are used ^[4]: a) deposition using hard porous templates and b) direct electrochemical synthesis with/without capping agent. The template-assisted process uses a porous template guiding the growth of deposit while the capping agent-assisted process uses the precursor atoms to selectively adsorb onto the specific crystallographic planes to enhance the anisotropic growth in a particular direction. Recently, researchers are trying to synthesize 1-D nanostructures without any template and any surfactants, although it is very difficult to do so because of the isotropic crystallographic structure of the material. However, for the crystalline materials with crystallographic anisotropy, 1-D growth is driven by the different surface energies depending upon the crystal orientation ^[5].

Anodization is one of the electrochemical methods, successively used for the synthesis of TiO₂ nanotubes ^[6]. In our work we have used anodization method in galvanostatic mode in a basic bath for the deposition of copper hydroxide nanowires. This will be discussed in detail in chapter 3.

2.1.2 Pulsed Laser Deposition (PLD)

Among the various techniques known for thin film deposition, Pulsed Laser Deposition is one of the most widely used techniques ^[7 - 9]. It has been used

successfully for wide range of materials', from polymers to superconducting oxides. The success of PLD lies in its simplicity of setup and a great control on the stoichiometry of the film.

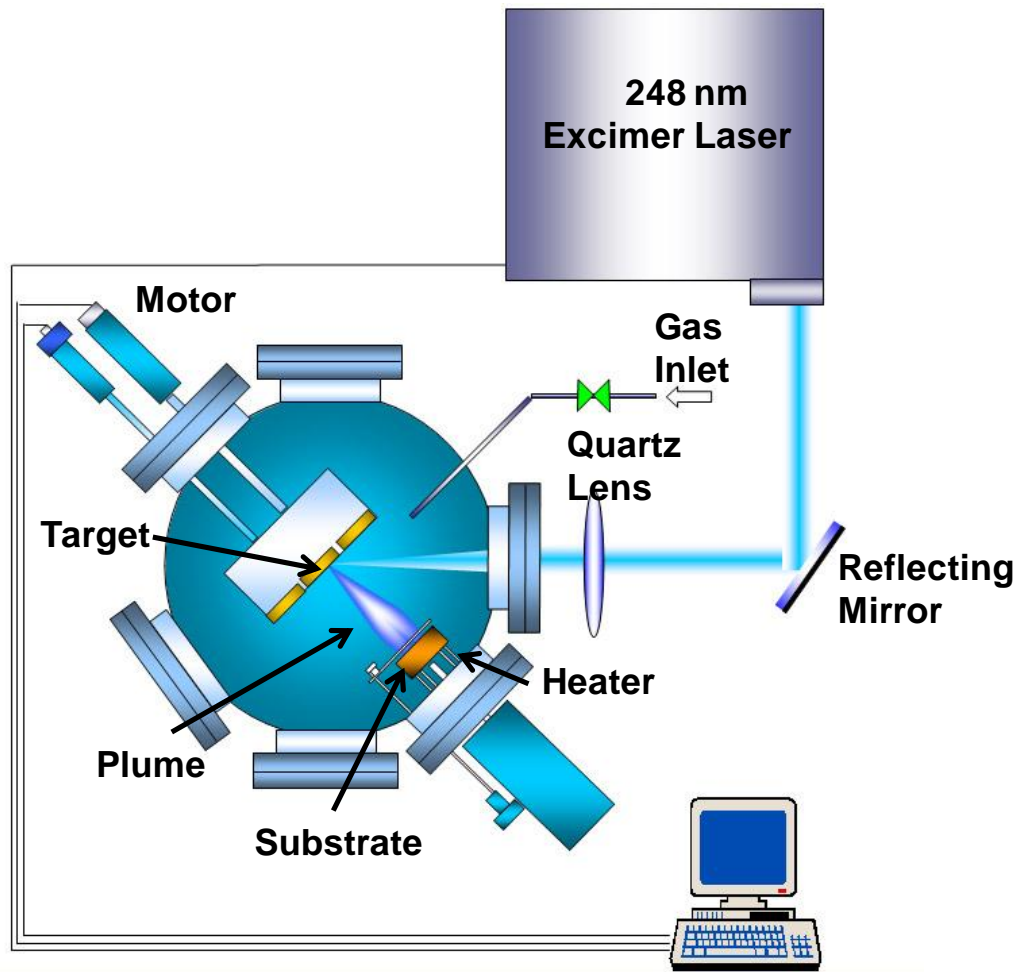


Figure 2.1: Typical schematic of the pulsed laser deposition technique

Pulsed Laser Deposition is a physical vapour deposition method, carried out in a vacuum chamber. The experimental setup, as shown in figure 2.1, consists of a high energy laser source (generally an UV excimer laser like KrF (248 nm), ArF (193 nm) or Nd:YAG laser) and a vacuum chamber (capable of evacuating in the order of $\sim 10^{-6}$ mbar with the help of rotary and turbo molecular pumps). The vacuum chamber is equipped with a rotating target holder (where multiple target mounting is possible for the multilayer deposition) controlled by a motor and a substrate holder, which can be simultaneously heated with the help of a heater controlled by a thermocouple. A gas inlet for inserting reacting gases, such as oxygen is also provided. The laser beam

incident at an angle of 45° to the target surface is focused on to the rotating target (made up of the material to be deposited) with a quartz lens. Laser beams of energy ~ 100 to 400 mJ are focused to a size such that energy density is maintained between 1 to 5 J/cm², at the target. The deposition processes can be controlled by externally connected computer. For the deposition, at sufficiently high laser energy, the target material is ablated to form plasma plume. The plasma plume contains various excited atoms, molecules, ions and small particles. This plasma quickly expands away from the target towards the substrate where it is deposited at the surface of the heated substrate leading to growth of the desired thin film.

There are several parameters, which immensely influence the growth and properties of thin films. These parameters are: laser energy density falling on the surface of the target, ambient pressure during and after deposition, pulse repetition rate, temperature of the substrate, choice and orientation of the substrate itself, target to substrate distance, etc. Laser energy density is a vital factor that hugely affects the properties of the films. The energy density must be selected and controlled according to the target material. If the target is made up of a soft material, such as a polymer, then the energy density should be kept low, so that the polymer chains won't break. While for a ceramic target material, it should be kept little high so that the material will be ablated. In all cases, care should be taken so that droplet-like particles should not get deposited on the substrate, due to very high energy density. The ambient oxygen partial pressure too is vital for the thin film growth of complex oxides to make up the loss of oxygen in the ceramic target itself or during the course of transfer of the excited species from the target to the substrate. The temperature is important to maintain the desired phase and stoichiometry of the film. In spite of having all the mentioned advantages, PLD technique suffers from having difficulty in large area uniform film deposition due to narrow angular distribution of the plasma plume.



Figure 2.2: Photograph of PLD system at National Chemical Laboratory, Pune.

In the present work, a KrF excimer laser (Lambda Physik, LPX200) having 248 nm wavelength and pulse duration of 20 ns was used for thin film deposition. The photograph of the PLD system is shown in figure 2.2.

Section – II

2.II Materials Characterization Techniques

A detail analysis of properties of the nanomaterials and thin films is very crucial in order to employ them for any application. When material's dimensions are reduced to nanoscale they show different properties as compared to their bulk counterparts. Their structural, electronic and optical properties drastically change when the size is reduced. Such changes in the properties can make the analysis complicated at times. Therefore it is very important to select the appropriate characterization technique that will give precise and clear information about the nanomaterials under study. Following sections present the discussion on the various characterization techniques used for the present doctoral work.

To realize the quality and composition of the synthesized material, it is very crucial to characterize the material. Better resolution, higher sensitivity and greater accuracy of characterization tools can give better insights of the materials; hence will be much useful to design appropriate technological devices.

2.II.1 X-Ray Diffraction (XRD)

X-ray crystallography is the most crucial tool for studying structural properties of crystalline material ^[10]. X-ray diffraction (XRD) is a fast, non destructive, analytical technique primarily used for structure, phase identification of a crystalline material and can also provide information on particle / crystallite size. XRD patterns are generated from the interference pattern of elastically dispersed X-ray beams by atom cores. This technique is suitable for thin films, bulk and nanomaterials. In case of nanostructures, the change in lattice parameter with respect to bulk gives idea of nature of strain present in the film.

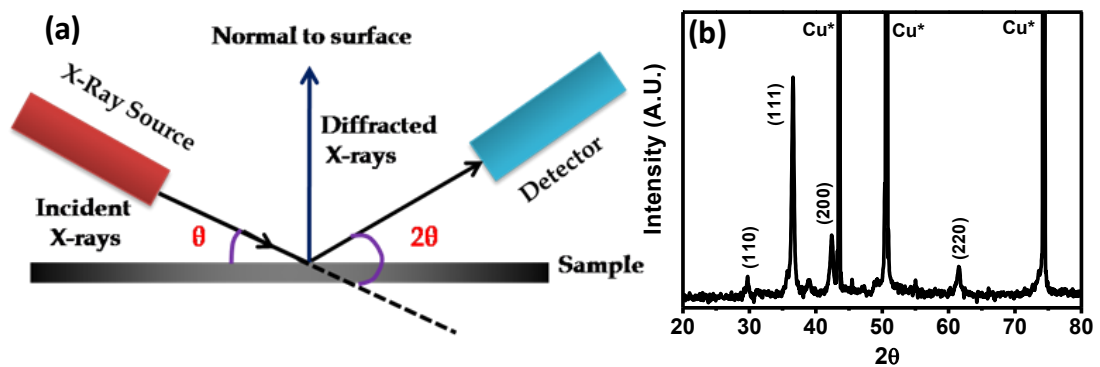


Figure 2.3: (a) Representation of X-ray Diffraction. The θ - 2θ scan maintains these angles with the sample, detector and X-ray source. Only planes of atoms that share this normal will be seen in the θ - 2θ scan. (b) Typical XRD plot of cuprous oxide film on copper substrate

In the XRD instrument, a collimated monochromatic beam of X-rays is incident on the sample. A constructive interference occurs only for certain θ values correlating to those (hkl) plane, where path difference is an integral multiple (n) of wavelength. Based on this, the Bragg's condition is given by ^[11],

$$2d\sin\theta = n\lambda$$

Where, λ is the wavelength of the incident X-ray, d is the inter-planer distance, ' θ ' is the scattering angle and n is an integer-called order of diffraction. In nanostructures, X-rays are diffracted by the oriented crystallites at a particular angle to satisfy the Bragg's condition. Experimentally, we use X-ray with known

wavelength and take readings for different θ values to calculate the inter-planer spacing that satisfies Bragg's condition i.e. for peaks in XRD data. The XRD can be taken in different modes such as θ - 2θ scan mode, θ - 2θ rocking curve, and ϕ scan. In the θ - 2θ scan mode, a monochromatic beam of X-ray is incident on the sample at an angle of θ with the sample surface. The detector motion is coupled with the X-ray source in such a way that it always makes an angle 2θ with the incident direction of the X-ray beam (figure 2.3 (a)). The resulting spectrum is a plot between the intensity recorded by the detector versus 2θ , as shown in figure 2.3 (b), which is a typical XRD plot cuprous oxide film on copper substrate.

The incident X-rays may reflect in many directions but will only be measured at one location so we will require:

$$\text{Angle of Incidence } (\theta_i) = \text{Angle of Reflectance } (\theta_r)$$

This is done by moving the detector twice as fast in (θ) as the source. So, only where $\theta_i = \theta_r$, will be the intensity of the reflected X-rays to be measured.

Nanomaterials have smaller sized crystallites and significant strains due to surface effects, causing considerable peak broadening and shifts in the peak positions w.r.t standard data. From the shifts in the peak positions, one can calculate the change in the d-spacing, which is the result of the change in the lattice constants under strain. The crystallite size (t) is calculated using Scherrer's formula:

$$t = k \lambda / \beta \cos \theta$$

Where, k = Scherrer's Constant ≈ 0.9 , β = Full Width at Half Maximum (FWHM) for a peak at an angle θ .

The only disadvantage of XRD is its less sensitivity towards low-Z materials, thus usually high-Z materials are used. In such cases, electron or neutron diffraction is employed to overcome the low intensity of diffracted X-rays.

In the present work, the XRD pattern for all the samples were recorded at National Chemical Laboratory, Pune using Pan-analytical Philips X'Pert PRO

powder diffractometer. For all the cases, we have used Cu K_{α} X-ray source of wavelength, $\lambda = 1.542 \text{ \AA}$.

2.II.2 Scanning Electron Microscopy (SEM)

Scanning Electron Microscopy allows direct observations of topography and morphological features with high resolution and depth of field than optical microscope. A typical schematic of a SEM is shown in figure 2.4. The three major components of SEM are: the electron column, detector and control console ^[12]. The electron column consists of an electron gun and two or more electron lenses, which influence the path of electrons travelling down an evacuated tube. There are various types of detectors for the detection of various ways in which the electron beam interacts with the sample. The Everhart-Thornley detector is used for detection of secondary electrons, which are the electrons come out from the outer surface of a sample, capable to produce a detail image of the sample's surface morphology. The control console consists of a cathode ray tube viewing screen and computer to control the electron beam. The purpose of electron gun is to provide a stable beam of electrons. There are two types of electron guns: thermionic emission gun and field emission gun. Field emission guns are more preferable since they can produce high primary electron brightness and small spot size even at low accelerating potentials. Generally, tungsten thermionic emitters or Lanthanum hexaboride (LaB_6) coated field emitters are used as electron gun. The spot size from a tungsten gun is too large and requires electron lenses to focus the electron spot on the specimen.

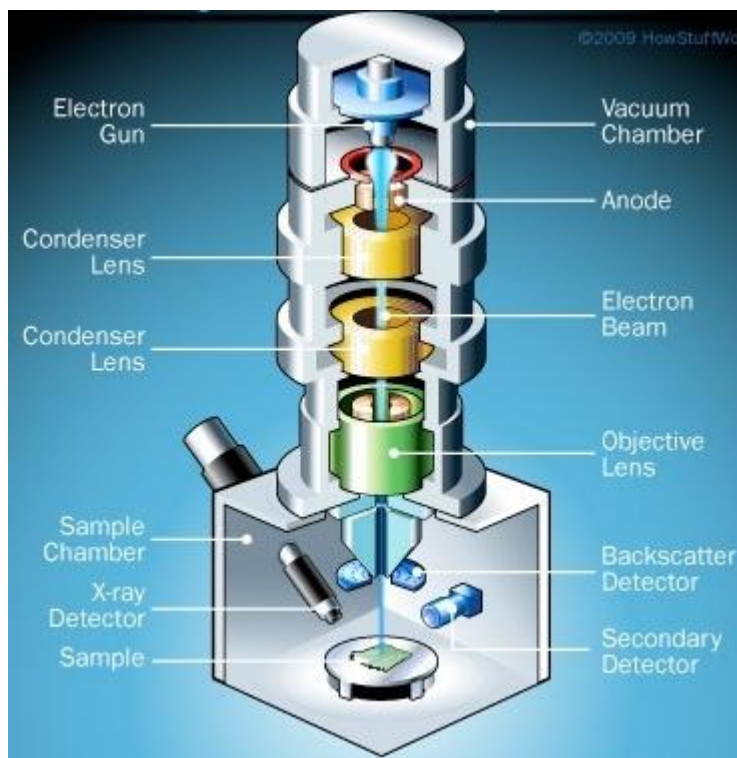


Figure 2.4: Schematic diagram of the Scanning Electron Microscope ^[13]

When the electron beam interacts with the specimen, many types of signals are generated. The two signals most often used to produce SEM images are secondary electrons (SE) and backscattered electrons (BSE). Most of the electrons are scattered at large angles (from 0° to 180°) when they interact with the positively charged nucleus. These elastically scattered electrons usually called 'backscattered electrons' (BSE) are used for backscattered electron imaging. These images provide information about the distribution of different elements in the sample as the intensity of backscattered electrons strongly depends on the atomic number (Z) of the elements in the sample. Some other electrons scatter inelastically due to the loss in kinetic energy upon their interaction with orbital shell electrons. The incident electrons may knock off loosely bound conduction electrons out of the surface of the sample. These are secondary electrons (SE) and are used for SEM topographical imaging.

Both, secondary and back scattered electrons (BSE) are collected when a positive voltage is applied to the collector screen in front of detector. When a negative voltage is applied on the collector screen only BSE signal is captured because the

low energy SE's are repelled. Electrons captured by the scintillator/ photomultiplier are then amplified and used to form an image in the SEM. If the electron beam knocks off an inner shell electron, the atom rearranges by dropping an outer shell electron to an inner one. This excited or ionized atom emits an electron commonly known as the Auger electron. Recently Auger electron spectroscopy (AES) has also been useful to provide compositional information. Here instead of excited atom releasing Auger electron, it can release a photon of electromagnetic radiation. If the amount of energy released is high, the photon will be an X-ray photon. These electrons are characteristic of the sample and can be used for analysis. This type of analysis is known as Energy Dispersive analysis of X-rays (EDAX).

2.II.3 Transmission Electron Microscopy (TEM)

Transmission electron microscopy (TEM) allows to obtain atomic resolution of crystal lattices due to its unique characteristics and hence is one of the most powerful and versatile techniques for the characterization of nanostructured systems. It can also be used to obtain chemical and electronic information at the sub-nanometer scale (with the assistance of energy-dispersive X-ray spectroscopy (EDS) complementary techniques). The line diagram of a typical TEM column is shown in figure 2.5. In TEM, a thin specimen is illuminated with uniform and high intensity electrons. The interaction of an electron beam with a solid specimen results in a number of elastic or inelastic scattering phenomena (backscattering or reflection, emission of secondary electrons, X-rays or optical photons, and transmission of the undeviated beam along with beams deviated as a consequence of elastic – single atom scattering, diffraction - or inelastic phenomena). The TEM technique is dedicated to the analysis of the transmitted or forward-scattered beam. The beam is passed through a series of lenses to obtain the magnified image. The Objective lens mainly determines the final image resolution. In low resolution TEM, the objective aperture is adjusted for selection of the central beam (containing the less-scattered electrons) or of a particular diffracted (or scattered in any form) beam to form the bright-field or dark-field image, respectively. The high resolution TEM (HRTEM) is usually performed in bright-field mode where the image is formed by collecting a few diffracted beams in addition to the central one.

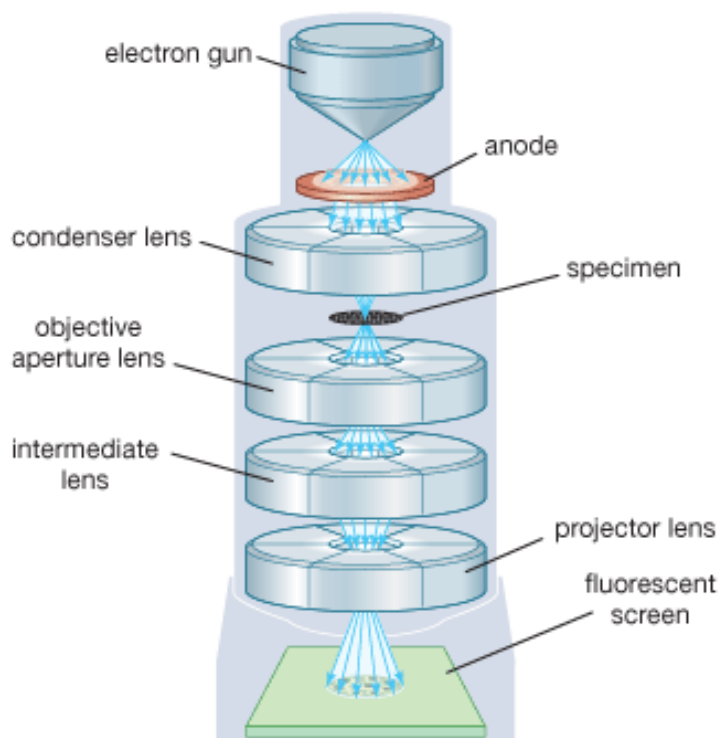


Figure 2.5: Schematic diagram of the Transmission Electron Microscope ^[14].

Angular distribution of scattering electrons can be viewed in the form of diffraction patterns, commonly referred to as selected area electron diffraction (SAED). Spatial distribution of scattering electrons can be observed as contrast in images of the specimen. This arrangement allows direct viewing of the area from which the diffraction pattern arises. Moreover, Kikuchi patterns obtained by inelastic scattering of electrons is also very useful for understanding the crystallographic orientation as these are rigidly attached to a crystal plane and therefore move in the diffraction pattern when the crystal is tilted.

Many materials require extensive sample preparation and thinning procedures to produce a sample thin enough to be electron transparent, and this process may cause some changes in the sample. Therefore sample preparation method should be selected carefully. The field of view in TEM is relatively small, which can raise the possibility that the region analyzed may not be representative of the whole sample. There is always a possibility of the sample getting damaged by the electron beam, particularly in the case of biological materials. Despite these limitations, TEM has been the technique of choice due to the atomic-level resolution leading direct visual

information of size, shape, dispersion and structure. Further, when coupled with SAED, the technique can provide important information on the crystallographic directions in the structures, helpful to understand the growth kinetics^[15, 16].

2.II.4 UV-VIS Spectroscopy

UV-VIS Spectrophotometer presents information about the spectroscopic absorption of light by the material of interest due to electronic transitions^[17]. In semiconductors, when the incident photon energy exceeds the band gap energy of the materials, transition of electrons takes place and corresponding signal is recorded by the spectrometer. In case of metals the surface free electrons vibrate coherently with the incident frequency and resonant absorption takes place. The spectrophotometer can operate in two modes (i) transmission and (ii) reflection mode. For thin films and colloidal nanoparticles well-dispersed in solvent transmission mode is used. For opaque samples diffuse reflectance (DRS) mode is used.

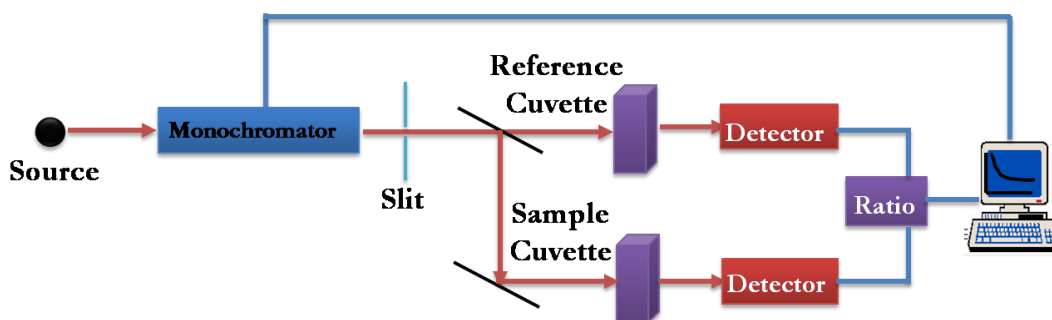


Figure 2.6: Schematics of UV-VIS Spectrophotometer in Transmission Mode

Instrument: The light from the source is alternatively split into one of two beams by a chopper; one beam is passed through the sample and the other through the reference. The detector, which is often a photodiode, alternates between measuring the sample beam and the reference beam. Some double beam instruments have two detectors, and the sample and reference beam are measured at the same time. In other instruments, the two beams pass through a beam chopper which blocks one beam at a time. The schematic of UV-VIS Spectrophotometer in transmission mode has been shown in figure 2.6.

Applications: UV-visible spectroscopy is usually used as a very important analytical tool for the absorption studies of organic compounds such as conjugated polymers and semiconducting, metallic nanomaterials. The wavelength at which maximum absorption occurs (λ_{\max}) provides important information about the organic compounds.

The concentration of desired material in a solution can be determined using Beer-Lambert's law by knowing the molar extinction coefficient. According to Beer-Lambert's law, absorption is proportional the concentration of the substance present in the solution. It can be written as:

$$T = I / I_0 = 10^{-\epsilon cl}$$

Where $T = \text{transmittance} = I / I_0$, I_0 is the intensity of incident radiation and I is the intensity of transmitted radiation, ϵ is a constant for each material known as molar absorption coefficient (or molar extinction coefficient), l is the path length of absorbing material and c is the concentration of the substance present in the solution.

Inverting above equation and taking logarithms,

$$I_0 / I = 10^{\epsilon cl} \text{ or } \log (I_0 / I) = \epsilon cl = A,$$

Where $A = \text{absorbance} / \text{optical density}$

Thus, absorbance is directly proportional to the concentration, where the path length and molar extinction coefficient is suppose to be constant for the particular measurement.

UV-Visible spectroscopy is used to determine band gap (E_g) of semiconductors by using Tauc's plot. The equation for it is given as ^[18, 19]:

$$[F(R)h\nu]^{1/n} \propto (h\nu - E_g)$$

Where $F(R)$ is a modified Kubelka – Munk function,

$$F(R) = \frac{(1 - R)^2}{2R}$$

R is reflectance measured from the DRS of samples and $n=1/2$, for direct band gap material while $n=2$ for indirect band gap material. By plotting the graph of $[F(R)hv]^{1/n}$ vs. hv , we can get the value of band gap (E_g).

The source used for the UV and visible light are deuterium and tungsten lamps respectively and the detector used is usually PMT.

2.II.5 Field Emission Measurements

The field emission current density vs. electric field (J-E) measurements and current vs. time (I-t) measurements were carried in all-metal field emission microscope with load lock chamber, as shown in figure 2.7. The field emission studies were carried out in a planar diode configuration, wherein the sample served as a cathode and a semi-transparent cathodoluminescent phosphor screen (ZnS:Cu Green Color) as an anode. The cathode, pasted onto a sample holder using vacuum compatible conducting silver paste, was held in front of the anode screen at a distance of $\sim 500 \mu\text{m}$.

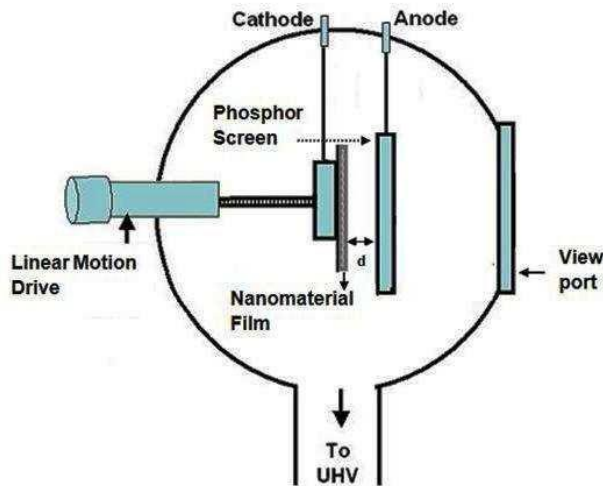


Figure 2.7: Schematic of Field-emission setup

The working chamber was evacuated using an ultra high vacuum system comprising turbo molecular pump, a sputter ion pump and a titanium sublimation pump. The characteristic measurements of the emission current density vs. applied electric Field (J-E), were carried out at 1×10^{-8} mbar pressure using a Keithley 6514

electrometer and a Spellman high voltage DC power supply (0-40kV). Special care was taken to avoid any leakage current by using shielded cables with proper grounding.

2.II.6 Cyclic Voltammetry (CV)

Cyclic voltammetry or CV is a type of potentiodynamic electrochemical measurement and is the most common method used in electrochemistry to obtain information about the properties of the analyte in the solution ^[20]. In a cyclic voltammetry experiment the working electrode potential is ramped linearly versus time as in case of linear sweep voltammetry, however when cyclic voltammetry reaches a set potential, the working electrode's potential ramp is inverted. Thus potential scans are taken for a particular potential window in cyclic manner. The current at the working electrode is plotted versus the applied voltage to give the cyclic voltammogram trace.

A typical Cyclic Voltammogram is shown in figure 2.8. In this case the voltage is swept between two values, starting at V_1 , at a fixed scan rate (measured in V/s). When the voltage reaches V_2 the scan is reversed and the voltage is swept back to V_1 . A typical cyclic voltammogram (figure 2.8) recorded for a reversible single electrode transfer reaction is demonstrated here by plotting the electrode current (i) versus applied potential (E). In a three electrode system, the potential is applied between the reference electrode and the working electrode and the current is measured between the working electrode and the counter electrode. As shown in figure 2.8, the forward scan produces a current peak for the substance that can be oxidized (or reduced depending on the initial scan direction) through the range of the potential scanned. The current will increase as the potential reaches the oxidation potential of the analyte, but then falls off as the concentration of the analyte is depleted close to the electrode surface. If the redox couple is reversible then when the applied potential is reversed, it will reach the potential that will reduce the product formed in the first oxidation reaction, and produce a current of reverse polarity from the forward scan. This reduction peak will usually have a similar shape to the oxidation peak. As a result, information about the redox potential and electrochemical reaction rates of the compounds is obtained. Cyclic Voltammetry provides a wide range of information

about the electrode and electrode/electrolyte interaction and the nature of the cyclic voltammogram depends upon the types of measurements for desired applications.

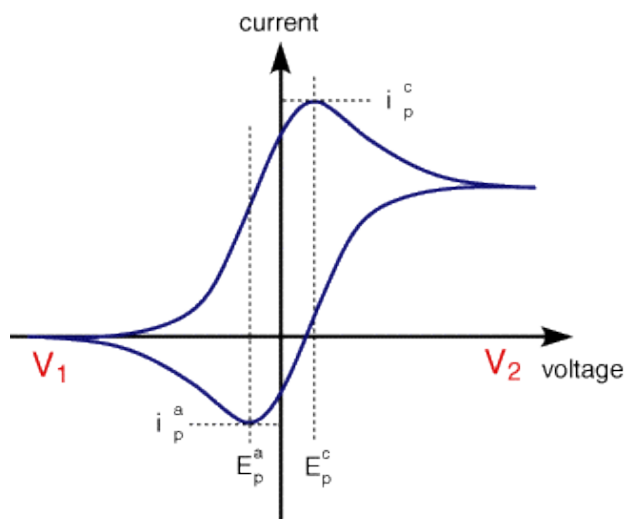


Figure 2.8: A typical cyclic voltammogram (<http://www.ceb.cam.ac.uk/pages/linear-sweep-and-cyclic-voltammetry-the-principles.html>)

In the present research work, we have used the technique of CV for the determination of oxidation potential and current density, to be applied for the anodization process of copper in basic (KOH) solution. We have also used linear sweep voltammetry (LSV) for the photo-electrochemical (PEC) measurements using cuprous oxide as photocathode. The effect of light in a PEC cell is demonstrated in the form of LSV.

2.II.7 Impedance Spectroscopy (IS)

Impedance spectroscopy (IS) is an important tool to understand the interface properties of materials and is popularly used in electrochemistry to obtain information about the solid / liquid interface ^[21]. It can also be used to investigate the dynamics of charges in the interfacial regions of any type of solid or liquid material: ionic, semiconducting, electronic–ionic or even insulators. Dielectric constants and conductivity of bulk materials can also be calculated using IS. Impedance measurements are performed by applying a single-frequency voltage or current to the interface and measuring the phase shift and amplitude, or real and imaginary parts of

impedance at that frequency. The commercial instruments are available which measure the impedance as a function of frequency automatically in the frequency ranges of about 1 mHz to 1MHz and are interfaced to computers.

The total impedance of any electronic circuit containing resistors and capacitor is, $Z = R - iX_c$, which is a complex parameter, as a function of frequency given by,

$$Z(\omega) = Z' - iZ'' \text{ and } Z^2 = (Z')^2 + (Z'')^2$$

where Z' and Z'' are the real and imaginary parts of the impedance, respectively.

The charge transfer reactions at the interface are usually represented in terms of an equivalent circuit composed of a number of single and/or sub-circuit elements containing resistors and capacitors. An example of a simple equivalent circuit representing an electrochemical system is shown in figure 2.9 (a), where the diffusion in the system is represented by a Warberg element (Z_w). Impedance data is presented in three formats: Nyquist plot ($-Z''$ vs. Z'), Bode phase (phase angle ϕ vs. frequency) and Bode modulus ($\text{mod } Z$ vs. frequency). A typical Nyquist plot is shown in figure 2.9 (b) obtained for the system represented by an equivalent circuit shown in figure 2.9 (a). Although having many applications in various fields, impedance technique often suffers due to the failure in appropriate analysis and fitting of proper equivalent circuit.

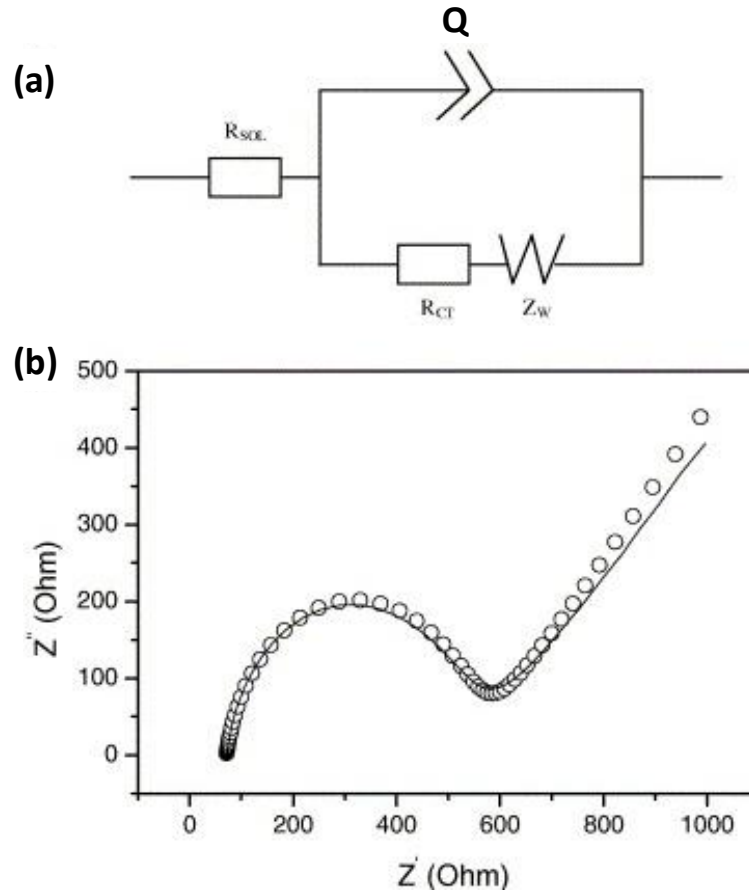


Figure 2.9: (a) Example of equivalent circuit applied to fit the graph obtained in impedance spectroscopy (b) Typical Nyquist plot in case of impedance spectroscopy [Permission taken from Elsevier ref. 22].

Mott-Schottky Plot is used to investigate the flat band potential of a solid in contact with a liquid. It can be considered as one of the applications of Impedance spectroscopy, where impedance data is recorded at different applied bias voltages. In Mott Schottky plot, $1/C^2$ is plotted against the applied potential. The intercept of linear portion of $1/C^2$ on the x-axis gives the value of the flat band potential, the slope of the curve gives the charge carrier density, and the width provides information of space charge layer. It also gives information about type of majority carriers (p or n) in a semiconducting solid.

2.III References

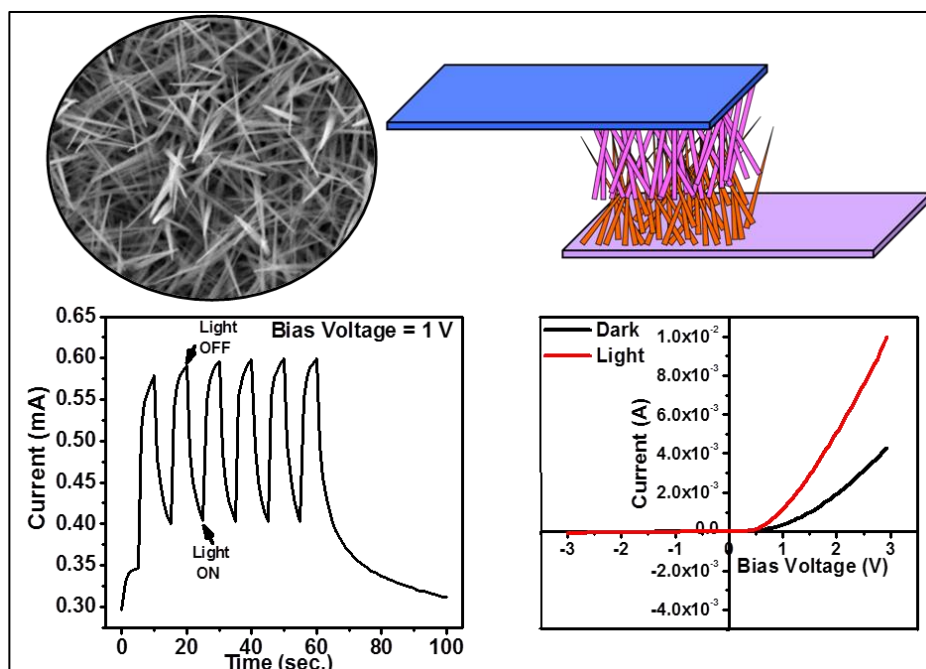
1. Xue-Jun Wu, Feng Zhu, Cheng Mu, Yongqi Liang, Lifen Xu, Qingwei Chen, Ruizhi Chen, Dongsheng Xu, *Coordination Chemistry Reviews* **2010**, 254, 1135–1150.
2. Dacheng Yang, Guowen Meng, Shuyuan Zhang, Yufeng Hao, Xiaohong An, Qing Wei, Min Ye and Lide Zhang, *Chem. Commun.*, **2007**, 1733–1735.
3. G. Helen Annal Therese and P. Vishnu Kamath, *Chem. Mater.* **2000**, 12, 1195-1204.
4. Guangwei She, Lixuan Mu and Wensheng Shi, *Recent Patents on Nanotechnology* **2009**, 3, 182-191.
5. J. Elias, R. Tena-Zaera, C. Le´vy-Cle´ment, *Journal of Electroanalytical Chemistry* **2008**, 621, 171–177.
6. Jan M. Macak, Hiroaki Tsuchiya, Luciano Taveira, Saule Aldabergerova, and Patrik Schmuki, *Angew. Chem. Int. Ed.*, **2005**, 44, 7463 –7465.
7. “*Pulsed Laser Deposition of Thin Films: Applications-Led Growth of Functional Materials*”, edited by Robert Eason, Wiley-Interscience A John Wiley & Sons, Inc., Publication, Hoboken, New Jersey, **2007**
8. M S Hegde, *Proc. Indian Acad. Sci. (Chem. Sci.)*, **2001**, 113, 445–458.
9. “*Pulsed Laser Deposition of Thin Films*”, edited by D. B. Chrisey, G. H. Hubler, Wiley Interscience Publication, NewYork, **1994**.
10. Wyckoff, R. W. G. *Crystal Structures, 2nd ed.*; Wiley: New York, **1964**
11. “*Elements of X-Ray Diffraction*”, B. D. Cullity, Addison-Wesley Publishing Company, Inc., Massachusetts, **1956**.
12. G. Lawes, “*Scanning electron microscopy and X-ray microanalysis: Analytical chemistry by open learning*”, John Wiley & sons, **1987**.
13. Atteberry, Jonathan. "How Scanning Electron Microscopes Work" 21 April **2009**. HowStuffWorks.com <<http://science.howstuffworks.com/scanning-electron-microscope.htm>> 13 September 2013.
14. "Transmission electron microscope". Art. Encyclopaedia Britannica Online. Web. 13 Sep. **2013**. <<http://www.britannica.com/EBchecked/media/110686/Transmission-electron-microscope>>

15. J. Duan, S. Yang, H. Liu, J. Gong, H. Huang, X. Zhao, R. Zhang, Y. J. Du, *Am. Chem. Soc.*, **2005**, *127*, 6180.
16. Y. Ding, Z. L. Wang, *J. Phys. Chem. B.*, **2004**, *108*, 12280.
17. “*Fundamentals of UV-visible spectroscopy*”, Tony Owen, *Hewlett-Packard publication*, Germany, **1996**.
18. Ziyauddin Khan, Momina Khannam, Natarajan Vinothkumar, Mahuya De and Mohammad Qureshi, *J. Mater. Chem.*, **2012**, *22*, 12090.
19. Yoshitaka Nakano, Shu Saeki, and Takeshi Morikawa, *Applied Physics Letters*, **2009**, *94*, 022111.
20. “*Electrochemical Methods Fundamentals and Applications*”, Allen J. Bard Larry R. Faulkner, *John Wiley & Sons, Inc.*, USA, **2001**.
21. “*Impedance Spectroscopy Theory, Experiment, and Applications*” Edited by Evgenij Barsoukov J. Ross Macdonald, Second Edition, Wiley-Interscience A John Wiley & Sons, Inc., Publication, **2005**.
22. Haizhen Huang, Zhigang Liu, Xiurong Yang, *Analytical Biochemistry*, **2006**, *356*, 208–214.

Chapter 3

Strong Photo-Response in a Flip-Chip Nanowire p-Cu₂O/n-ZnO heterojunction

Cu₂O nanoneedles are synthesized on copper substrate by a simple anodization and reducing ambient annealing protocol. ZnO nanorods are grown on ITO coated glass by a low temperature chemical route. The electronic and photo-response properties of the p-Cu₂O / n-ZnO flip-chip heterojunction are then studied and analyzed. We show that the I-V characteristic is rectifying and the junction exhibits a good photoresponse (~120% under 1V reverse bias) under AM 1.5 1 Sun illumination. This nano-heterojunction photo-response is far stronger as compared to that of pulsed laser deposited thin film p-Cu₂O/n-ZnO heterojunction, which can be attributed to higher junction area in the former case.



Ref.: Meenal Deo *et. al.*, *Nanoscale*, **2011**, 3, 4706

3.1 Introduction

Energy harvesting using non-silicon and earth abundant materials is an increasingly sought after goal of the scientific community at the present time. Metal oxides are considered to be the potentially interesting candidates in this respect since the range of electronic and optical properties they support are truly exceptional. Unfortunately it has not been easy to control the stoichiometry and defect states in the case of oxides and this has held back the development of the field of oxide electronics for several years. Over the years the techniques and controls have improved dramatically and it is envisaged that in the next few years significant progress will occur in this field. ZnO and TiO₂ are the abundant work-horse oxide materials that have been used in several applications and are n-type. Relatively less number of oxides is p-type and Cu₂O is one of them. Hence it is of interest to find out ways of creating functional p-n junctions using these oxides and examine their optoelectronic properties, because many devices such as solar cells, photo-detectors, emitters etc. can be based on p-n junctions. Eventual goal of these efforts is of course to push for efficient solar cell designs. This is non-trivial because one may have to engineer surfaces suitably and control defects to avoid recombination effects. Yet beginning needs to be done towards such a goal, and the present study is a modest attempt along this line.

Cuprous oxide (Cu₂O) is one of the few p-type direct band gap metal oxide based semiconductors (Band gap ~2.17 eV). Because of its distinct properties, Cu₂O has attracted interest as a good candidate material for photo-catalysis, Li-ion batteries, solar cells, Photo-electrochemical cell, photo-sensor etc. ^[1-5]. Among various nanostructures, quasi 1D nanostructures (nanorods, nanowires, nanotubes) have been attracting quite an attention recently because of their potential applications ^[6]. In the context of electronic charge transport such quasi 1D nano-structures provide a direct pathway for efficient and confined charge transport along with surface accessibility, which is useful in making functional devices at the nanoscale. There are a few reports on the synthesis of quasi 1D Cu₂O nanostructures by solution processing methods ^[7, 8] but relatively much less effort has been expended on their evaluation in the context of device science.

In this work a simple protocol is demonstrated for the synthesis of Cu₂O with nanoneedle morphology involving anodization of copper and its consequent vacuum annealing. ZnO nanorods are also grown on ITO coated glass by a simple chemical route. The electronic and photo-response properties of p-Cu₂O nanoneedle / n-ZnO nanorod flip-chip junction are then examined. The junction shows a rectifying diode type behavior, as expected. This nanowire heterojunction device is shown to exhibit considerably stronger response as compared to that of a thin film heterojunction due to substantial increase in interfacial area. The reported study of photo-response of the p-Cu₂O/n-ZnO nanowire junction can be applied for photo-detector application.

3.2 Experimental

3.2.1 *Synthesis of Cu₂O Nanoneedles on Copper and ZnO nanorods on ITO/Glass*

The Cu₂O nano-needle film is grown directly on copper substrate by anodization of copper itself followed by annealing at 450°C in controlled oxygen pressure (5×10^{-6} mbar). For anodization, aqueous solution of 2M KOH was used as the electrolyte in an electrochemical cell. High purity polycrystalline copper foil, polished with fine grade polish paper was used as working electrode (5 cm x 1 cm x 0.1 mm) and a graphite rod as a counter electrode. The deposition was carried out at an applied constant current density of ~ 7 mA/cm² and the growth time was kept around 5 min. By anodization, we get evenly spread Cu(OH)₂ nanoneedles film on the Cu substrate which on annealing in vacuum gets converted into Cu₂O nanoneedles.

ZnO nanorods on ITO substrate were synthesized by wet chemical process^[9, 10]. First, the ZnO seed layer was prepared by spin coating 5 mM zinc acetate in ethanol on clean ITO at the rotation speed of 2500 rpm for 30 sec, followed by annealing at 300 °C for 1h for better adherence of ZnO nanoparticles which act as nucleating sites for the growth of ZnO nanorods. For facile growth of ZnO on the seeded surface of ITO, an equimolar (25 mM) solution of Zn(NO₃)₂ and hexamethylene tetramine (HMT) and 5 mM polyethylenimine (PEI) was used for the reaction. The reaction was carried out in a closed container at 95°C while stirring simultaneously for 2 hours. After the reaction was complete, the grown ZnO NRs were thoroughly rinsed with Milli-Q water and dried in air to remove residual polymer. Finally, the

deposited samples were kept for annealing at 300 °C for 1h for better adherence of ZnO nanorods on the substrates.

3.2.2 Thin Film Deposition of Cu₂O & ZnO by PLD

The thin films of p-Cu₂O and n-ZnO were deposited on copper and ITO substrates respectively by Pulsed Laser Deposition (PLD) technique. Copper oxide (CuO) and Zinc Oxide (ZnO) pellets were used as the target materials for laser ablation using KrF laser (wavelength $\lambda=248$ nm, pulse width of 20 ns). The distance between the target and the substrate was kept 5 cm. The pulse repetition rate was fixed at 10 Hz for both ZnO and Cu₂O depositions. The deposition of ZnO on ITO coated glass substrate was carried out at room temperature and the oxygen partial pressure was kept at 1×10^{-1} mbar. The deposition of Cu₂O on copper substrate was also carried out at 300°C and at 5×10^{-6} Torr background pressure in order to avoid the oxidation of Cu₂O into CuO. The thickness was kept ~50 nm for both films. The p-Cu₂O/n-ZnO thin film heterojunction was formed by flip-chip method just like in case of nanowires heterojunction for the comparison.

3.2.3 Characterization

Various techniques such as X-ray diffraction (XRD, Philips X'Pert PRO), Scanning Electron Microscopy (SEM, FEI Quanta 200 3D), High-Resolution Transmission Electron Microscope (HR-TEM, FEI Tecnai 300), X-ray photoelectron spectroscopy (XPS, VG scientific ESCA-3000 spectrometer), Electrochemical Impedance Spectroscopy (EIS, Autolab PGSTAT30 (Eco-Chemie)) were used to characterize the samples. All the IS data were analyzed by using ZView software. I-V measurements were taken using Keithley 2400-C source meter. Solar simulator (Newport) at 100 mW/cm^2 (1 sun AM 1.5 G) was used for illumination of photodiode.

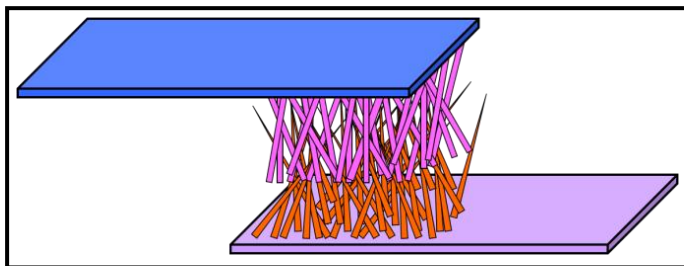


Figure 3.1: Schematic diagram of the Cu₂O/ZnO nanowire heterojunction

The p-n heterojunction of these p-Cu₂O nanoneedles was formed with n-ZnO nanorods by flip-chip method as shown in the figure 3.1. We found that the device can withstand around 1.5×10^5 N/m² pressure exceeding which it gets damaged (short). We therefore restricted to a pressure value fairly lower than this threshold, yet giving a firm enough and reproducible contact which gave the overall junction resistance of the order of about 15-25 k Ω . The measured pressure in this case was about 2.5×10^4 N/m². We did not use any specific instrument for the purpose and all the measurements are performed at room temperature. For the photoresponse measurement the light was incident on this flip-chip geometry from the transparent (ITO) side.

3.3 Results and Discussion

3.3.1 Study of copper in basic solution

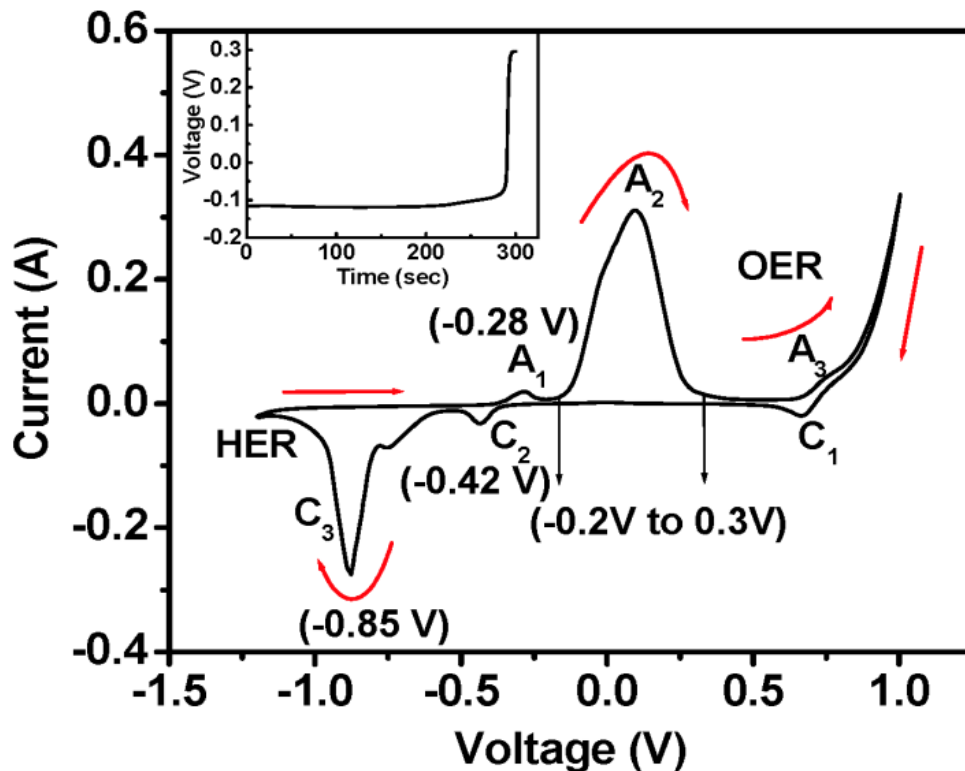


Figure 3.2: Cyclic Voltamogram recorded for copper electrode in aqueous solution of 2M KOH. Inset shows voltage – time curve during the deposition process at constant applied current density 7 mA/cm².

Prior to the deposition of Cu₂O nanoneedles, the Cu(OH)₂ nanoneedles were first deposited on copper in basic solution of 2M KOH. In order to study the behavior of polycrystalline copper in aqueous solution of 2M KOH, Cyclic Voltammogram (CV) was recorded as shown in figure 3.2. The CV shows the successive anodic (A₁, A₂, A₃) and cathodic (C₁, C₂, C₃) peaks, which can be assigned to various redox processes. During the positive sweep starting at -1.2 V (hydrogen evolution reaction, HER potential), Cu⁰ is first oxidized at -280 mV into Cu₂O (peak A₁). The subsequent feature A₂ which appears as a doublet at -13 mV and 94 mV, is due to the oxidation of Cu₂O into Cu (II) to form a CuO/Cu(OH)₂ duplex film. Increase in the voltage from -0.2V increases the formation of cuprate ion in the form of the complex Cu(OH)₄²⁻ at the substrate/electrolyte interface ^[11] creating nucleating sites on the copper substrate. Due to the negative charge on Cu(OH)₄²⁻, it readily gets attracted towards copper anode, where this complex precipitates forming Cu(OH)₂ film on Cu. Since our interest in the present work was to grow needles of Cu(OH)₂ for subsequent processing to convert them to Cu₂O, we optimized galvanostatic preparative parameters (current density and potential drop across the electrode) to yield evenly spread, thick film of Cu(OH)₂ nanoneedles on the copper surface. The deposition process was monitored by voltage-time curve as shown in the inset of figure 3.2, which is the change in voltage during the deposition at applied constant current density of ~7 mA/cm². The constant voltage during the deposition implies evenly spread film formation on the surface and the growth time is around 300 sec. Thereafter potential drop increases suddenly from about -0.11 to 0.3 V due to increase in the resistance of the anode and evolution of oxygen takes place on the anode. Thus, the deposition is stopped within 5 minutes. The film is washed in MilliQ water and dried in air. The formation of Cu(OH)₂ on Cu was confirmed by XRD and the needle-like morphology by SEM, as shown in figure 3.3 (a) and (b) respectively. This film was annealed at 450°C in vacuum (~10⁻⁶ mbar) for 1 hr in order to fully convert Cu(OH)₂ nanoneedles to Cu₂O nanoneedles.

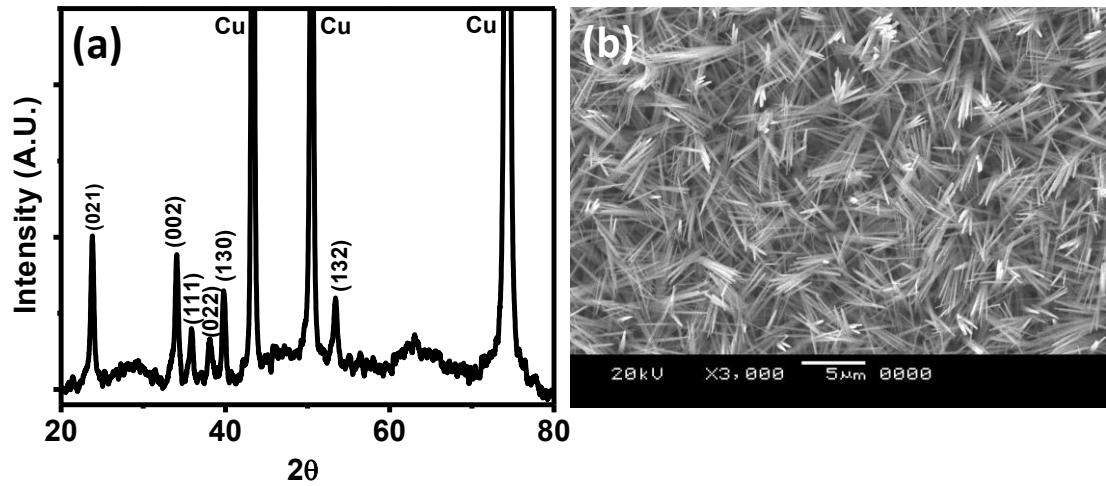


Figure 3.3: (a) XRD and (b) SEM image of as prepared Cu(OH)₂ nanoneedles on copper substrate

3.3.2 Characterization of Cu₂O Nanoneedles

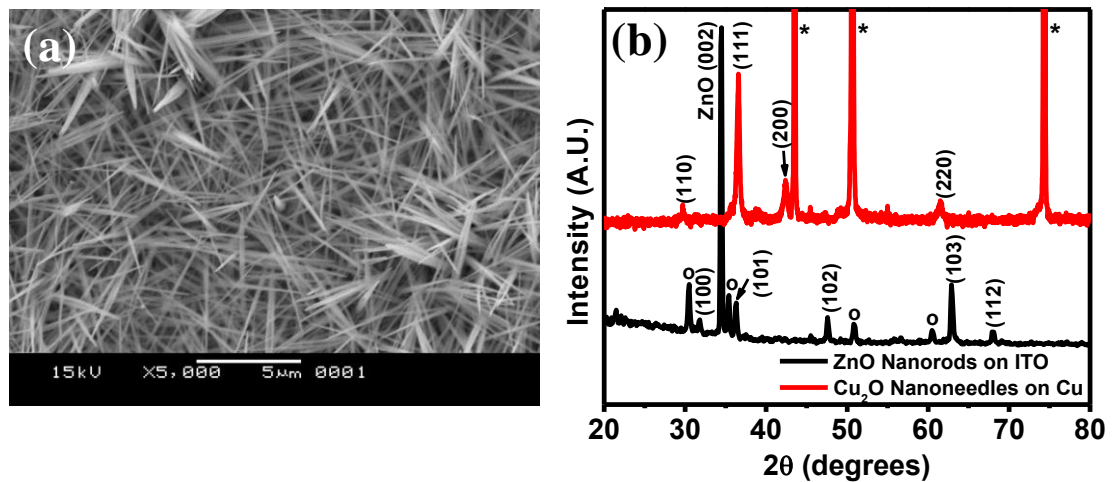


Figure 3.4: (a) SEM image showing Cu₂O Nanoneedles grown on copper substrate. (b) XRD pattern of Cu₂O nanoneedles and ZnO nanorods. '*' indicates copper substrate peaks and 'o' indicates ITO substrate peaks in case of Cu₂O and ZnO films respectively.

Figure 3.4 (a) shows scanning electron micrograph (SEM) of a Cu₂O nanoneedles film on Cu. From the SEM image it is clearly observed that the whole surface of the sample is comprised of dense array of needlelike morphology with tapering ends. The X-ray Diffraction (XRD) patterns of Cu₂O nanoneedles on Cu and ZnO nanorods on ITO shown in figure 3.4 (b) establish the phase pure nature of the respective, nanomaterials.

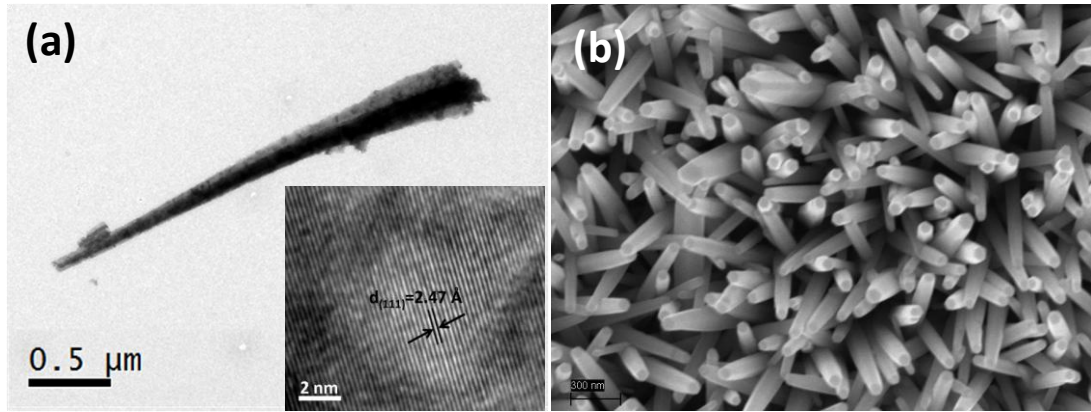


Figure 3.5: (a) TEM image of single Cu₂O nanoneedle. Inset shows lattice fringes of Cu₂O nanoneedle (b) SEM image showing ZnO nanorods on ITO coated glass substrate

The TEM image of single Cu₂O nanoneedle is shown in the inset of figure 3.5 (a). This shows that the needle is ~2.5 μm in length. Inset of figure 3.5 (a) shows high resolution TEM micrograph of the Cu₂O nanoneedle. From the HRTEM image the inter-planer distance is about 0.247 nm, which matches exactly with the (111) family of planes of Cu₂O (PDF # 782076), as also indicated by the XRD data. The SEM image of ZnO nanorods grown on ITO is shown in figure 3.5 (b), which shows the formation of the hexagonal rods of diameter ~100 nm evenly distributed on ITO substrate.

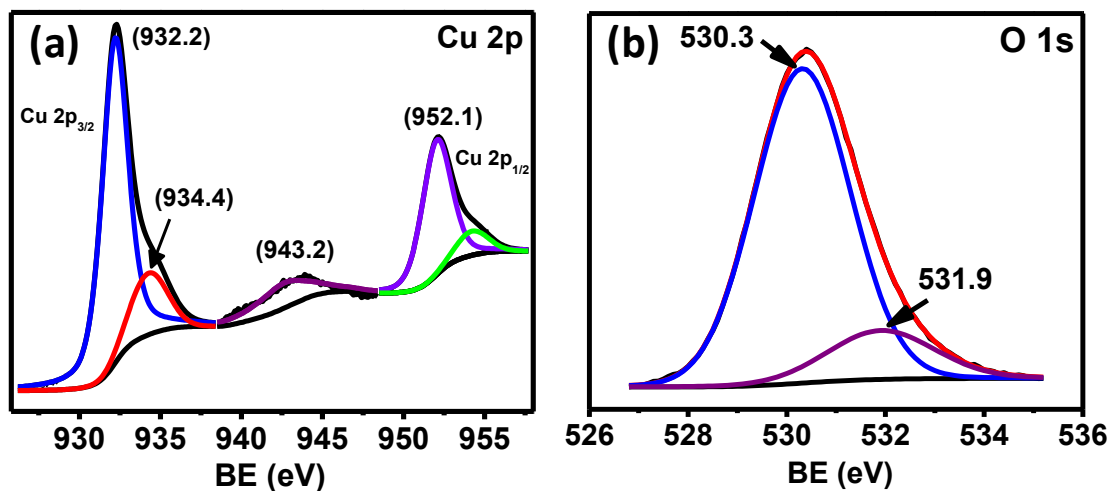


Figure 3.6: XPS spectra of Cu₂O nanoneedles corresponding to (a) Cu 2p (b) O 1s

The compositions and purity of the as-synthesized Cu₂O films were further examined with X-ray photoelectron spectroscopy (XPS), and these results are shown in Figure 3.6. The XPS spectrum of Cu 2p as shown in figure 3.6 (a) exhibit peaks at 932.2 eV and 952.1 eV corresponding to Cu 2p_{3/2} and 2p_{1/2} respectively, is in good agreement with data observed for copper (I) oxide ^[12]. The occurrence of a weak satellite feature on the higher binding energy (943.2 eV) side of the Cu 2p main peak indicates slight presence of CuO on the surface. The observed amount of CuO is very tiny due to the slightly oxidized surface of Cu₂O nanoneedles due to their exposure to the atmosphere. This may also be the reason for the effective stability of the Cu₂O needle phase. The O 1s core level spectrum, as observed from figure 3.6 (b), shows the main peak at the energy of 530.3 eV is characteristic of Cu-O lattice formation in Cu₂O. The peak of 531.9 eV is attributed to adsorbed oxygen on the surface of Cu₂O nanoneedles. All of these results bear out that the sample is just composed of Cu₂O.

3.3.3 *Electrical properties of p-Cu₂O/n-ZnO heterojunction*

The energy band diagram of Cu₂O/CuO/ZnO junction based on Anderson's Model ^[13] is shown in Figure 3.7 (a). The formation of ultrathin CuO on the surface of Cu₂O nanoneedles on the exposure to atmosphere also leads to the change of the interface between Cu₂O and ZnO. This change has been taken into account by drawing the band diagram. The effective ΔE_c of the Cu₂O/CuO/ZnO junction is ~1 eV. The conductivity of CuO being less than that of Cu₂O one may think of it as a resistive (semi-insulating) layer between the Cu₂O and ZnO layers. However the charge transfer between the end layers, which is critical to the photo-response, is not be affected much because of the favorable band alignment of Cu₂O/CuO/ZnO layer system. Hence, hereafter the Cu₂O/CuO/ZnO junction is mentioned as a p-Cu₂O/n-ZnO junction.

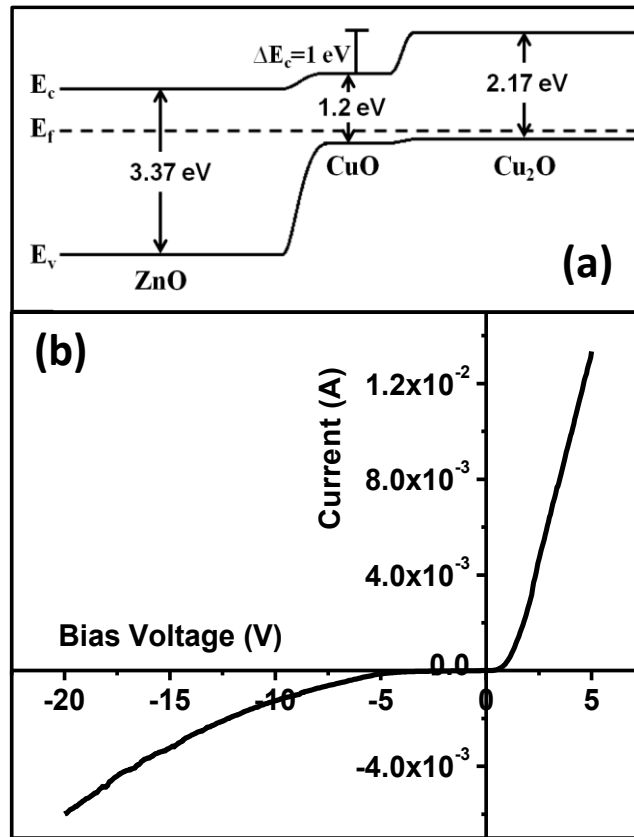


Figure 3.7: (a) Energy band diagram of Cu₂O/CuO/ZnO heterojunction (b) I-V characteristics of the Cu₂O/ZnO nanowire heterojunction

The junction of Cu₂O nanoneedles on copper substrate and ZnO nanorods on ITO substrate was made by simple flip-chip method, as shown in figure 3.1, where copper is the back contact and ITO is the front contact of the device for optical access. Electrical properties of the device were studied using I-V characteristics in CPP (Current perpendicular to plane) configuration. Figure 3.7 (b) shows the full dark I-V characteristics of the device. The device shows rectifying behavior with rectification ratio ($I_{\text{forward}} / I_{\text{reverse}}$) of about 200 at 3V and about 100 at 5 V in the dark, indicating the formation of a p-n junction diode. The turn-on voltage and the reverse leakage current values of the device are found to be 1.1 V and 1.35×10^{-4} A at -5 V, respectively. In the forward bias, electrons should experience a barrier equivalent to ΔE_c which is equal to 1 eV in this case, as shown in figure 3.7 (a). Hence Ohmic behavior is expected above 1.1 V. The I-V characteristics also indicate that there is

no sharp breakdown of the device; however it shows an increase in current from -5 V.

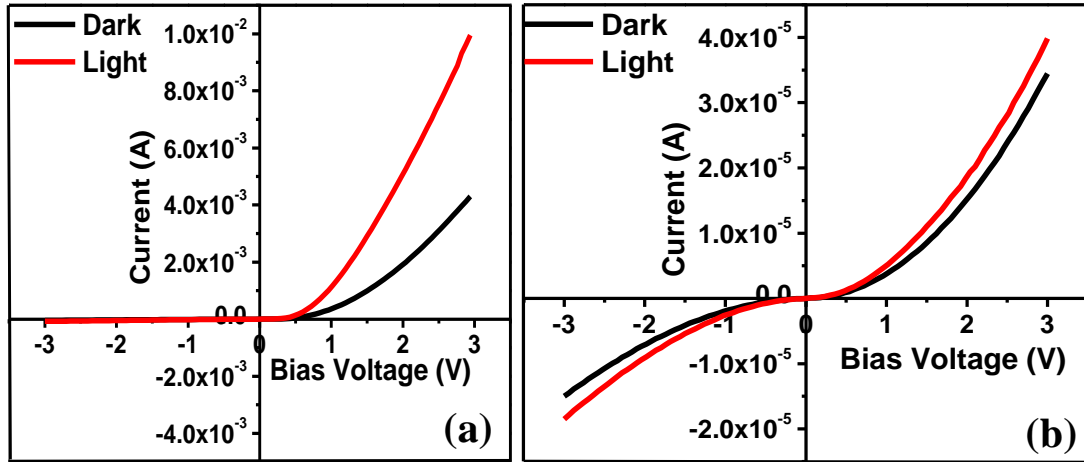


Figure 3.8: I-V characteristics of the Cu₂O/ZnO heterojunction in dark and under illumination for (a) nanowire junction and (b) thin film junction

Figure 3.8 (a) shows the I-V characteristics of the ZnO/Cu₂O p-n nanowire heterojunction both in the dark and under AM 1.5 i.e. 100 mW/cm² illumination. It is found that under reverse bias condition, no significant change in the current takes place after illumination. On the other hand, the current under forward bias increases drastically. Under illumination, the electron-hole pairs are generated due to absorption of photons with photon energy higher than the band gap of semiconducting material. Clearly in our case the electron-hole pairs are primarily generated from Cu₂O with photon energy greater than about 2.1 eV implying that the photo-generated carriers mainly emanate from Cu₂O. Thus enhanced photocurrent is due to the photo-generated charge carriers. We have tested about 10 devices checking each device at least 5 times. The photo-response of these devices was within $\pm 10\%$.

Figure 3.8 (b) shows the I-V characteristics of the ZnO/Cu₂O PLD thin film heterojunction. From comparison of figures 3.8 (a) and (b), it is clear that the overall generation of current (both dark and illumination current) in case of thin film junction is less than that of nanowire junction by about two orders of magnitude. Less dark current in case of Cu₂O-ZnO thin film junction can be attributed to small

interfacial area as compared to nanowire heterojunction. Figure 3.8 (a) also shows significant increase in the junction current on illumination due to the contribution of the photocurrent. Due to higher surface area of both the nanomaterials and thereby the large interfacial area between the Cu₂O/ZnO nanowires the generation of charges at the interface will be much more as compared to the corresponding planar thin films which would yield significant increase in photocurrent. Therefore we get considerable enhancement in the photocurrent which promotes its use in photodiode mode.

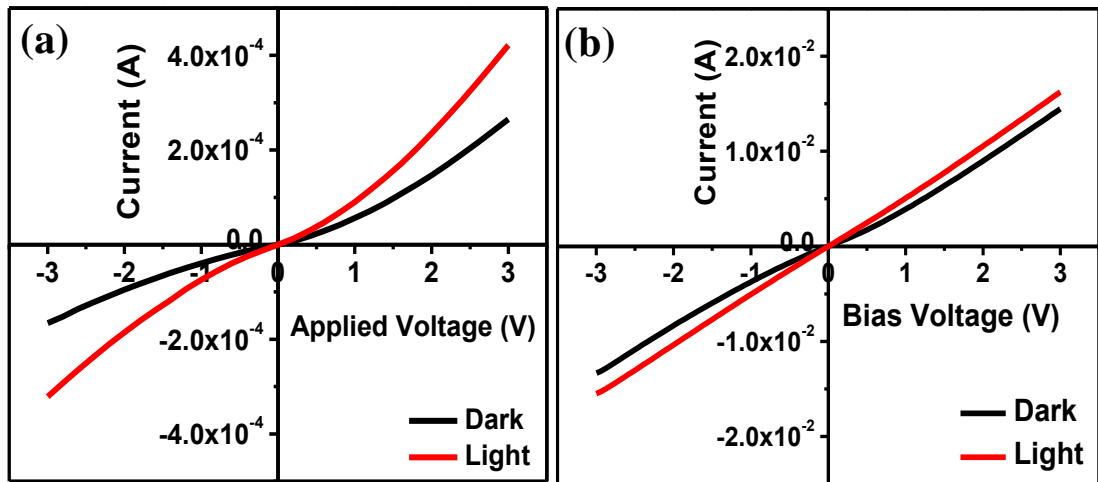


Figure 3.9: I-V characteristics of the (a) Cu₂O/ITO junction and (b) ZnO/Cu junction in dark and under illumination

In order to make sure that the I-V characteristics discussed in the work reflect the Cu₂O/ZnO interface only, and not the Cu₂O/ITO and ZnO/Cu interfaces we made I-V measurements on the Cu₂O nanoneedles flip-chiped with ITO and ZnO nanorods flip-chiped with Cu, and the corresponding results are shown in figure 3.9 (a) and (b) respectively. We observed that the Cu₂O-ITO junction shows a roughly symmetric (Schottky) behaviour, in contrast to the asymmetric behaviour observed in the case of the p-Cu₂O/n-ZnO junction. The nearly symmetric behaviour is probably due to nearly equal work function values of Cu and ITO contacts. In this case, we obtained a photoresponse ~50% in forward as well as reverse bias, which is more than two times weaker than the Cu₂O/ZnO nanowire junction in the reverse bias mode. The I-V characteristics of the ZnO nanorods-Cu junction also show a symmetric behaviour

with very low photoresponse as compared to the p-Cu₂O/n-ZnO junction. Thus we can clearly rule out the possibility of direct shorting between Cu₂O and ITO or ZnO and copper.

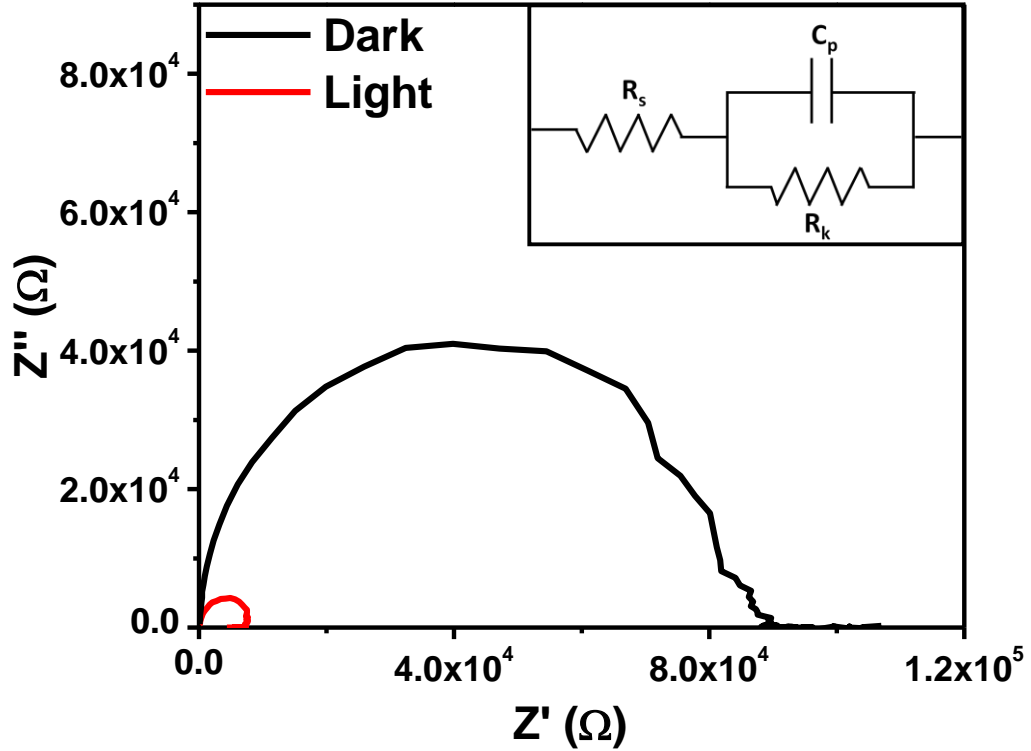


Figure 3.10: Impedance Spectroscopy (IS) Measurements (Nyquist Plot) of p-Cu₂O/n-ZnO nanowire junction for Dark and Light (illuminated) conditions. Inset shows the Equivalent Circuit for the same.

In order to study the electron transport and charge recombination at Cu₂O/ZnO nanowire junction Impedance Spectroscopy (IS) measurements were performed. The frequency range chosen for the measurement was from 10⁻² Hz to 10⁶ Hz with ac amplitude of 10 mV. Figure 3.10 shows the impedance spectrum (Nyquist plot) of the junction in the dark and in the presence of light. Simulated AM1.5 1 Sun illumination was used to measure the photoresponse under light. The figure shows the expected single semicircle corresponding to the Cu₂O/ZnO p-n junction. The enhanced photo-response of Cu₂O/ZnO nanowire junction can be seen from the difference in the impedance spectra of the junction in the presence and absence of light. We have performed fitting and simulation of this data for an equivalent circuit

shown in inset of figure 3.10. The resistance element R_s in the high frequency range over 1 MHz is influenced by the contact resistance between both the contacts which are Cu/Cu₂O and ZnO/ITO. The value of R_s in dark and under light are 128 and 154 ohms, respectively, which implies little change under illumination. Various parameters in the equivalent circuit of Cu₂O/ZnO nanojunction in dark and under illumination are given in table 3.1. The charge transfer resistance value reduces from about 89 k-ohms to about 6.9 k-ohms under illumination. This reduced resistance is a result of photocarriers generated within Cu₂O/ZnO nanojunction under illumination. ω_{\max} is the peak frequency of the semi-circular arc. Inverse of ω_{\max} corresponds to the characteristic time constant, τ of the equivalent RC circuit which indicates the carrier lifetime^[14] within the heterojunction film. Carrier lifetime for p-Cu₂O/n-ZnO nanowire heterojunction reduces under illumination because of various possible recombination pathways (radiative / non-radiative) of photo-generated charge carriers. The carrier lifetime in the illuminated p-Cu₂O/n-ZnO nanowire heterojunction is ~23 μ sec. This carrier lifetime is very low compared to the photovoltaic cells, typically Dye Sensitized Solar Cells, where this value is in the order of few milliseconds^[15]. This low lifetime of charge carriers can be attributed to high density of interfacial states which results in higher rate of recombination. This explains the absence of photovoltaic effect in our case although there are few reports on p-Cu₂O nanoparticles/n-ZnO nanowires junction photovoltaic cell^[16]. In these cases also the efficiency values are low possibly because of high interfacial recombination which is then partially reduced by a thin TiO₂ layer between ZnO and Cu₂O.

	ω_{\max} (kHz)	$\tau = 1/\omega_{\max}$ (10 ⁻³ sec.)	R_s (Ω)	R_k (k Ω)	C_p (10 ⁻¹⁰ F)
Dark	4.53	0.22	128	89	4.4
Light	42.29	0.023	154	6.9	2.7

Table 3.1 Parameters determined by Impedance Spectroscopy Measurements under Dark and Light (illuminated) conditions.

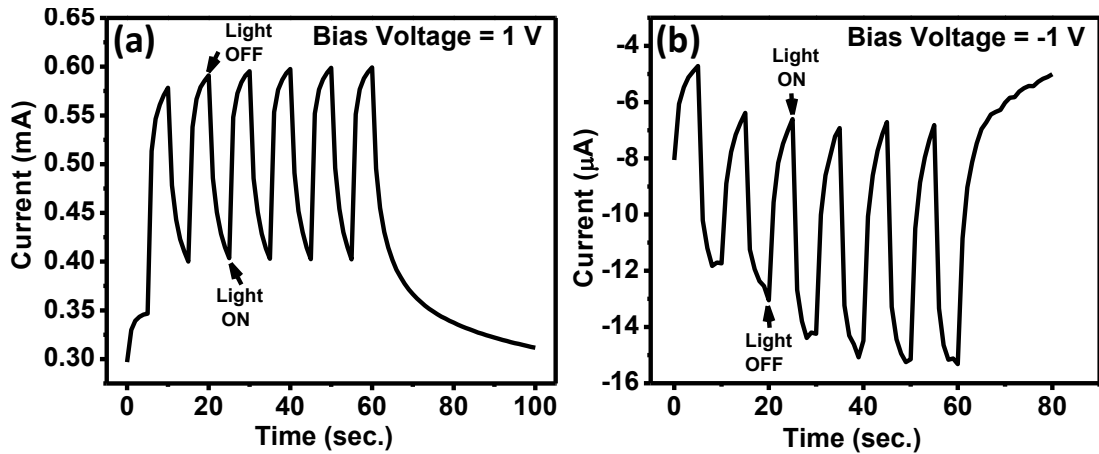


Figure 3.11: Time dependent photocurrent response of the p-n heterojunction under AM 1.5G i.e. $100\text{mW}/\text{cm}^2$ illumination at bias of (a) +1 V and (b) -1 V

The Cu₂O/ZnO nanowire flip-chip heterojunction was tested for photosensor application by taking its time dependent photo-response to solar simulator (AM 1.5G i.e. $100\text{ mW}/\text{cm}^2$ illumination) measured in air and at room temperature under forward and reverse bias of 1 V, as shown in figures 3.11 (a) and (b) respectively. In figure 3.11(a), the initial slight increase in the current without illumination can be attributed to the thermal effects (forming). This current gets stabilized after some time. Similar but reverse effect is observed in the case of reverse bias of -1 V. The % increase in photo-to-dark current is observed to be about 50% and 120% for forward and reverse bias conditions, respectively. Illumination current to dark current ratio in the case of negative bias is clearly much greater than that in the case of forward bias. This can be explained on the basis of energy band diagram. For negative bias, the majority carriers experience a large barrier. At the same time, the photo-generated minority carriers (electrons in p-Cu₂O) experience no barrier at all. For the light absorbed in the visible region, the photogenerated electrons in Cu₂O are transferred to conduction band of ZnO and are collected immediately by the positive electrode and the holes generated at the valance band of Cu₂O are collected by the negative electrode, minimizing the probability of recombination of the carriers. Thus a high ratio of photo-to-dark current is achieved. On the other hand, in the case of forward bias, the device is already in the ON state at 1.1 V. Therefore, only the extra charge carriers due to photons contribute for the increase in the current. Thus, the differential increase in the current is expected to be much higher in the reverse bias

case. It should be noted however that the increase in photo-to-dark current can be considerably higher even in the forward bias condition if the device is operated below the turn on voltage.

Further improvement in the device performance using intermediate TiO₂ or Al₂O₃ blocking layer is under investigation.

3.4 Conclusion

Cu₂O nanoneedles were synthesized by a simple anodization method followed by annealing in vacuum. A strong photo-response is realized in a simple flip-chip type rectifying junction configuration of Cu₂O nanoneedles and ZnO nanorods grown on metallic Cu and ITO, respectively, and this response is shown to be two orders of magnitude stronger than that of a thin film hetero-junction of the same materials. A ~120% resistance change was obtained under 1V reverse bias in the case of the nanowire junction.

3.5 References

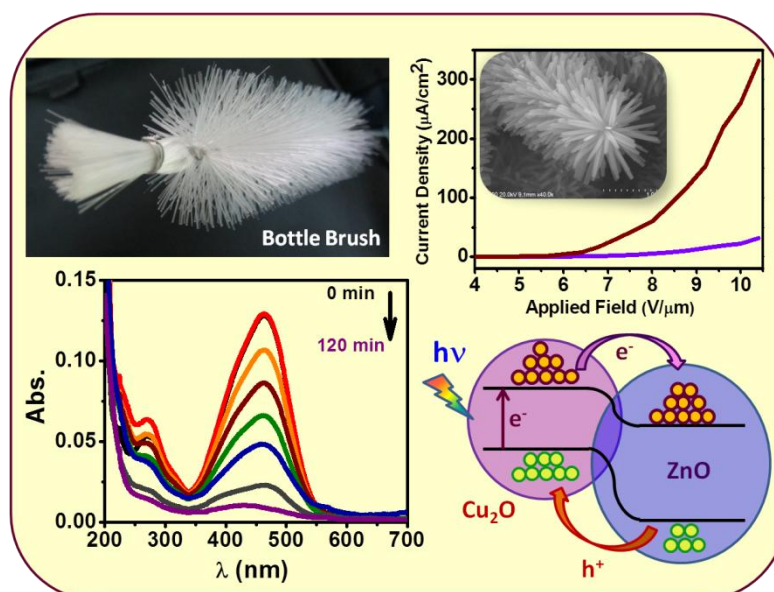
1. H. Xu, W. Wang, W. Zhu, *J. Phys. Chem. B*, **2006**, 110, 13829.
2. Y. H. Lee, I. C. Leu, C. L. Liao, S. T. Chang, M. T. Wu, J. H. Yen, K. Z. Funga, *Electrochem. Solid-State Lett.*, **2006**, 9, A207.
3. A. Mittiga, E. Salza, F. Sarto, M. Tucci, R. Vasanthi, *Appl. Phys. Lett.*, **2006**, 88, 163502.
4. P. E. de Jongh, D. Vanmaekelbergh, J. J. Kelly, *Chem. Comm.*, **1999**, 1069.
5. S. Sahoo, S. Husale, B. Colwill, T.-M. Lu, S. Nayak, P. M. Ajayan, *ACS Nano*, **2009**, 3, 3935.
6. Y. Xia, P. Yang, Y. Sun, Y. Wu, B. Mayers, B. Gates, Y. Yin, F. Kim, H. Yan, *Adv. Mater.*, **2003**, 15, 353.
7. W. Wang, G. Wang, X. Wang, Y. Zhan, Y. Liu, C. Zheng, *Adv. Mater.* **2002**, 14, 67.
8. D. P. Singh, N. R. Neti, A. S. K. Sinha, O. N. Srivastava, *J. Phys. Chem. C* **2007**, 111, 1638.
9. L. Vayssieres, *Adv. Mater.*, **2003**, 15, 464.

10. A. Yengantiwar, R. Sharma, O. Game, A. Banpurkar, *Current Applied Physics*, **2011**, 11, S113-S116
11. M. Yamashita, K. Omura, D. Hirayama, *Surface Science*, **1980**, 96, 443.
12. S. Poulston, P. M. Parlett, P. Stone and M. Bowker, *Surf. Interface Anal.*, **1996**, 24, 811.
13. S. M. Sze, “*Physics of Semiconductor Devices*”, Wiley Eastern Limited, New Delhi, 2nd Edition, **1981**, Ch.14, p. 807.
14. Y. Y. Proskuryakov, K. Durose, M. K. Al Turkestani, I. Mora-Seró, G. Garcia-Belmonte, F. Fabregat-Santiago, J. Bisquert, V. Barrioz, D. Lamb, S. J. C. Irvine, E. W. Jones, *J. Appl. Phys.*, **2009**, 106, 044507.
15. M. Adachi, M. Sakamoto, J. Jiu, Y. Ogata, S. Isoda, *J. Phys. Chem. B*, **2006**, 110, 13872
16. B. D. Yuhas, P. Yang, *J. Am. Chem. Soc.*, **2009**, 131, 3756.

Chapter 4

Cu₂O/ZnO Hetero-nanobrush: Hierarchical assembly, Field Emission and Photocatalytic Properties

Cu₂O/ZnO hetero-nanobrush assembly is formed by seed assisted growth of zinc oxide (ZnO) nanorods on cuprous oxide (Cu₂O) nanoneedles. It is observed that the turn on field and overall current density of the nanobrush improves dramatically as compared to only Cu₂O nanoneedles. Also, the charge separation and transport are facilitated because of the multiple p/n junctions formed at p-Cu₂O/n-ZnO interfaces and quasi 1D structures of both the materials, respectively. Thus, the Cu₂O/ZnO hetero-nanobrush assembly can also be used as a good photocatalyst for degradation of organic pollutants as compared to only Cu₂O nanoneedles, as it shows an excellent improvement in photocatalytic properties.



Ref.: Meenal Deo et al. *J. Mater. Chem.*, **2012**, 22, 17055

4.1 Introduction

Since the discovery of carbon nanotubes¹, quasi-1D nanostructures have become an interesting and special class of materials in view of their unique properties such as specific nature of the electronic density of states, possibility of ballistic charge transport, localization effects, increased surface area enabling surface electronic functionalization etc. These lead to many applications in the field of electronics and opto-electronics^{2, 3}. Forming a branched 3-D structure of 1-D systems enhances the application domain even further. Indeed, such branched 3-D structures have found applications in the fields of solar energy conversion⁴, field electron emission⁵⁻⁸, gas sensing⁹, and photocatalysis¹⁰. ZnO is perhaps the most studied material in this respect because it can be easily formed in interesting 3D morphologies by seeded secondary growth¹¹. Interestingly, formation of heterostructure with components having different functionalities with favourable band alignment can not only lead to a functional integration of the properties of both the materials but also to novel interface effects and phenomena¹². For example, some nanocomposites involving carbon nanostructures have shown excellent enhancement in photocatalytic activity than their components^{13, 14}. Semiconducting oxides are a special class of materials known for their broad range of electronic and optical properties and have therefore attracted scientific attention for several years. Heterostructures of such metal oxides have been of significant interest in the context of diverse applications.¹⁵ 3-D branched heterostructures in particular are now beginning to attract more attention due to major advantages of tremendously increased surface area, enhanced heterojunction density, and intrinsic light harvesting effects. Various 3-D branched heterostructures of metal oxides have been pursued for different applications: For example, ZnO-WO₃¹⁶, SnO₂-WO₃¹⁷ for field emission, SnO₂-Fe₂O₃ for photocatalysis¹⁸, In₂O₃-SnO₂ for gas sensing¹⁹, Fe₂O₃-SnO₂ for Li-ion batteries²⁰ and ternary oxides such as MnMoO₄-CoMoO₄ for supercapacitors²¹.

Cuprous oxide (Cu₂O) is one of the few p-type direct band gap metal oxide based semiconductors (Band gap ~2.17 eV). It has additional advantages of non-toxicity, low cost and abundance of its starting material i.e. copper. Cu₂O has attracted interest as a good candidate material for solar cells²², photocatalysis²³, and photo-electrochemical (PEC) water splitting²⁴ because of its favourable absorption in the

visible range. However Cu₂O is far less explored in heterostructure nanomaterial form for various applications. It is also less explored material for field electron emission studies although its work function (4.8 eV) is low. To our knowledge there are only two reports, one on thin film form²⁵ and one on nanostructured Cu₂O²⁶ for field emission. ZnO is another interesting material which has n-type conductivity with a band gap of ~3.37 eV. It has been well studied for solar cell²⁷ and field emission²⁸ applications. The major advantage of ZnO is that it can be fabricated in various morphologies which are useful in different applications. Although a few heterojunction forms of Cu₂O/ZnO have been studied for photovoltaic²⁹⁻³³ and photocatalytic³⁴⁻³⁶ applications, clearly further work on the heterostructures of Cu₂O and ZnO is needed for enhanced functionality. In this work, we report synthesis of the hetero-nanobrush comprising of Cu₂O nanoneedles decorated with ZnO nanorods by a two step chemical method. We have examined such a hetero-nanobrush system for field electron emission and photocatalysis applications.

4.2 Experimental Section

4.2.1 *Synthesis of Cu₂O/ZnO hetero-nanobrush on copper*

The Cu₂O nanoneedles film was grown directly on copper substrate employing a protocol previously reported by us³⁷. Copper foil was anodized in the presence of 2M KOH which acts as electrolyte and graphite rod as the counter electrode. This leads to evenly spread Cu(OH)₂ nanoneedles film on the Cu substrate which on annealing at 450°C in controlled oxygen pressure (5*10⁻⁶ mbar) gets converted into Cu₂O nanoneedles.

We carried out seed assisted growth of ZnO on Cu₂O, to achieve brush like ZnO morphology. Thus a seed layer of ZnO was deposited by Pulsed Laser Deposition (PLD) technique on the Cu₂O nanoneedle film. The deposition was carried out in an oxygen pressure of 1*10⁻⁴ mbar at the substrate temperature of 100°C for better adherence of the ultrathin ZnO surface nanostructure. For facile growth of ZnO on the seeded surface of Cu₂O, an equimolar (25 mM) solution of Zn(NO₃)₂ and hexamethylene tetramine (HMT) was used for the reaction. The reaction was carried out at 95°C while stirring simultaneously for only 15 minutes. The samples were then rinsed with de-ionized water and dried in air. The Cu₂O/ZnO heterostructure films

were then annealed in vacuum (5×10^{-5} mbar) at 250°C for better adherence and better crystallinity of the nanostructure. This growth procedure is schematically shown in Figure 4.1.

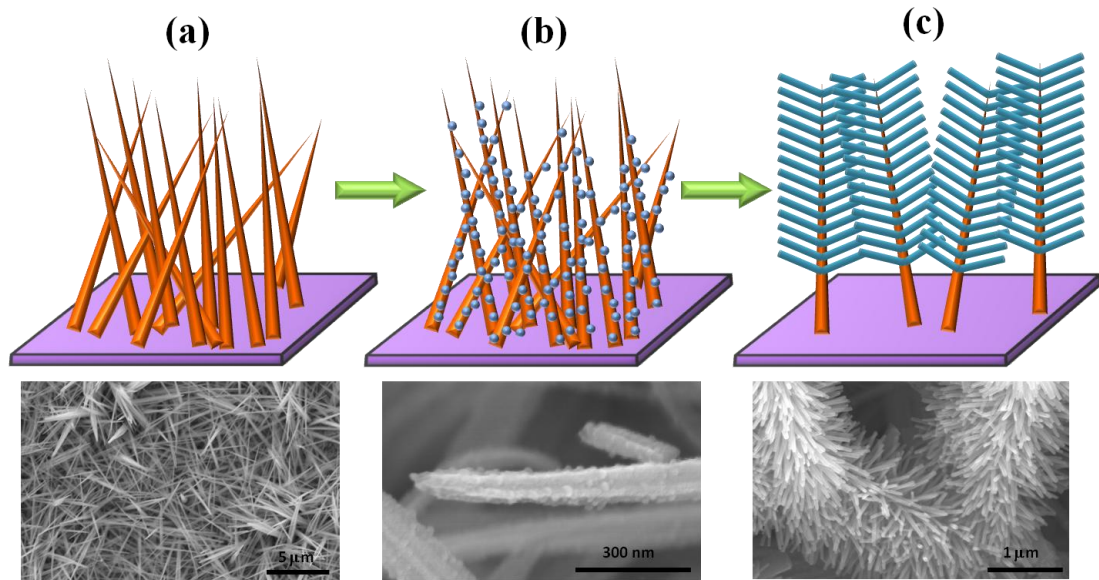


Figure 4.1: Schematic of the growth procedure of Cu₂O/ZnO hetero-nanobrush. The bottom pictures show SEM images of each growth step.

From the high resolution SEM shown in fig. 4.1 (b), there are ZnO nanoparticles formed all over the surface of the Cu₂O nanoneedles by PLD, which ensures further growth of ZnO nanorods. The ZnO nanorod growth was carried out in the presence of hexamethylene tetramine (HMT) which covers non-polar surfaces of ZnO, other than the (002) plane system, to enhance the nanorod growth in the direction of (002). Fig. 4.1 (c) gives the schematic and SEM image of the growth of ZnO nanorods on Cu₂O nanoneedles surface. These heterostructured films were further characterized by using XRD, SEM and TEM.

4.2.2 General Characterizations

Various techniques such as X-ray diffraction (XRD, Philips X'Pert PRO), Field Emission Scanning Electron Microscopy (FE-SEM, Hitachi S4800), UV-Vis spectrophotometer (Jasco V-570) were used for characterizations. The analytical transmission electron microscopy (TEM) was also performed with a probe corrected

ARM200F JEOL microscope operated at 200kV. Energy Dispersive X-ray Spectroscopy (EDS) was performed with a JEOL JED2300 detector with a probe size of 0.2 nm.

4.2.3 Field Emission and Photocatalysis experiments

The field emission (FE) current density-electric field (J-E) characteristic measurements were carried in all-metal field emission microscope with a load lock chamber. The FE studies were carried out in a planar diode configuration, wherein Cu₂O nanoneedles or Cu₂O/ZnO hetero-nanobrushes served as a cathode and a semi-transparent cathodoluminescent phosphor screen (ZnS:Cu Green Color) as an anode. The cathode was pasted onto a sample holder using vacuum compatible conducting silver paste and was held in front of the anode screen at a distance of ~500 μm. The emission current density - applied electric Field (J-E) characteristic measurements were carried out at 1×10^{-8} mbar pressure using a Keithley 6514 electrometer and a Spellman high voltage DC power supply (0-40kV). For FE, we kept the area of the specimen as 1 cm².

The Photocatalysis measurements were done at room temperature and in 10^{-5} M aqueous solution of methyl orange (MO), used as a pollutant. The Cu₂O nanoneedles and Cu₂O/ZnO heterostructure films of the same area were directly dipped into the methyl orange solution. The solution was first stirred in the dark in the presence of the film for 30 minutes before photocatalytic measurements so as to reach the adsorption/desorption equilibrium. Then it was continuously stirred under solar simulator (AM 1.5, 100 mW/cm²) used for illumination. The spectral intensity distribution was analyzed using UV-Vis spectro-photometer for specific intervals of time for a total time of 2.5 hours.

4.3 Results and Discussion

4.3.1 Characterization of Cu₂O/ZnO Heterostructure

The morphology of the as-synthesized Cu₂O/ZnO heterostructure was imaged by Field Emission Scanning Electron Microscopy (FESEM). Figure 4.2 (a) shows low magnification SEM image which reveals a uniform formation of brush like structures. From the high magnification SEM images, shown in inset of fig. 4.2 (a), it

is seen that ZnO nanorods have been decorated all over the Cu₂O nanoneedle surface forming the hetero-nanobrush morphology. It is also seen that the length of single ZnO nanorod is around 500 nm with hexagonal cross section having a diameter about 50 nm.

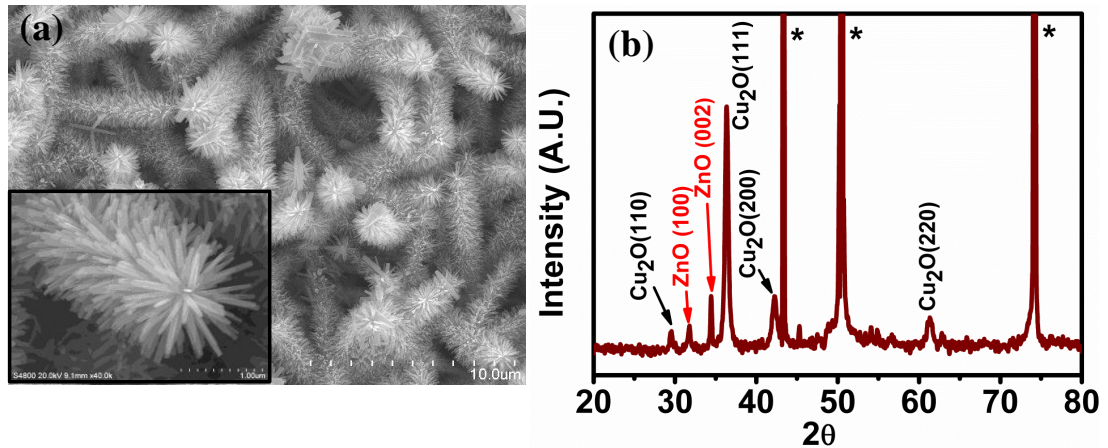


Figure 4.2: (a) Low magnification FESEM image of Cu₂O/ZnO hetero-nanobrush, inset shows High magnification FESEM image, (b) X-Ray Diffraction pattern of Cu₂O/ZnO hetero-nanobrush. * represents copper substrate peaks

Figure 4.2 (b) shows the X-Ray Diffraction (XRD) pattern of Cu₂O/ZnO hetero-nanobrush. The XRD shows polycrystalline phase of Cu₂O nanoneedles grown directly on copper. The formation of ZnO phase is also confirmed by XRD. During the deposition of ZnO nanorods on these Cu₂O nanoneedles, even if the deposition is carried out at 95°C in air, the Cu₂O phase does not get converted into CuO. This can be attributed to uniform growth and surface coverage of ZnO seed layer by PLD, which also acts as protecting layer for Cu₂O avoiding its further oxidation.

To reveal the precise morphology and the interconnection of the two phases detected by XRD (namely Cu₂O and ZnO) some TEM observations were carried out. As shown in Fig. 4.3 (a), the structure of hetero-nanobrushes consists of a core nanoneedle covered by nanorods that are seen to nucleate and grow on its surface. EDS elemental mapping (Fig. 4.3 (b), (d) and (e)), clearly brings out the copper rich core and the Zn rich shell. SAED patterns recorded on the nanoneedle (Fig. 4.3 (c)) and on nanorod (Fig. 4.3 (f)) confirm that the two pure phases present are Cu₂O and ZnO, respectively, in agreement with the XRD data. The typical diameter of ZnO

nanorods measured from TEM images is in a range of 30 to 50 nm, while the mean diameter of Cu₂O nanoneedles is about 100 nm. Using EDS analysis, the composition of both oxides was qualitatively estimated. A Zn:O (Cu:O) ratio of 0.96 (1.94) was found for the ZnO (Cu₂O), in good agreement with the expected stoichiometry.

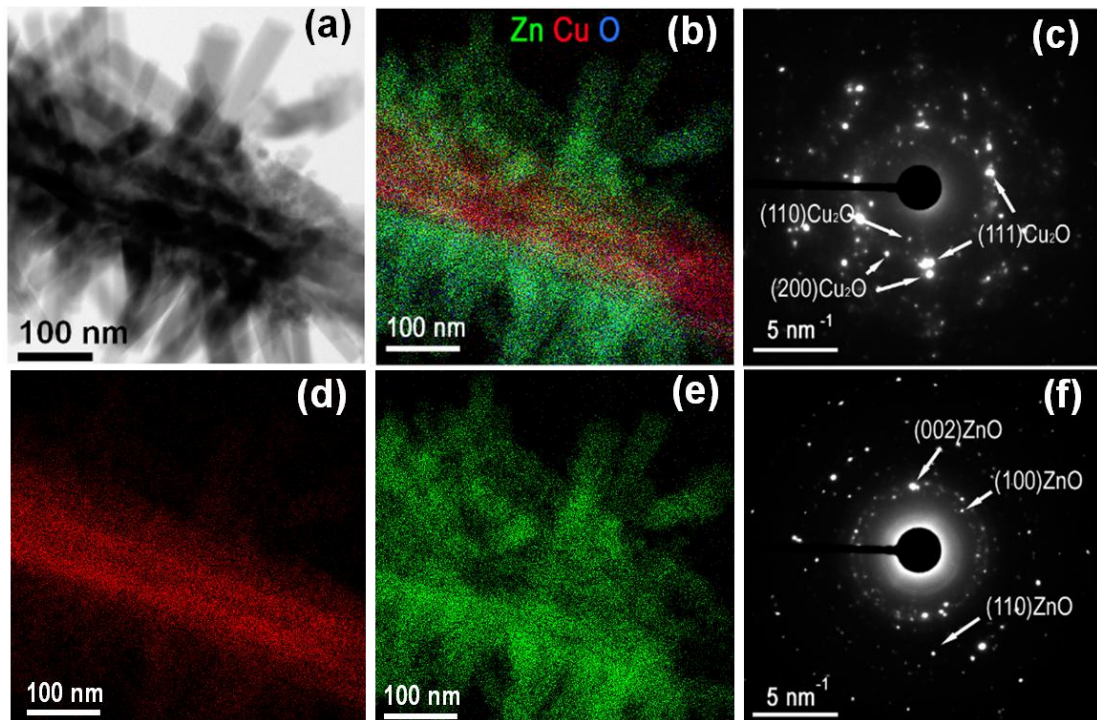


Figure 4.3: (a) Bright field STEM image of a Cu₂O/ZnO hetero-nanobrush and (b) corresponding EDS elemental mapping showing the distribution of Zn (green), Cu (red) and O (blue) within the structure, and separate elemental mapping of (d) Cu and (e) Zn, SAED pattern obtained with a small probe located on the (c) cuprous oxide nano-needle and (f) on the Zinc oxide nanorods, confirming that only two phases are present, namely Cu₂O and ZnO.

We have performed HRTEM analysis of Cu₂O nanoneedle and ZnO nanorods grown on Cu₂O nanoneedles to find exact crystal growth directions of both Cu₂O and ZnO, as shown in fig. 4.4 (a) and (b), respectively. We find that Cu₂O nanoneedle grows along [220] direction, while the ZnO nanorods grow along the [002] direction. As the growth direction of hexagonal ZnO nanorods is along [002], the six surface facets of ZnO nanorods are along the (101 $\bar{0}$) family of planes which are

perpendicular to the [002] direction. The Cu₂O surface facets, which are found from HRTEM analysis, are mostly along (111) planes.

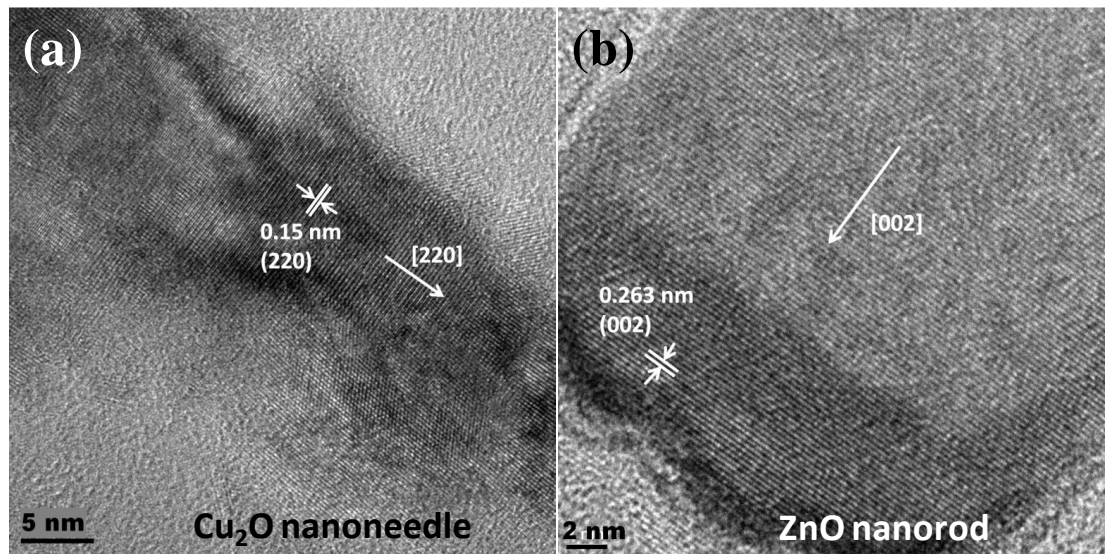


Figure 4.4: HRTEM images of (a) Cu₂O nanoneedle and (b) ZnO nanorod.

4.3.2 Field Emission studies

The field emission properties of Cu₂O are rarely studied, in contrast to the other semiconducting oxides such as ZnO, SnO₂, WO₃, etc. Moreover the possibility of the enhancement in its field emission properties by making its composites with other materials has not been explored yet. We have therefore studied the field emission properties of Cu₂O nanoneedles and also Cu₂O/ZnO hetero-nanobrushes.

Figure 4.5 (a) depicts the field emission current density as a function of the applied electric field (J-E) plot. The turn-on field and threshold field, defined as the field required to draw an emission current density of $\sim 10 \mu\text{A}/\text{cm}^2$ and $\sim 100 \mu\text{A}/\text{cm}^2$, are found to be $\sim 8.4 \text{ V}/\mu\text{m}$ and $\sim 11.8 \text{ V}/\mu\text{m}$, respectively, for Cu₂O nanoneedles, and $\sim 6.5 \text{ V}/\mu\text{m}$ and $\sim 8.9 \text{ V}/\mu\text{m}$, respectively, for the Cu₂O/ZnO nanobrush sample. Relatively the lower turn on field for the Cu₂O/ZnO heterostructure can be attributed to its unique geometrical form (which controls the field distribution) along with favourable band structure. As reported by Ujjal Gautam et. al.³⁸, in the case of such branched structures, the applied primary field gets enhanced at the stems (Cu₂O nanoneedles in our case) which successively acts as secondary field for the branches (ZnO nanorods in our case), thereby enhancing the local electric field.

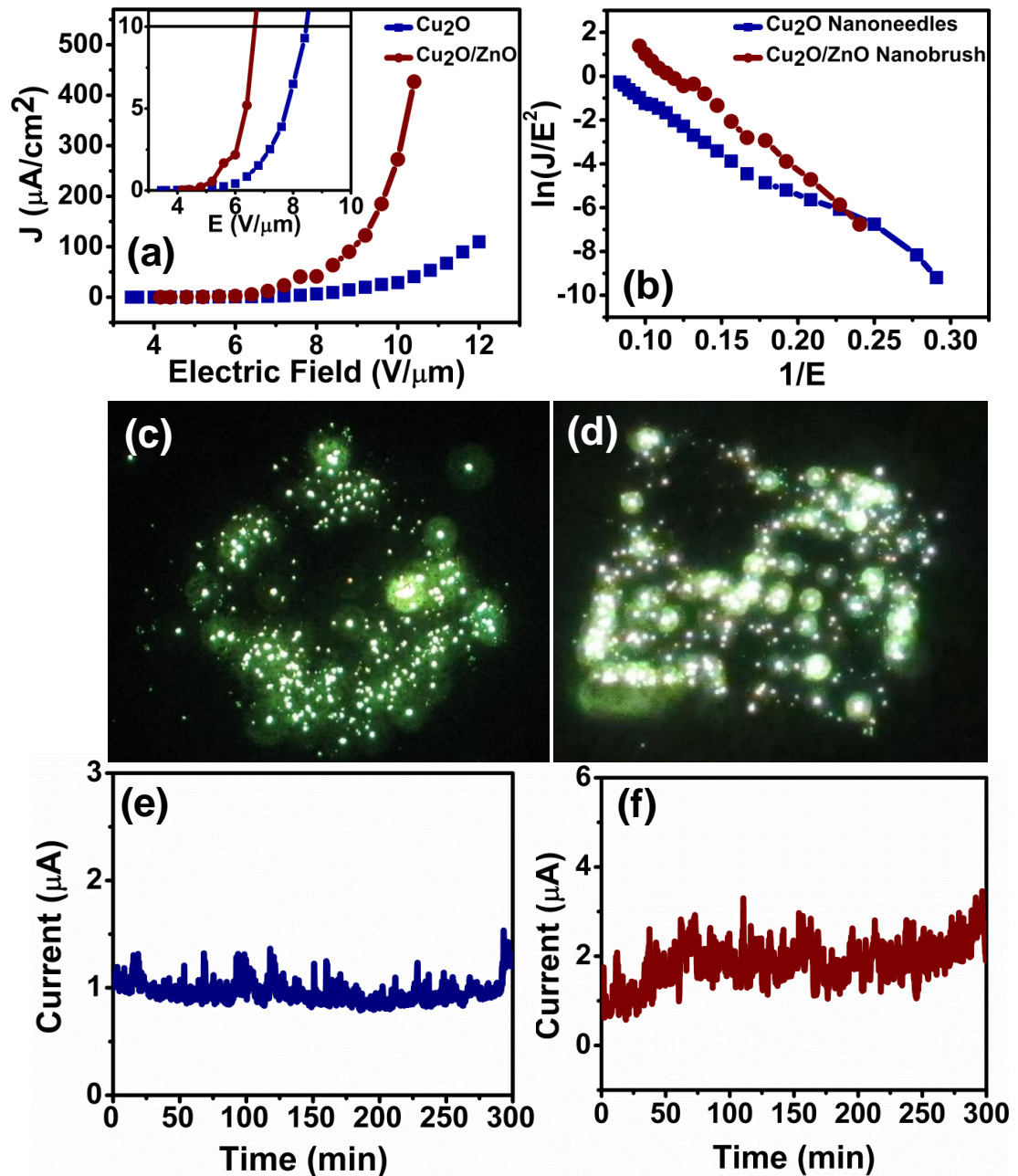


Figure 4.5: (a) Field emission current density - applied electric field (J-E) characteristics (Inset shows turn-on value), (b) Corresponding Fowler-Nordheim (F-N) plot of Cu₂O nanoneedles and Cu₂O/ZnO nanobrush, (c) and (d) show the field emission micrographs of Cu₂O nanoneedles and Cu₂O/ZnO nanobrush, respectively. The traces in (e) and (f) show the current stability for Cu₂O nanoneedles and Cu₂O/ZnO nanobrush, respectively.

Interestingly, the current density in the case of the Cu₂O/ZnO nanobrush is seen to have increased dramatically to $\sim 425 \mu\text{A}/\text{cm}^2$ in comparison to $\sim 40 \mu\text{A}/\text{cm}^2$ in the case of Cu₂O nanoneedles at an applied electric field of $\sim 10.5 \text{ V}/\mu\text{m}$. This tremendous increase in the current density can be attributed to the branched structure which acts as multiple emitters. As reflected from the basics of field emission, the emission current density is mainly decided by the intrinsic property (work function) and the extrinsic property (shape and size) of the emitter material. Thus for a better field emission performance the material with low work function should be in quasi 1D form and preferably oriented perpendicular to the substrate i.e. vertically aligned. As seen from the SEM image (fig. 4.1 (a)), the random orientation of the Cu₂O nanoneedles is also responsible for their inferior FE characteristics as compared to Cu₂O/ZnO hetero-nanobrushes. On the other hand, in case of Cu₂O/ZnO nanobrush (Fig. 4.2 (a)) there are relatively fair number of emitters pointing towards the anode; thus the effective electric field experienced by an individual ZnO nanorod will be more as compared to only Cu₂O nanoneedle and hence enhancement in the field emission current is observed.

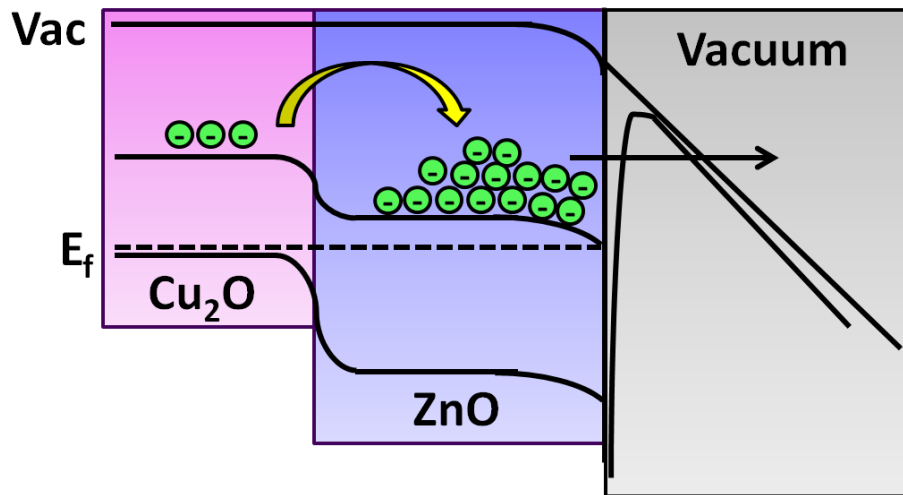


Figure 4.6: Band diagram of Cu₂O/ZnO heterojunction

This phenomenon can be further discussed on the basis of the band diagram of Cu₂O/ZnO heterostructure schematically shown in fig. 4.6. Normally in the case of the field emission from heterostructures, it is well accepted that the work function of the shell material should be lower than that of the core material. Considering the work functions of Cu₂O and ZnO of about 4.8 eV and 5.3 eV, respectively, one could

expect higher value of the turn-on field in the case of Cu₂O/ZnO nanobrush than that of only Cu₂O nanoneedles. But, when these two materials come into contact, there is a formation of p-n junction at their interface and there is a favourable band alignment for the electron transport from the conduction band of core Cu₂O to the conduction band of shell ZnO, as shown in fig. 4.6.

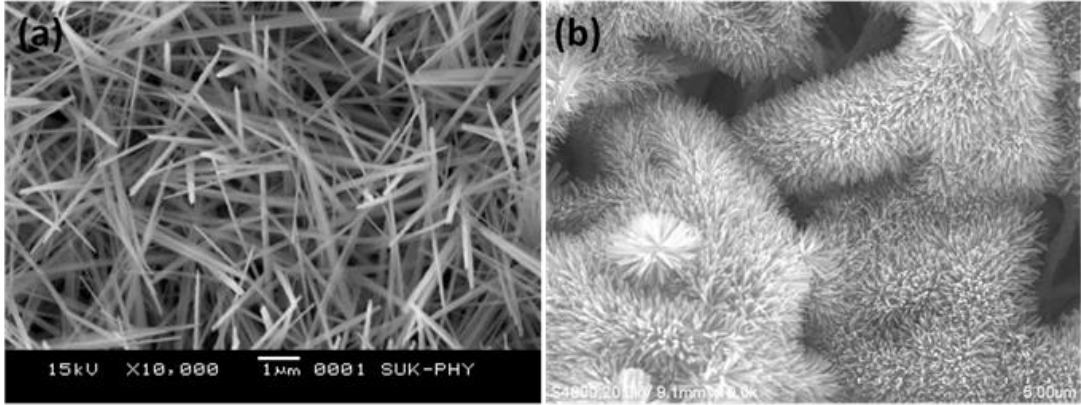


Figure 4.7: SEM images of (a) Cu₂O nanoneedles and (b) Cu₂O/ZnO nanobrush

In any practical measurement, the turn-on field is defined as the field at which the emission current attains a specific chosen value. It is taken as 10 $\mu\text{A}/\text{cm}^2$ in our case, as in many other works. This value then also depends on the number of emission points (tips) per cm^2 in addition to the value of the work function. In the present case since a number of ZnO brush-like strands grow on each Cu₂O tip, the density of emission points is considerably higher in the case of ZnO/Cu₂O hetero-brush, as clear from SEM images shown in fig. 4.7 (a) and (b). Hence in spite of the higher work function of ZnO, the current density of 10 $\mu\text{A}/\text{cm}^2$ is reached at a lower applied field. Thus the effective turn on field is lower.

The field emission characteristics were further analysed by Fowler-Nordheim equation³⁹, which is given by,

$$J = \left(\frac{A\beta^2 E^2}{\phi} \right) \exp\left(-\frac{B\phi^{3/2}}{\beta E} \right)$$

Where, $A=1.54 \times 10^{-6} \text{ A eV V}^{-2}$ and $B= 6.83 \times 10^3 \text{ eV}^{-3/2} \text{ V } \mu\text{m}^{-1}$, J is the current density, E is the applied electric field, ϕ is the work function of emitting material and β is field enhancement factor.

The Fowler-Nordheim (F-N) plot derived from the observed J-E characteristic is shown in fig. 4.5 (b). The F-N plot shows an overall linear behaviour with decrease in the slope (non-linearity) at very high applied field range. Such type of F-N plot exhibiting tendency toward nonlinearity at very high applied field has been also reported in our previous work¹⁷.

The field emission micrographs corresponding to Cu₂O nanoneedles and Cu₂O/ZnO nanobrush emitters are shown in Fig. 4.5 (c) and (d) respectively. The number of spots for the Cu₂O/ZnO nanobrush is larger because of the increased density of the emission sites as compared to Cu₂O nanoneedles. More non-uniformity of the emission spots in case Cu₂O also suggests that all the needles cannot take part in the emission at lower applied fields.

For field emission electron sources, along with the emission competence, the current stability is also a decisive and important parameter. The current stability curve (I-t plot) recorded for Cu₂O nanoneedles is shown in fig. 4.5 (e) which shows that the emission current is quite steady, whereas an instability in the emission current is seen for Cu₂O/ZnO nanobrush (fig. 4.5 (f)). This can be attributed to the adsorption / desorption of residual gas molecules present in the ambient of the specimen. The instability in emission current in Cu₂O/ZnO nanobrush can be attributed to the densely crowded ZnO branches which cause more surface area for the adsorption and diffusion of residual gas molecules on the emitter surface. Other considerations such as field migration of oxygen vacancies, mild ion bombardment etc. may also be operative.

4.3.3 *Photocatalysis*

In view of the favourable band alignment of Cu₂O and ZnO for efficient separation of charges, we studied the photocatalytic activity of Cu₂O nanoneedles and Cu₂O/ZnO hetero-nanobrush for degradation of Methyl Orange (MO) dye in the presence of simulated sunlight as shown in figures 4.8 (a) and (b) respectively.

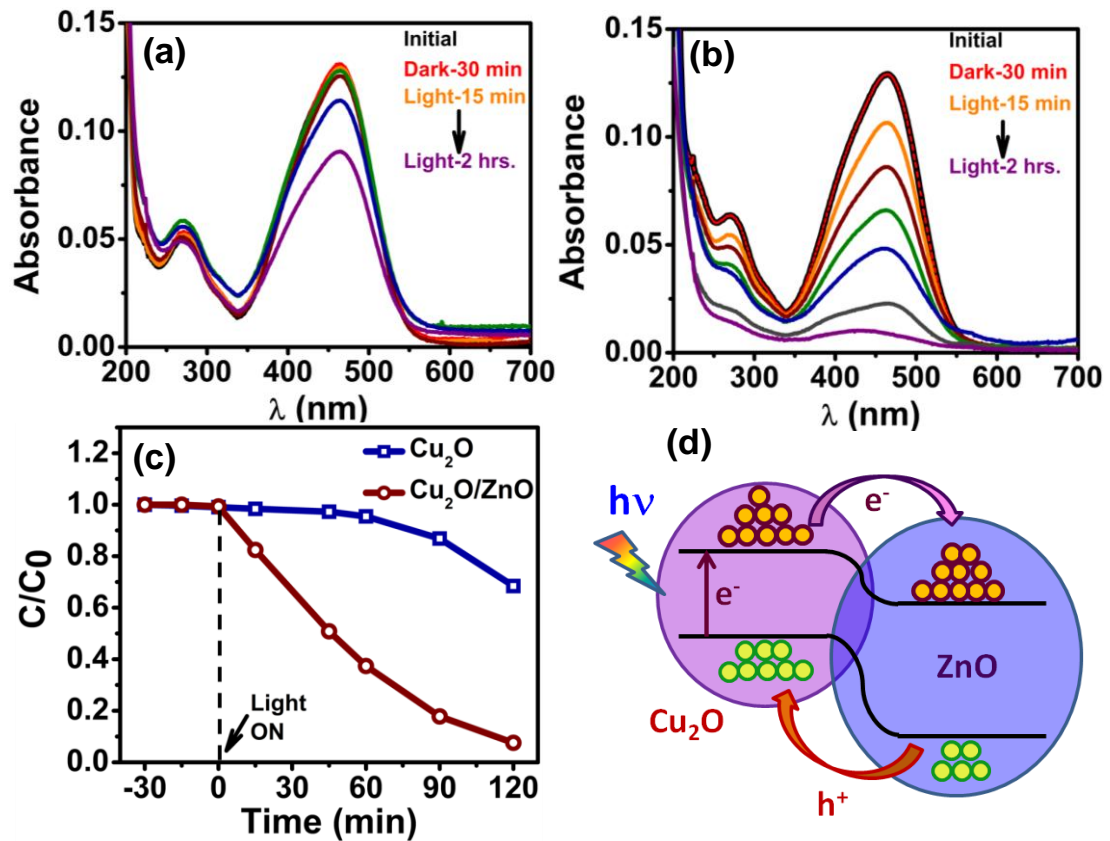
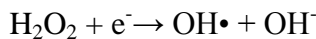
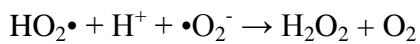
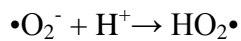
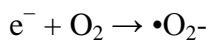
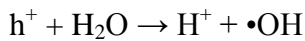


Figure 4.8: UV-Vis absorption spectroscopy of Methyl orange dye taken at different times under visible light in the presence of (a) Cu₂O nanoneedles and (b) Cu₂O/ZnO nanobrush (c) Rates of corresponding Methyl Orange degradation (d) Schematic diagram showing charge generation and transfer in the presence light causing degradation of dye.

The Cu₂O nanoneedles film and Cu₂O/ZnO nanobrush film were treated in the dark for 30 minutes before the photocatalytic measurements (light on) to eliminate the possibility that higher adsorption site density in the case of the Cu₂O/ZnO nanobrush did not simply adsorb more dye molecules and hence showed an “apparent” rapid dye removal from the solution that is examined optically. It can be clearly seen from figures 4.8 (a) and (b) that there is hardly any change in the intensity of MO after 30 minutes treatment in the dark. Also, from fig. 4.8 (a) and (b) we can notice that the Cu₂O/ZnO nanobrush system can degrade the dye almost completely in 120 minutes under illumination, which is not possible with the Cu₂O nanoneedles alone. By considering the intensity of measure peak of methyl orange at 464 nm, we have plotted the corresponding rates of degradation by Cu₂O and

Cu₂O/ZnO as shown in fig. 4.8 (c), which indicates that, the rate in the presence of Cu₂O/ZnO is much faster than only Cu₂O. According to this data, after 2 hours in the presence of light, the amount of MO remaining in the case of Cu₂O nanoneedles is around 70% while that in the case of Cu₂O/ZnO nanobrush is only around 7%.

There can be two possible reasons for this fast photocatalysis in the case of Cu₂O/ZnO. Because of the special brush-like morphology, the surface area in the case of Cu₂O/ZnO nanobrush is much greater than that of Cu₂O nanoneedles which is highly advantageous for good photocatalytic activity⁴⁰. Also, the Cu₂O is p-type having band gap of 2.1 eV, which absorbs visible light, but there is a possibility of recombination in the case of only Cu₂O. When we make Cu₂O/ZnO heterostructure there is a favourable p-n junction formation which helps in the separation of generated electron-hole pairs in the presence of light and avoids recombination. This is shown schematically in fig. 4.8 (d). Also, because of the quasi 1D nature of both Cu₂O and ZnO, the generated charges can very quickly come at the surface, which contributes to the degradation of dye. After the separation of electrons and holes, there are some reactions involved for the formation of OH• radicals, which can be written as⁴¹:



These hydroxyl radicals are known to be very reactive oxidative species which react with the organic or water pollutants and degrade them.

4.4 Conclusion

We have synthesized Cu₂O/ZnO hetero-nanobrush on copper substrate by simple chemical route. The Cu₂O/ZnO hetero-nanobrush leads to the formation of multiple p-n junctions, and enhancement of the surface area and tip density. These properties are utilized in the applications of field electron emission and photocatalysis. We observe that for the Cu₂O/ZnO nanobrush case the field emission current increases

and turn-on field decreases significantly in comparison to the case of Cu₂O nanoneedles. The Cu₂O/ZnO nanobrush structure is also shown to be a good candidate for photocatalysis as it degrades methyl orange effectively than only Cu₂O nanoneedles.

4.5 References

1. Sumio Iijima, *Nature*, **1991**, 354, 56-58.
2. Jia Grace Lu, Paichun Chang, Zhiyong Fan, *Mat. Sci. Eng. R*, **2006**, 52, 49–91.
3. Tianyou Zhai, Liang Li, Ying Ma, Meiyong Liao, Xi Wang, Xiaosheng Fang, Jiannian Yao, Yoshio Bando and Dmitri Golberg, *Chem. Soc. Rev.*, **2011**, 40, 2986–3004.
4. Matthew J. Bierman, Song Jin, *Energy Environ. Sci.*, **2009**, 2, 1050–1059
5. Zhiqiang Wang, Jiangfeng Gong, Yun Su, Yuwen Jiang, Shaoguang Yang, *Cryst Growth Des*, **2010**, 10, 2455–2459
6. Chuanbao Cao, Zhuo Chen, Xiaoqiang An, Hesun Zhu, *J. Phys. Chem. C*, **2008**, 112, 95-98.
7. Zhi-Gang Chen, Lina Cheng, Hong-Yi Xu, Ji-Zi Liu, Jin Zou, Takashi Sekiguchi, Gao Qing (Max) Lu, Hui-Ming Cheng, *Adv. Mater.*, **2010**, 22, 2376–2380.
8. Guohua Li, Tianyou Zhai, Yang Jiang, Yoshio Bando, Dmitri Golberg, *J. Phys. Chem. C*, **2011**, 115, 9740–9745.
9. N. Zhang, Ke Yu, Q. Li, Z. Q. Zhu, Q. Wan, *J. Appl. Phys.*, **2008**, 103, 104305.
10. Caihong Fang, Baoyou Geng, Jun Liu and Fangming Zhan, *Chem. Commun.*, **2009**, 2350–2352.
11. Seung Hwan Ko, Daeho Lee, Hyun Wook Kang, Koo Hyun Nam, Joon Yeob Yeo, Suk Joon Hong, Costas P. Grigoropoulos, and Hyung Jin Sung, *Nano Lett.*, **2011**, 11, 666–671.
12. Delia J. Milliron, Steven M. Hughes, Yi Cui, Liberato Manna, Jingbo Li, Lin-Wang Wang, A. Paul Alivisatos, *Nature*, **2004**, 430, 190-195.
13. Jiang Du, Xiaoyong Lai, Nailiang Yang, Jin Zhai, David Kisailus, Fabing Su, Dan Wang, and Lei Jiang, *ACS Nano*, **2011**, 5, 590–596.

14. Shuo Wang, Luoxin Yi, Jonathan E. Halpert, Xiaoyong Lai, Yuanyuan Liu, Hongbin Cao, Ranbo Yu, Dan Wang, and Yuliang Li, *Small*, **2012**, 8, 265-271.
15. Junqing Hu, Yoshio Bando and Dmitri Golberg, *J. Mater. Chem.*, **2009**, 19, 330–343.
16. Heejin Kim, Seongho Jeon, Mikyung Lee, Junghan Lee and Kijung Yong, *J. Mater. Chem.*, **2011**, 21, 13458–13463.
17. Deodatta R. Shinde, Padmakar G. Chavan, Shashwati Sen, Dilip S. Joag, Mahendra A. More, S. C. Gadkari, and S. K. Gupta, *ACS Appl. Mater. Interfaces*, **2011**, 3, 4730–4735.
18. Mutong Niu, Feng Huang, Lifeng Cui, Ping Huang, Yunlong Yu, and Yuansheng Wang, *ACS Nano*, **2010**, 4, 681–688.
19. Yung-Chiun Her, Ching-Kuo Chiang, Sen-Tsun Jean and Sing-Lin Huang, *Cryst. Eng. Comm.*, **2012**, 14, 1296–1300.
20. Weiwei Zhou, Chuanwei Cheng, Jinping Liu, Yee Yan Tay, Jian Jiang, Xingtao Jia, Jixuan Zhang, Hao Gong, Huey Hoon Hng, Ting Yu, Hong Jin Fan, *Adv. Funct. Mater.*, **2011**, 21, 2439–2445.
21. Li-Qiang Mai, Fan Yang, Yun-Long Zhao, Xu Xu, Lin Xu & Yan-Zhu Luo, *Nat. Commun.*, **2011**, 2, 381.
22. B. P. Rai, *Solar Cells*, **1988**, 25, 265 - 272
23. Ying Zhang, Bin Deng, Tierui Zhang, Daming Gao, An-Wu Xu, *J. Phys. Chem. C*, **2010**, 114, 5073–5079.
24. Adriana Paracchino, Vincent Laporte, Kevin Sivula, Michael Grätzel and Elijah Thimsen, *Nat. Mater.*, **2011**, 10, 456–461.
25. Qun Tang, Ting Li, Xihong Chen, Dapeng Yu, Yitai Qian, *Solid State Commun.*, **2005**, 134, 229–231.
26. Hui Shi, Ke Yu, Fang Sun and Ziqiang Zhu, *Cryst. Eng. Comm.*, **2012**, 14, 278.
27. Qifeng Zhang, Christopher S. Dandeneau, Xiaoyuan Zhou, and Guozhong Cao, *Adv. Mater.*, **2009**, 21, 4087–4108.
28. Guozhen Shen, Yoshio Bando, Baodan Liu, Dmitri Golberg, and Cheol-Jin Lee, *Adv. Funct. Mater.*, **2006**, 16, 410–416.

29. Benjamin D. Yuhas and Peidong Yang, *J. Am. Chem. Soc.*, **2009**, 131, 3756–3761.
30. Jingbiao Cui, Ursula J. Gibson, *J. Phys. Chem. C*, **2010**, 114, 6408–6412.
31. Haoming Wei, Haibo Gong, Yingzi Wang, Xilun Hu, Ling Chen, Hongyan Xu, Peng Liu and Bingqiang Cao, *Cryst. Eng. Comm.*, **2011**, 13, 6065-6070.
32. Kevin P. Musselman, Andrew Marin, Andreas Wisnet, Christina Scheu, Judith L. MacManus-Driscoll, and Lukas Schmidt-Mende, *Adv. Funct. Mater.*, **2011**, 21, 573–582.
33. Ting-Jen Hsueh, Cheng-Liang Hsu, Shoou-Jinn Chang, Pei-Wen Guo, Jang-Hsing Hsieh and I-Cherng Chen, *Scripta Mater.*, **2007**, 57, 53–56.
34. Chao Xu, Lixin Cao, Ge Su, Wei Liu, Hui Liu, Yaqin Yu, Xiaofei Qu, *J. Hazard. Mater.*, **2010**, 176, 807–813.
35. Yao Wang, Guangwei She, Haitao Xu, Yunyu Liu, Lixuan Mu, Wensheng Shi, *Mater. Lett.*, **2012**, 67, 110–112.
36. Qingwei Zhu, Yihe Zhang, Fengshan Zhou, Fengzhu Lv, Zhengfang Ye, Feidi Fan, Paul K. Chu, *Chem. Eng. J.*, **2011**, 171, 61–68.
37. Meenal Deo, Sarfraj Mujawar, Onkar Game, Ashish Yengantiwar, Arun Banpurkar, Sneha Kulkarni, Jyoti Jog and Satishchandra Ogale, *Nanoscale* **2011**, 3, 4706.
38. Ujjal K. Gautam, Xiaosheng Fang, Yoshio Bando, Jinhua Zhan, Dmitri Golberg, *ACS Nano*, **2008**, 5, 1015-1021
39. Xiaosheng Fang, Yoshio Bando, Ujjal K. Gautam, Changhui Ye, Dmitri Golberg, *J. Mater. Chem.*, **2008**, 18, 509–522.
40. Fang Lu, Weiping Cai and Yugang Zhang, *Adv. Funct. Mater.*, **2008**, 18, 1047–1056.
41. Ken-ichi Okamoto, Yasunori Yamamoto, Hiroki Tanaka, Masashi Tanaka and Akira Itaya, *Bull. Chem. Soc. Jpn.*, **1985**, 58, 2015-2022.

Chapter 5

Evaluation of cuprous oxide nanoneedle photocathode for photo-electrochemical activity

Controlled synthesis of single crystalline cuprous oxide (Cu_2O) nanoneedles with {111} exposed facets is achieved on copper foil and the same film is used as photocathode for photo-electrochemical water splitting. It shows excellent performance as reflected by the current density of $\sim 1.7 \text{ mA/cm}^2$ photocurrent at 0V vs. RHE in 0.05 M Na_2SO_4 having pH ~ 6.5 . This performance shows $\sim 40\%$ stability upto 1 hr of exposure to light. We attribute this photocurrent and stability performance to the exposed (111) facets. The Cu_2O nanoneedles are further covered by TiO_2 with simple wet chemical route, which form p-n junction, leading to effective separation of charges at the interface and enhancement of the photocurrent.

5.1 Introduction

The production of hydrogen by solar energy conversion combined with water electrolysis (i.e. water splitting by photo-electrochemical (PEC) cell using semiconducting material) has attracted the attention of researchers due to the need of renewable fuels ^[1-3]. The semiconducting material used for PEC must be earth abundant, low cost and should absorb the visible light with suitable band edge positions so as to reduce / oxidize water.^[3, 4] Amongst metal oxides, p-type Cu₂O can be considered as a potentially useful material in this context, with direct band gap ~2.2 eV and favorable band positions for water splitting. For Cu₂O the conduction band is located 0.7 V negative to the hydrogen evolution potential and the valence band is just positive of the oxygen evolution potential ^[5].

Cu₂O was explored long back for photocatalytic water splitting ^[6] because of its favorable band alignment with respect to the water oxidation and reduction levels. Some researchers suggested that this may in fact be a better system for water splitting by photo-electrochemical route ^[7]. However Cu₂O is known to be unstable due to photo-corrosion in aqueous medium during illumination ^[8], and this concern has remained unanswered for many years. Recently, Gratzel group reported enhancement in the PEC performance as well as high stability by depositing protective layers of Al:ZnO and TiO₂ on Cu₂O by atomic layer deposition (ALD) ^[9]. This report boosted the attention again towards Cu₂O as a potentially viable photocathode for PEC application. Researchers are now focusing on protecting the surface of Cu₂O, which undergoes reduction reaction on exposure of light under the applied bias, affecting the PEC performance. Some efforts have been undertaken to make the Cu₂O film stable in the PEC cell by depositing different coatings such as CuO ^[10], NiO_x ^[11], and carbon ^[12] on the surface of Cu₂O.

It is a well known fact that, the catalytic or electrochemical properties of semiconducting materials vary depending on which crystal face has been exposed at the interface, because of the different atomic arrangement of each crystal face(s) ^[13, 14] and the corresponding surface electronic structure. In the photocatalytic context of Cu₂O, the (111) facet is considered as most stable ^[15]. A systematic study by Sowers et. al. on the crystal face dependent stability of Cu₂O as photocathode showed that the (111) surface, which is Cu⁺ - terminated, is the most stable for PEC ^[16]. However,

hardly any efforts have been undertaken towards the development of stable Cu₂O nanostructures with specific surface facets ^[17].

For the photocatalytic and photo-electrochemical reactions, surface area of the active material is a crucial factor. Although, in this context some nanostructured Cu₂O materials have been studied as effective photocathode ^[17 - 22], they show low photocurrent in the range of few hundreds of $\mu\text{A}/\text{cm}^2$ due to various reasons. Amongst the various nanostructures, quasi 1D nanostructures seem to be promising because they possess high surface area and provide a direct pathway for electronic charge transport. Also, in the case of planer films the photocurrent collection is limited by the high absorption depth near band gap, which is much larger ($\sim 10 \mu\text{m}$) than the minority carrier diffusion length ($\sim 10\text{-}100 \text{ nm}$) ^[23]. Therefore, high aspect ratio Cu₂O is advisable, which can effectively solve the problem of light absorption and charge separation, for its use in PEC ^[9, 12].

In this work, we have grown single crystalline Cu₂O nanoneedles with (111) facets exposed at the surface on a copper foil. The PEC performance of this film is tested and analyzed systematically. We have further coated n-type TiO₂ on the p-type Cu₂O using a simple TiCl₄ treatment ^[24] to form a p-n junction system for effective charge separation at the Cu₂O/TiO₂ interface, rendering possibility of further enhancement of the photocurrent.

5.2 Experimental

5.2.1 Synthesis

The Cu₂O nano-needle films were grown directly on copper substrate by anodization of copper itself. By anodization of copper in basic solution, we obtained Cu(OH)₂ nanoneedles film on copper, as reported earlier ^[25]. It was followed by annealing at 700°C in vacuum (5×10^{-6} mbar pressure) to get Cu₂O nanoneedles film on copper substrate. This Cu₂O film was characterized by SEM, XRD, TEM and DRS.

5.2.2 *Characterization*

X-Ray diffraction (XRD) data were recorded on a Philips X'Pert PRO using Cu K α radiation. Scanning Electron Microscopy (SEM, FEI Quanta 200 3D) was used to record the morphology of the film. High-resolution transmission electron micrographs of the samples were recorded with HR-TEM, FEI Tecnai 300. UV-visible diffused reflectance spectra (DRS) were recorded using a Jasco V-570 spectrophotometer.

5.2.3 *TiCl₄ treatment*

For conformal coating of TiO₂ on Cu₂O, we used aqueous 5 mM TiCl₄ solution prepared in ice. The films of Cu₂O were dipped in the solution for 5 and 10 seconds, while maintaining the temperature of the solution at 70°C in oil bath. The films were washed thoroughly with MilliQ water and absolute ethanol after dip coating. They were then dried at room temperature and annealed in vacuum at 200°C for the formation of TiO₂.

5.2.4 *Photoelectrochemical measurements*

An Autolab PGSTAT30 (Eco-Chemie) was used for photoelectrochemical measurements, which were performed in a three neck quartz photo-reactor with a planer window. The photoelectrochemical cell was prepared using Cu₂O film on copper as the working electrode, platinum foil as the counter electrode, and Ag/AgCl as the reference electrode. In our optimized experiment, we used 0.05 M sodium sulphate (Na₂SO₄) as electrolyte and the voltage was applied in Linear Sweep Voltammogram (LSV) mode at a scan rate of 5 mV/s. The PEC cell was illuminated using solar simulator, AM 1.5G, at incident power density of 100 mW/cm².

5.3 **Results and discussion**

5.3.1 *Characterization of Cu₂O nanoneedles*

The morphology of the as-synthesized Cu₂O film was imaged by Scanning Electron Microscopy (SEM). Figure 5.1 (a) shows the SEM image from which it is clearly observed that the whole surface of the film is comprised of dense uniform elongated structures. These nanowire-type structures were further characterized by TEM, as shown in the inset of figure 5.1 (a). The corresponding TEM of single

nanowire shows tapering needle-like morphology. This also shows that the needle is very long $\sim 5 \mu\text{m}$ in length.

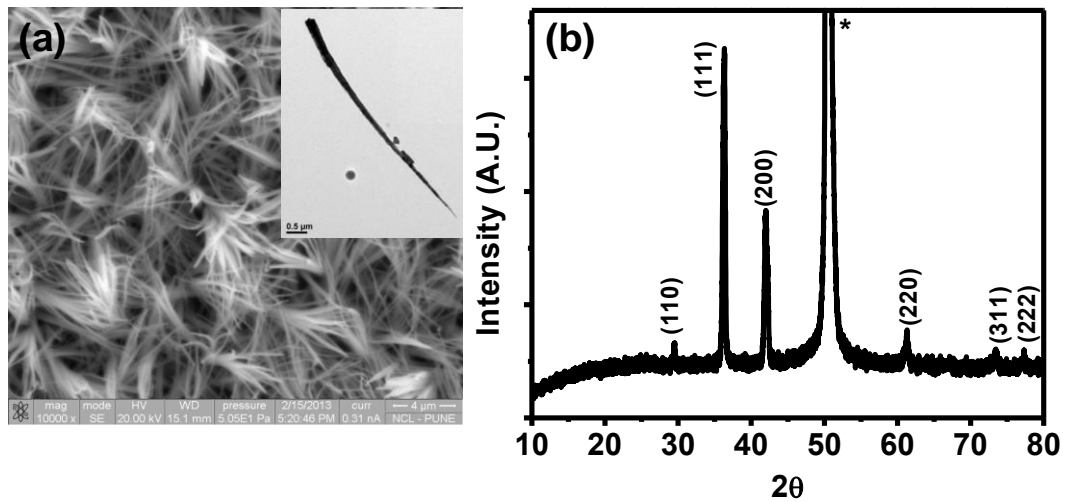


Figure 5.1: (a) SEM image of Cu₂O nanoneedles, Inset shows low-magnification TEM image of single nanoneedle, (b) X-Ray Diffraction pattern of Cu₂O nanoneedles. * represents copper substrate peaks

Figure 5.1 (b) shows the X-Ray Diffraction (XRD) pattern of this Cu₂O nanoneedles film. The XRD shows pure phase of Cu₂O nanoneedles on copper substrate, the peaks matching perfectly with cubic Cu₂O (JCPDS # 782076).

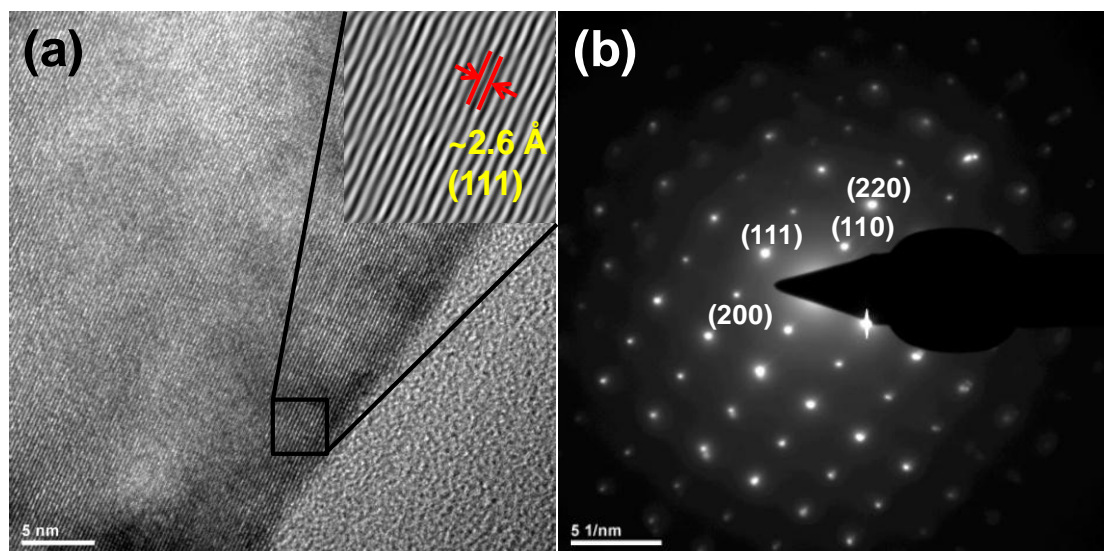


Figure 5.2: (a) HRTEM image recorded at the edge and (b) SAED pattern for single Cu₂O nanoneedle

The single Cu₂O nanoneedle was further investigated by HRTEM, as shown in figure 5.2 (a). Interestingly, one-dimensional growth was observed along (111) plane which was also confirmed by the lattice spacing of ~ 0.26 nm for (111) plane. The SAED pattern recorded on the entire nanoneedle is shown in figure 5.2 (b). The cubic diffraction spots corresponding to (111), (200) and (110) planes clearly indicate that the nanoneedle is single crystalline. As discussed earlier, it is highly desirable to synthesize quasi-1D Cu₂O with exposing (111) facets, for the application in PEC.

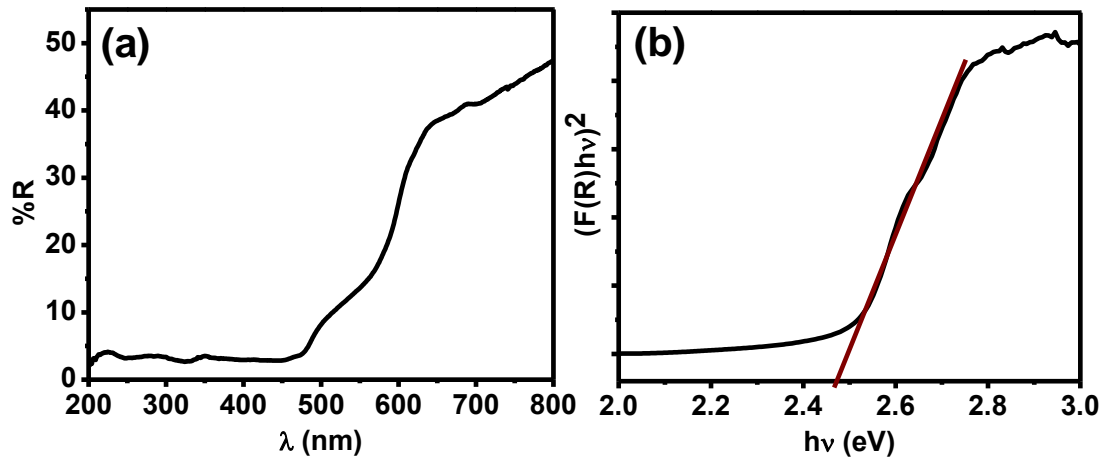


Figure 5.3: (a) Diffused reflectance spectra for Cu₂O nanoneedles film. (b) Tauc's plot for Cu₂O.

The optical absorption of Cu₂O nanoneedles film was studied using diffused reflectance spectroscopy (DRS), the data being shown in figure 5.3 (a). The energy gap of optically active semiconducting materials can be calculated by extrapolation of the tangent to Tauc's plots based on the equation ^[26, 27]:

$$[F(R)hv]^{1/n} \propto (hv - E_g)$$

Where $F(R)$ is modified Kubelka–Munk function,

$$F(R) = \frac{(1 - R)^2}{2R}$$

R is reflectance measured from the DRS of samples and $n = \frac{1}{2}$ for direct band gap material while $n = 2$ for indirect band gap material. From Tauc's plot of Cu₂O

nanoneedles, shown in figure 5.3 (b), the band gap (E_g) of the Cu₂O nanoneedles film is estimated to be ~ 2.46 eV. The band gap energy of Cu₂O nanoneedles is slightly higher as compared to that of bulk Cu₂O (~ 2.2 eV).

5.3.2 Mott – Schottky Plot

We carried out a Mott–Schottky analysis in order to determine the flat band potential for Cu₂O in the presence of Na₂SO₄ electrolyte. Mott–schottky plots were taken in the dark with three electrode assembly and perturbation amplitude of 10 mV in 0.05 M Na₂SO₄ aqueous electrolyte. Potential dependent electrochemical impedance spectroscopy measurements were performed in order to get the respective capacitances at semiconductor/electrolyte interface.

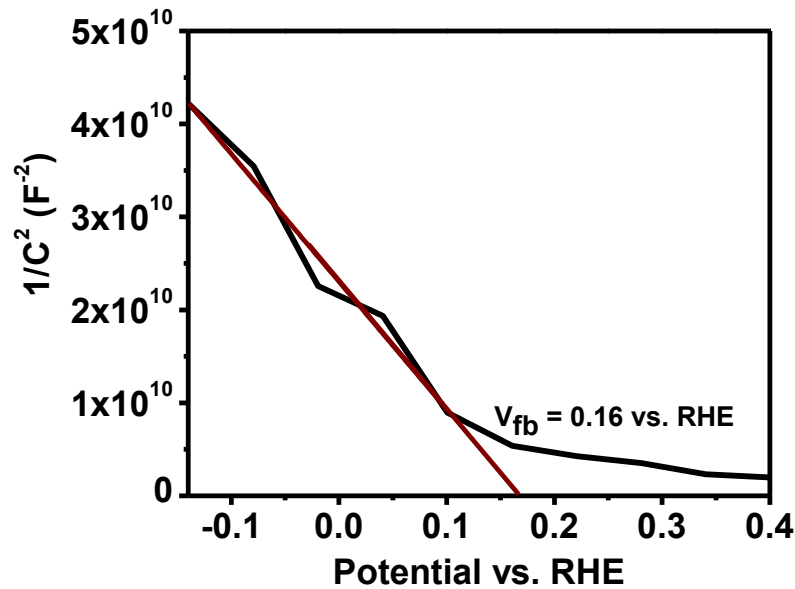


Figure 5.4: Mott – Schottky plot for Cu₂O film in aqueous Na₂SO₄ solution recorded at 5 kHz

In Mott Schottky plot $1/C^2$ is plotted against the applied potential. The intercept of linear portion of $1/C^2$ on the x-axis gives the value of the flat band potential, the slope of the curve gives the charge carrier density, and the width of space charge layer can be calculated by Mott-Schottky equation which is ^[28]:

$$\frac{1}{C^2} = \left(\frac{2}{e_0 \epsilon \epsilon_0 N_d} \right) q \left[(V - V_{FB}) - \frac{kT}{e_0} \right]$$

The charge density can be calculated by,

$$N_d = \left(\frac{2}{e_0 \varepsilon \varepsilon_0} \right) \left[\frac{d \left(\frac{1}{C^2} \right)}{dV} \right]^{-1}$$

where, ε_0 is permittivity of free space, ε is the dielectric constant which is 6.3 for Cu₂O^[29], e_0 is electronic charge, N_d is carrier density, and V_{FB} is the flat band potential. C is the interfacial capacitance, and e is the electronic charge (1.6×10^{-19} C).

Figure 5.4 shows the Mott–Schottky plot for the Cu₂O film measured at 5 kHz. The negative slope for Mott–Schottky plot implies the obvious p-type conductivity in Cu₂O. Extrapolating the linear region of the Mott–Schottky plots gives the flat band potential of the samples to be 0.16 V against reversible hydrogen electrode (RHE). The value for carrier density, N_d , as obtained from the slope of the Mott-Schottky plot is $1.6 * 10^{18} \text{ cm}^{-3}$.

5.3.3 Photo-electrochemical Measurements

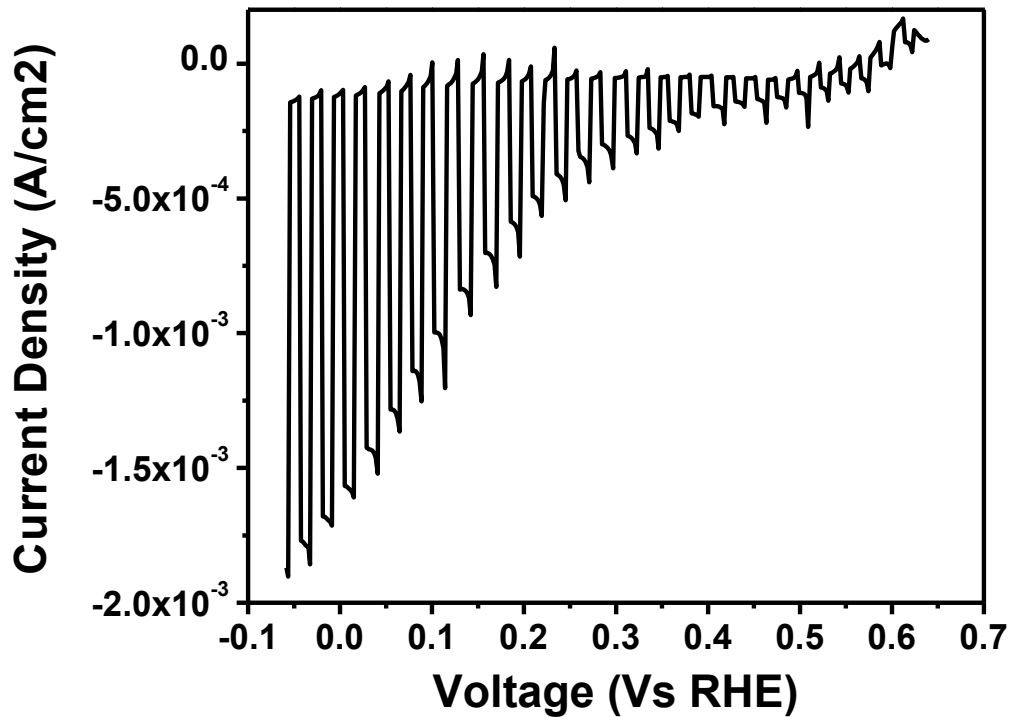


Figure 5.5: The photo-electrochemical response of Cu₂O nanoneedles film under the chopped solar-simulated light

The photo-electrochemical characteristics of Cu₂O nanoneedles were measured in a three-electrode electrochemical set up consisting of Cu₂O film as working, platinum foil as counter and Ag/AgCl as reference electrode. The electrolyte used was 0.05 M Na₂SO₄. No purging of gas was used during the measurements. Linear Sweep Voltammogram (LSV) was performed avoiding the oxygen evolution reaction above 0.65 V and reduction below -0.05 V vs. RHE. The photo-electrochemical current was measured under mechanically chopped light (solar simulator, AM 1.5 G), which was periodically chopped at the cycle of 5 seconds, so as to measure dark and light response simultaneously. The current was recorded while the voltage was changed at a scan rate of 5 mV. The corresponding voltage-current density data are presented in Figure 5.5. A significant photocathodic current of ~1.7 mA/cm² was observed at 0 V vs. RHE. This photo-induced cathodic current occurs due to the reduction of protons by photo-generated electrons at the Cu₂O/electrolyte interface. This good photocurrent can be assigned to the quasi-1D nature of the photoelectrode, which provides direct pathway for the separated charges after absorption of light to come to the surface. The nanoneedle nature of the film also leads to light harvesting inside the film, which can enhance the photocurrent significantly. The exposed (111) facets at the interface play a significant role in this enhancement, as they are most active due to dangling Cu-bonds.

5.3.4 Photo-stability of Cu₂O nanoneedles electrode

As Cu₂O is known to undergo photo-corrosion in PEC cell, it is important to study the stability of the Cu₂O photocathode. We have taken the stability data for Cu₂O nanoneedles in the same set up as that for PEC measurements. The transient photocurrent measurement taken at 0V vs. RHE is shown in figure 5.6. Interestingly, the initial photocurrent (~1.5 mA/cm²) reduces to ~0.6 mA/cm² which maintains itself after 5 minutes of light exposure. This ~ 40% retention can be considered as very good for the case of only Cu₂O. This can be attributed to the (111) exposed planes in our case. The stability obtained here is certainly good as compared to other reports, e.g. A. Paracchino *et. al.* have shown 0% stability after 20 minutes of light exposure for bare Cu₂O electrode ^[9], where mainly {100} facets of Cu₂O are exposed.

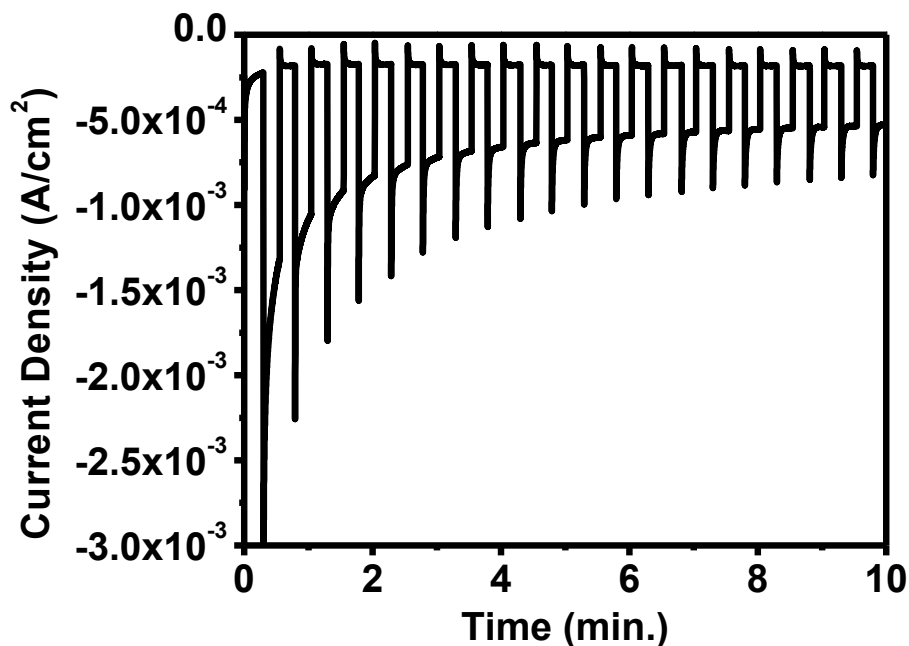


Figure 5.6: The transient photocurrent measurement of Cu₂O nanoneedles photocathode under the bias of 0 V vs. RHE

As indicated by H. Gerischer^[30], the photocurrent in the PEC cell depends drastically on surface orientations of crystal. Many factors such as flat band potential, energy positions, minority carrier diffusion length depend on surface orientation because of the polarization arising due to surface charge discrepancies. Also, depending on the surface states, the electrical double layer structure can be different. Besides this, corrosion reactions are controlled by charges present at the surface. In the case of Cu₂O the (111) facets are Cu⁺ terminated^[16,31]. When Cu₂O is used as photocathode in PEC; H⁺ ions migrating from anode cause the reduction of Cu₂O to Cu. But in the case of Cu⁺ terminated (111) surfaces, the H⁺ ions are not attracted to the surface avoiding the reduction of Cu₂O, as studied theoretically by Sowers et. al.^[16]. In our case, however, Cu₂O still undergo reduction to Cu reaction, and conversion of Cu to more stable phase CuO occurs at the surface, as oxygen is readily present in the reaction bath. This causes a formation of uniform coating of CuO on the surface of Cu₂O, avoiding further photo-corrosion. Therefore, the photocurrent decreases for the first few minutes, then maintains for 1 hr, as shown in

figure 5.7. This leads in the change of color from yellowish to blackish of the inserted Cu₂O film.

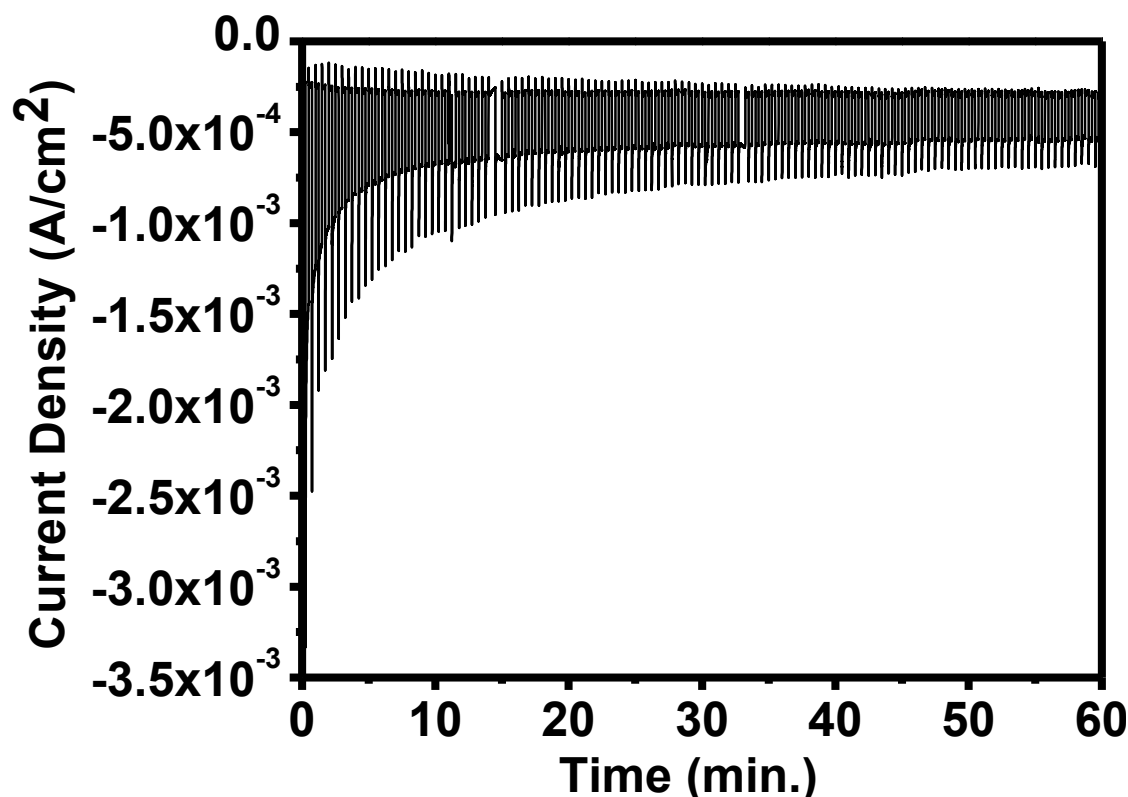


Figure 5.7: The current stability measurement of Cu₂O nanoneedles photocathode under the bias of 0 V vs. RHE for 1 hr

In light of the foregoing discussion it is clear that it may be very interesting to make a conformal coating of suitable material on the optimized Cu₂O nanoneedles surfaces for further enhancement and increased stability of the photoelectrode. We examined the case of TiO₂ coating in this respect.

5.3.5 Effect of TiO₂ coating

As Cu₂O/TiO₂ system forms a p-n junction for facilitating charge separation at the interface, a coating of TiO₂ on Cu₂O nanoneedles was implemented by a simple chemical route i.e. by TiCl₄ treatment. In our optimized experiment, we observed that TiCl₄ treatment for only 5 seconds followed by vacuum anneal treatment at 150°C leads to a good heterojunction film, which can be used as photocathode for PEC. The photoelectrochemical response for 5 second TiCl₄ treated Cu₂O is presented in figure 5.8. The photocurrent at 0 V vs. RHE is ~2.5 mA/cm², which has

increased dramatically than that of bare Cu₂O case. This increase in the current can be attributed to the favourable band alignment for charge separation at the Cu₂O/TiO₂ interface^[9, 32]. Although it is expected that the TiO₂ layer will protect the Cu₂O from photocorrosion, we did not observe improvement in stability for the case of TiCl₄ treated Cu₂O. This may be due to the non-uniform coating of TiO₂, where exposed underlying Cu₂O still undergoes the degradation upon light illumination.

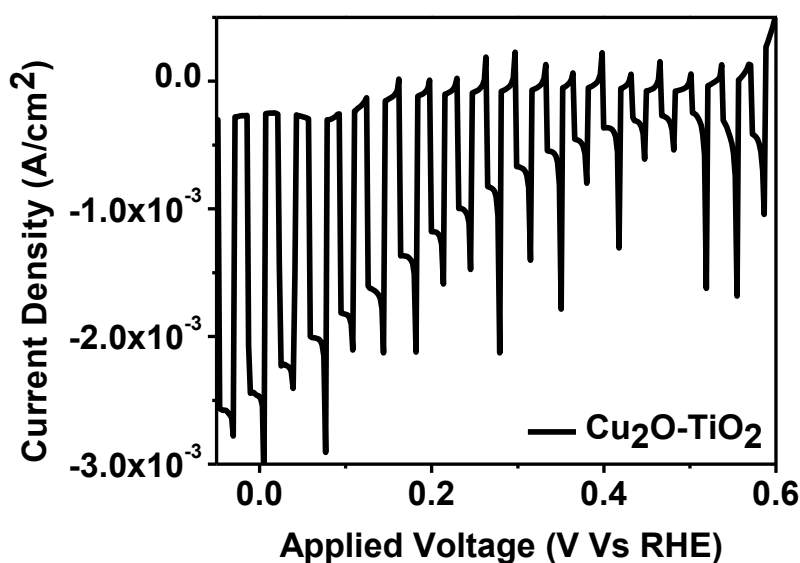


Figure 5.8: The photo-electrochemical response of TiO₂ (5 sec.) coated Cu₂O nanoneedles film under the chopped solar-simulated light

5.4 Conclusion

We have successfully grown single crystalline Cu₂O nanoneedles with (111) facets exposed to the surface on a copper foil. Such film gave a substantial photocurrent of ~ 1.7 mA/cm² and good stability over 1 hr, when used as a photocathode in PEC cell containing 0.05M Na₂SO₄ electrolyte having pH ~ 6.5 . The performance was further enhanced by coating ultrathin TiO₂ on the surface of Cu₂O by simple TiCl₄ treatment. This modification yielded a photocurrent of ~ 2.5 mA/cm² at 0V vs. RHE; however unfortunately the stability did not improve much possibly because of partial coverage of TiO₂. A technique such as atomic layer deposition (ALD) may be needed to circumvent this problem.

5.5 References

1. Hao Ming Chen, Chih Kai Chen, Ru-Shi Liu, Lei Zhang, Jiujun Zhang and David P. Wilkinson, *Chem. Soc. Rev.*, **2012**, 41, 5654–5671
2. Zhaosheng Li, Wenjun Luo, Minglong Zhang, Jianyong Feng and Zhigang Zou, *Energy Environ. Sci.*, **2013**, 6, 347–370
3. Roel van de Krol, Yongqi Liang and Joop Schoonman, *J. Mater. Chem.*, **2008**, 18, 2311–2320
4. T. Bak, J. Nowotny, M. Rekas, C.C. Sorrell, *International Journal of Hydrogen Energy*, **2002**, 27, 991 – 1022
5. Lingling Wu, Lok-kun Tsui, Nathan Swami, and Giovanni Zangari, *J. Phys. Chem. C*, **2010**, 114, 11551–11556
6. Michikazu Hara, Takeshi Kondo, Mutsuko Komoda, Sigeru Ikeda, Kiyooki Shinohara, Akira Tanaka, Junko N. Kondo and Kazunari Domen, *Chem. Commun.*, **1998**, 357.
7. Petra E. de Jongh, Daniel Vanmaekelbergh and John J. Kelly, *Chem. Commun.*, **1999**, 1069–1070.
8. H. Gerischer, *J. Electroanal. Chem.*, **1977**, 82, 133—143.
9. Adriana Paracchino, Vincent Laporte, Kevin Sivula, Michael Grätzel and Elijah Thimsen, *Nature Mater.*, **2011**, 10, 456.
10. Zhonghai Zhang and Peng Wang, *J. Mater. Chem.*, **2012**, 22, 2456.
11. Chia-Yu Lin, Yi-Hsuan Lai, Dirk Mersch and Erwin Reisner, *Chem. Sci.*, **2012**, 3, 3482–3487.
12. Zhonghai Zhang, Rubal Dua, Lianbin Zhang, Haibo Zhu, Hongnan Zhang, and Peng Wang, *ACS Nano*, **2013**, 7, 1709.
13. P. A. Morris Hotsenpiller, J. D. Bolt, and W. E. Farneth, J. B. Lowekamp and G. S. Rohrer, *J. Phys. Chem. B*, **1998**, 102, 3216-3226.
14. Kyoung-Shin Choi, *J. Phys. Chem. Lett.*, **2010**, 1, 2244–2250.
15. Zhaoke Zheng, Baibiao Huang, Zeyan Wang, Meng Guo, Xiaoyan Qin, Xiaoyang Zhang, Peng Wang, and Ying Dai, *J. Phys. Chem. C* **2009**, 113, 14448–14453.
16. Kelly L. Sowers and Akiko Fillinger, *Journal of the Electrochemical Society*, **2009**, 156, F80-F85.

17. Ho Seong Jang, Suk Jun Kim, and Kyoung-Shin Choi, *Small*, **2010**, 6, 2183–2190.
18. Wenyan Zhao, Wuyou Fu, Haibin Yang, Chuanjin Tian, Minghui Li, Yixing Li, Lina Zhang, Yongming Sui, Xiaoming Zhou, Hui Chen and Guangtian Zou, *Cryst Eng Comm*, **2011**, 13, 2871.
19. Yanchao Mao, Jintian He, Xiaofeng Sun, Wei Li, Xihong Lu, Jiayong Gan, Zhaoqing Liu, Li Gong, Jian Chen, Peng Liua, Yexiang Tong, *Electrochimica Acta*, **2012**, 62, 1–7.
20. Yu-Kuei Hsu, Chun-Hao Yu, Ying-Chu Chen and Yan-Gu Lin, *RSC Advances*, **2012**, 2, 12455–12459.
21. Jun-Nan Nian, Che-Chia Hu, Hsisheng Teng, *International Journal of Hydrogen Energy*, **2008**, 33, 2897 – 2903.
22. Swathi Sunkara, Venkat Kalyan Vendra, Jeong Hoon Kim, Thad Druffel, Mahendra K. Sunkara, *Catalysis Today*, **2013**, 199, 27–35.
23. (a) Salih Hacialioglu, Fei Meng, Song Jin, *Chem. Commun.*, **2012**, 48, 1174–1176 (b) P. E. de Jongh, D. Vanmaekelbergh, J. J. Kelly, *Journal of The Electrochemical Society*, **2000**, 147, 486-489.
24. Subas Muduli, Onkar Game, Vivek Dhas, Ashish Yengantiwar and Satishchandra B. Ogale, *Energy Environ. Sci.*, **2011**, 4, 2835-2839.
25. Meenal Deo, Sarfraj Mujawar, Onkar Game, Ashish Yengantiwar, Arun Banpurkar, Sneha Kulkarni, Jyoti Jog and Satishchandra Ogale, *Nanoscale*, **2011**, 3, 4706.
26. Ziyauddin Khan, Momina Khannam, Natarajan Vinothkumar, Mahuya De and Mohammad Qureshi, *J. Mater. Chem.*, **2012**, 22, 12090.
27. Yoshitaka Nakano, Shu Saeki, and Takeshi Morikawa, *Applied Physics Letters*, **2009**, 94, 022111.
28. Lily Mandal, Meenal Deo, Ashish Yengantiwar, Arun Banpurkar, Jyoti Jog, and Satishchandra Ogale, *Adv. Mater.*, **2012**, 24, 3686–3691.
29. Tengfei Jiang, Tengfeng Xie, Liping Chen, Zewen Fu and Dejun Wang, *Nanoscale*, **2013**, 5, 2938.
30. Heinz Gerischer, Chapter 1: “*The Influence of Surface Orientation and Crystal Imperfections on Photoelectrochemical Reactions at Semiconductor*

Electrode”; book - Photoeffects at Semiconductor-Electrolyte Interfaces; ACS Symposium Series, Vol. 146, **1981**.

31. Chun-Hong Kuo, Michael H. Huang, *Nano Today*, **2010**, 5, 106—116.
32. Withana Siripala, Anna Ivanovskaya, Thomas F. Jaramillo, Sung-Hyeon Baeck, Eric W. McFarland, *Solar Energy Materials & Solar Cells*, **2003**, 77, 229–237.

Chapter 6

Conclusion and Future Scope

This chapter presents a summary of the work with concluding remarks for the research performed and reported in this thesis and then lays out the future scope pertaining to this work.

6.1 Summary of the thesis

The research and development of electronic and optoelectronic devices leads to direct impact on our modern society, as most of them are used in day-to-day life. The rapid miniaturization and compact architecture of these devices has led to tremendously enhanced performance and cost reduction, but are restricted to only silicon based devices. Hence, the demand for other earth-abundant and cost effective materials with improved functionality and enhanced performance is growing. Metal oxides are considered to be good candidates in this respect because the range of electronic and optical properties they support is remarkable. Also, quasi 1D nanostructures have emerged as an important class of materials which facilitate, through controlled growth, making novel electronic and optoelectronic devices. The work on quasi 1D metal oxide nanostructures has witnessed considerable expansion during the past few years with fields such as field effect transistors, p-n junction diodes, sensors, solar energy conversion, etc. acquiring centre stage. Formation of heterojunction using such quasi 1D metal oxides widens the application domain even further due to integration of properties of both the materials and novel interface effects.

In the research work presented in this thesis, we have focused on the synthesis of p-type cuprous oxide (Cu_2O) nanoneedles and its heterojunctions with ZnO and TiO_2 using simple synthesis protocols. These materials have been studied for a few applications covering important current areas such as photo-sensing, field electron emission, photocatalysis and water splitting for hydrogen generation, etc.

The summary of the work done is as follows:

1. It is interesting to fabricate and study p-n junction using functional quasi 1D metal oxides and examine their opto-electronic properties. Therefore we synthesized Cu_2O nanoneedles by a simple anodization method followed by annealing in vacuum. A strong photo-response is realized in a simple flip-chip type rectifying junction configuration of Cu_2O nanoneedles and ZnO nanorods grown on metallic Cu and ITO, respectively. This response is shown to be two orders of magnitude stronger than that of a thin film hetero-

junction of the same materials. A ~120% resistance change was obtained under 1V reverse bias in the case of the nanowire junction.

2. To further improve the properties of the heterojunction, Cu₂O/ZnO hetero-nanobrush assembly has been synthesized directly on copper substrate by simple chemical route. The Cu₂O/ZnO hetero-nanobrush leads to the formation of multiple p-n junctions, and enhancement of the surface area and tip density. These properties are utilized in the applications of field electron emission and photocatalysis. We observed that for the Cu₂O/ZnO nanobrush case the field emission current increases and turn-on field decreases significantly in comparison to the case of Cu₂O nanoneedles. The Cu₂O/ZnO nanobrush structure is also shown to be a good candidate for photocatalysis as it degrades methyl orange very effectively than only Cu₂O nanoneedles.
3. Cuprous oxide, having band gap ~2.2 eV, is considered to be a very good photocathode material for photo-electrochemical (PEC) water splitting. It is important to investigate Cu₂O with high surface area and high activity grown on desired substrate for photo-electrochemical hydrogen generation. Hence we have grown single crystalline Cu₂O nanoneedles, with (111) facets exposed to the surface directly on a copper foil. Such film gave a substantial photocurrent of ~1.7 mA/cm² at 0V vs. RHE and good stability over 1 hr, when used as a photocathode in PEC cell containing 0.05M Na₂SO₄ electrolyte having pH ~6.5. The performance was further enhanced by coating ultrathin TiO₂ on the surface of Cu₂O by simple TiCl₄ treatment. This modification gave the photocurrent of ~2.5 mA/cm² at 0 V vs. RHE; however the stability did not improve much.

6.2 Scope for future work

Quasi 1D metal oxides are explored as the possible building blocks for the future electronic and opto-electronic technologies. But for their practical use, a control over structure and morphology during growth, which determines their properties, is a key parameter. Also, one should keep in mind that the materials used should overcome the cost and efficiency challenges and secondly they should be capable of long term

stability. Keeping these aspects in mind, a few possible points pertaining to the possible future work based on the outcome of current thesis work are as follows:

1. Organic-inorganic photodetectors with enhanced performance than its individual constituents have attracted much attention recently. This device structure combines inorganic material having high carrier mobility and organic material with good flexibility and low temperature processability. Therefore it would be interesting to study a photodetector designs based on p-Cu₂O as the inorganic component and an n-type polymer or ionic liquid, with proper band alignment with Cu₂O, as an organic component, in a quasi liquid-solid hybrid device. Certainly, an optimization would be required for such device to work as 'self-powered' photodetector.
2. In flat-panel displays, conducting carbon based nanomaterials are used as very efficient field electron emitters, because of their low work function and high conductivity. Formation of uniform thin film of graphitic carbon is possible by physical deposition techniques like PLD. Therefore it is important to deposit conducting carbon on aligned arrays of metal oxide nanowires by pulsed laser deposition (PLD) and study their field emission properties for future field emission displays.
3. Photo-electrochemical (PEC) cell containing a semiconductor as an electrode splits water under sunlight generating hydrogen with high efficiency. But, practically there are not many materials which have an ideal band gap and band alignment with hydrogen and oxygen evolution levels of water. Cu₂O has nearly ideal band gap of ~2 eV having proper alignment with water reduction level. Unfortunately, it gets corroded under illumination in aqueous environment due to slightly slow electron transfer across semiconductor/water interface. Therefore to protect the corrosion and to facilitate fast electron transfer across the junction, Cu₂O should be covered with another suitable material. Metal chalcogenites are used in solar cells and PEC cells for their visible light absorbing properties and good catalytic function. Cu₂S, is one of the less explored metal chalcogenites, can be easily grown on the surface of Cu₂O by controlled sulphurization and can be used as

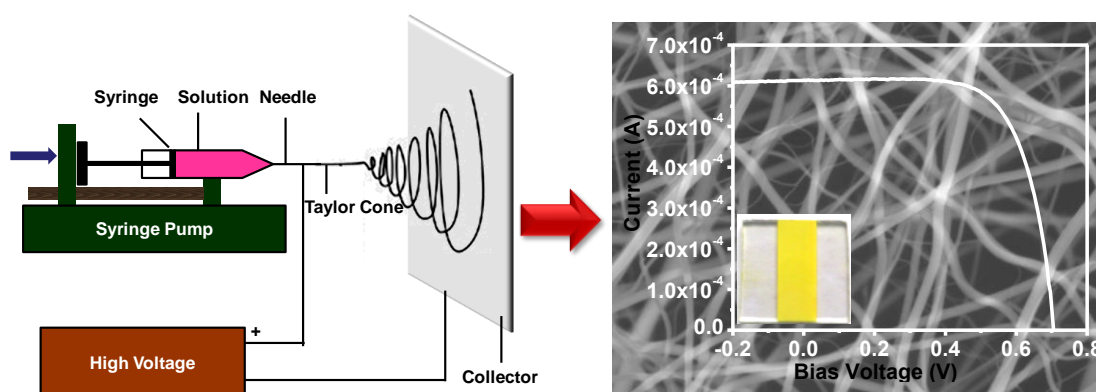
a protecting layer on Cu_2O when used as photocathode for PEC water splitting.

4. The design of an efficient system for direct water splitting using abundantly available sunlight and water is a current challenging task for scientific community. One approach has proposed construction of a tandem PEC cell having n-type and p-type materials in contact with each other, where hydrogen will be evolved at p-side and oxygen on the n-side. The cell design should be such that the potential developed should be enough for the water splitting reaction i.e. it should be self-biased cell and the band gap of the materials should be such that they will absorb maximum portion of the solar spectrum. Since there are a lot of options for stable n-type materials, synthesis of a suitable p-type material is very important. A surface-protected photo corrosion-free Cu_2O nanostructure is attractive in this respect.
5. In the PEC cell containing Cu_2O as photocathode, the photo-generated electrons which cannot be transferred to the electrolyte efficiently cause reduction of Cu_2O itself leading to its photo-corrosion. To avoid the accumulation of these electrons on the surface of Cu_2O and to protect the Cu_2O surface an electron scavenger molecule like methyl viologen can be used in the electrolyte in PEC cell.

Appendix - I

Fabrication of Anatase TiO₂ Nanofibers by Electrospinning for Dye and Quantum Dots Sensitized Solar Cells

Anatase TiO₂ nanofibers represent another quasi-1D system of current optoelectronic interest. In this work such fibers have been synthesized by electrospinning method. These electrospun TiO₂ nanofibers are used to prepare working electrode in Dye Sensitized Solar Cell (DSSC) and Quantum Dot Sensitized Solar Cell (QDSSC). A power conversion efficiency of ~4.4% was obtained for DSSC. Moreover, this value was seen to get enhanced when the nanofibers were used to form a light harvesting layer (~6%) or mixed with ~20 nm TiO₂ nanoparticles for the fabrication of DSSC (~6.5%). These TiO₂ nanofibers also show substantial efficiency in the case of CdS sensitized solar cells.



A-I.1 Introduction

Dye sensitized solar cells (DSSC) have attracted a lot of attention recently as a promising alternative to silicon solar cells because of their low production cost and reasonable efficiency ^[1]. In DSSC, a film of metal oxide nanoparticles, sensitized by a dye, on conducting glass is used as photoelectrode and an electrolyte is sandwiched in between such photoelectrode and another conducting glass with a specific catalyst. The dye generates excitons upon absorption of photons; the free electrons are injected into metal oxide nanoparticles and transported to adjacent conducting glass for charge collection. Meanwhile, the holes in the dye are compensated by redox reaction occurring in the electrolyte thereby getting transferred to another electrode. More the collection of charges, higher is the efficiency. Nanostructured TiO₂ is considered as one of the most important materials used as photoanode in DSSC ^[2]. Basically, TiO₂ occurs in nature in three different polymorphs: rutile, anatase, and brookite. Amongst all these phases, anatase TiO₂ shows better efficiency and more photocatalytic activity because of its favourable properties and great stability in aqueous/organic medium.

Metal oxide photoanodes used for DSSC should have higher surface area so that there should be higher dye loading. Enhanced mobility of the electrons through the metal oxide nanochannels is another requirement for the achievement of good efficiency ^[3]. Recently, photoanodes comprising of anisotropic nanostructures (e.g. nanorods, nanotubes, nanowires etc.) are being examined with interest in this context. These quasi-1-dimensional (1-D) nanostructures have received growing attention as charge transport media for their semi-directed transport capability, reduction of grain boundaries and hence less recombination of charge carriers compared to spherical particles. They can also have high porosity and specific surface area which increases the dye adsorption. Moreover, 1-D nanostructures also show improved light scattering effect which enables its use as light harvesting layer in DSSC ^[4]. But, it is difficult to form anisotropic morphologies of TiO₂ due to its tetragonal structure with almost equal (a,b,c) values. Hence electrospinning can be used for the fabrication of nanofibers or nanorods of TiO₂.

Electrospinning is a well-established and cost-effective technique for large-scale production of quasi-1-D nanostructures of polymers as well as other advanced

ceramic materials, when combined with sol-gel process ^[5]. Electrospinning method can produce ultra-fine fibers or fibrous structures of various polymer based solutions with diameters down to submicrons or few nanometers.

In this work, we have synthesized electrospun TiO₂ nanofibers and used them as an active photoanode material for efficient DSSC. To make use of both, good dye uptake of TiO₂ nanoparticles and electron transport property of TiO₂ nanofibers, we have used hybrid structure of TiO₂ nanoparticle-nanofibers ^[6] in an optimized percentage to get maximum efficiency for DSSC. Also, because of the favorable light scattering property, TiO₂ nanofibers have been used as a light harvesting layer in photoelectrode.

More recently, quantum dots (QDs) are being explored intensively as novel sensitizers, instead of dye molecules, for their probable multi-excitons generation which elevates the theoretical efficiency as high as 44%. Recently, metal chalcogenide quantum dot (QD) semiconductors such as CdS, CdSe, PbS, and PbSe have been tried as sensitizers for the solar cells, instead of Ruthenium based dyes ^[7]. These systems are referred as next-generation sensitizers as they are expected to provide the advantage of facile tuning of effective band gap down to the IR range by changing their sizes and compositions. Among the semiconductor QD sensitizing materials, CdS is a promising candidate for its bulk band gap of ~2.4 eV and flat band edge at 0.66 V (pH 7), rendering it capable of absorbing visible light and form a favorable band alignment with TiO₂ for efficient electron injection ^[8]. Considering all these advantages, we have fabricated CdS coated TiO₂ nanofiber photoelectrodes for reasonably efficient QDSSCs.

A-I.2 Experimental

A-I.2.1 *Synthesis of Electrospun TiO₂ Nanofibers:*

We have employed electrospinning method for the synthesis of TiO₂ nanofibers by using mixture of TiO₂ sol and polyvinylpyrrolidone (PVP) solution. In our optimized process, we first dissolved 1 gm polyvinylpyrrolidone (PVP) [mol. Wt. 1,300,000] completely into 9 ml ethanol. 10 µl concentrated HNO₃ (70%) was added drop-wise to this polymer solution. Titanium Tetraisopropoxide (TiP) was used as

precursor for TiO₂ sol, 5 ml of which was then added slowly and the solution was stirred overnight to form uniform, viscous solution for electrospinning. The solution was loaded in 10 ml syringe connected with stainless steel needle having inner diameter ~0.2 mm. An electric field of ~1 kV/cm was applied between the needle and a metallic collector plate, placed in front of the syringe and covered with aluminium foil, using high voltage power supply. The flow rate of 1ml/hr was kept fixed. The collected electrospun fibers on aluminium foil were dried under IR lamp for 15 minutes. The fibers were then annealed at heating rate of 1 °C/min to 500°C for 1 hr to obtain anatase TiO₂ nanofibers. The electrospun TiO₂ nanofibers were further characterized by XRD, SEM and TEM.

A-I.2.2 Fabrication of photoanode for DSSC

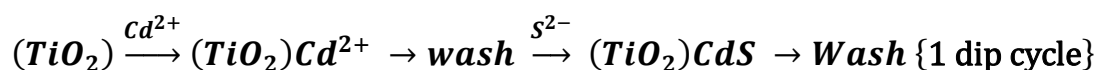
Films of the TiO₂ nanofibers were made using the standard protocol of doctor blading method^[9]. The TiO₂ nanofibers were first crushed to form uniform nanorods paste in an agate mortar with small amount of water, Triton X-100, ethanol, dilute acetyl acetone, dilute acid and binding agents (Poly ethylene glycol). To produce uniform films from this paste, “Doctor Blade” coating method was used. The coated film was allowed to air dry for 10 mins and then heated for 1 hr at 450°C to form electrical bridges between the TiO₂ nanocrystals. The films were post-treated with TiCl₄ to improve the electron transport. For the nanoparticle-nanofibers hybrid structure films, TiO₂ nanofibers were mixed and ultra-sonicated with lab-synthesized TiO₂ nanoparticles (of size ~20 nm) in ethanol in the desired amount for 30 minutes, and then heated at ~70°C under constant stirring to get uniform viscous paste. The films were then coated with Doctors blade method.

For dye sensitization, the films were dipped in N719 dye in ethanol for 24 h at room temperature. The samples were then rinsed with ethanol to remove excess dye on the surface and air-dried at room temperature. The active area of all the cells for DSSC was kept as 0.25 cm² by scratching other area of the film. To form the solar cell assembly, the film was sandwiched with the counter electrode of Pt coated FTO followed by addition of redox electrolyte. The electrolyte used was iodine/triiodide in acetonitrile. The I-V characteristics were measured under exposure of 100 mW/cm² (450W xenon lamp, Newport Instruments), 1 sun AM 1.5, simulated

sunlight as a solar simulator. The current was measured using a Keithley 2400 source.

A-I.2.3 Deposition of CdS quantum dots

The CdS QDs were deposited on the TiO₂ nanofibers electrode by successive ionic layer adsorption and reaction” (SILAR) method^[10]. In this method, dissolved cationic and anionic precursors are reacted slowly in one bath or separated into two containers; the bare electrode is dipped alternatively into each one, to grow the target QDs. Here, we have used non-aqueous solutions of reactants: 0.2 M Cd(NO₃)₂ and 0.2 M Na₂S in ethanol and methanol, respectively. Particularly non-aqueous solution was chosen because they have lower surface tension and thus have better penetrating ability through the porous matrix than aqueous solution. The films of TiO₂ nanofibers were dipped for 5 minutes each and then rinsed thoroughly with respective solvents. The ionic state of the reactants Cd²⁺ and S²⁻ ions could thus penetrate the TiO₂ film and incorporate into the inner region of a mesopore. Scheme A-I.1 illustrates the steps involved in the SILAR method. All the TiO₂ films used for QDSSC were made up of thin layer of TiO₂ nanoparticles (of size ~20 nm) underneath the TiO₂ nanofibers and of overall thickness ~12 μm. The CdS deposition cycles were varied from 4 to 10. The deposition of CdS on TiO₂ nanofibers was confirmed by further characterization of the film using XRD, DRS and SEM.



Scheme A-I.1: CdS Sensitization process on TiO₂ film

A-I.3 Results and discussion

A-I.3.1 Characterization of TiO₂ nanofibers

The as synthesized TiP-PVP electrospun fibers have diameters of ~100 - 300 nm and lengths of few microns, as seen by SEM image in figure A-I.1 (a). After sintering of the nanofibers, the morphology remains almost the same however the diameter slightly decreases because of PVP evaporation from the system. The TiO₂ nanofibers, as seen from SEM image in figure A-I.1 (b), have diameters ~100 - 200 nm. The TEM image in figure A-I.1 (c) indicates that the single

nanofiber is polycrystalline and consists of TiO₂ crystallites or grains with sizes of ~10 nm. TEM also shows that the grains are densely packed in the fiber. The HRTEM in figure A-I.1 (d) shows that the interplanar spacing (d) is ~0.36 nm, suggesting that the TiO₂ crystallites in the nanofibers are in the anatase phase.

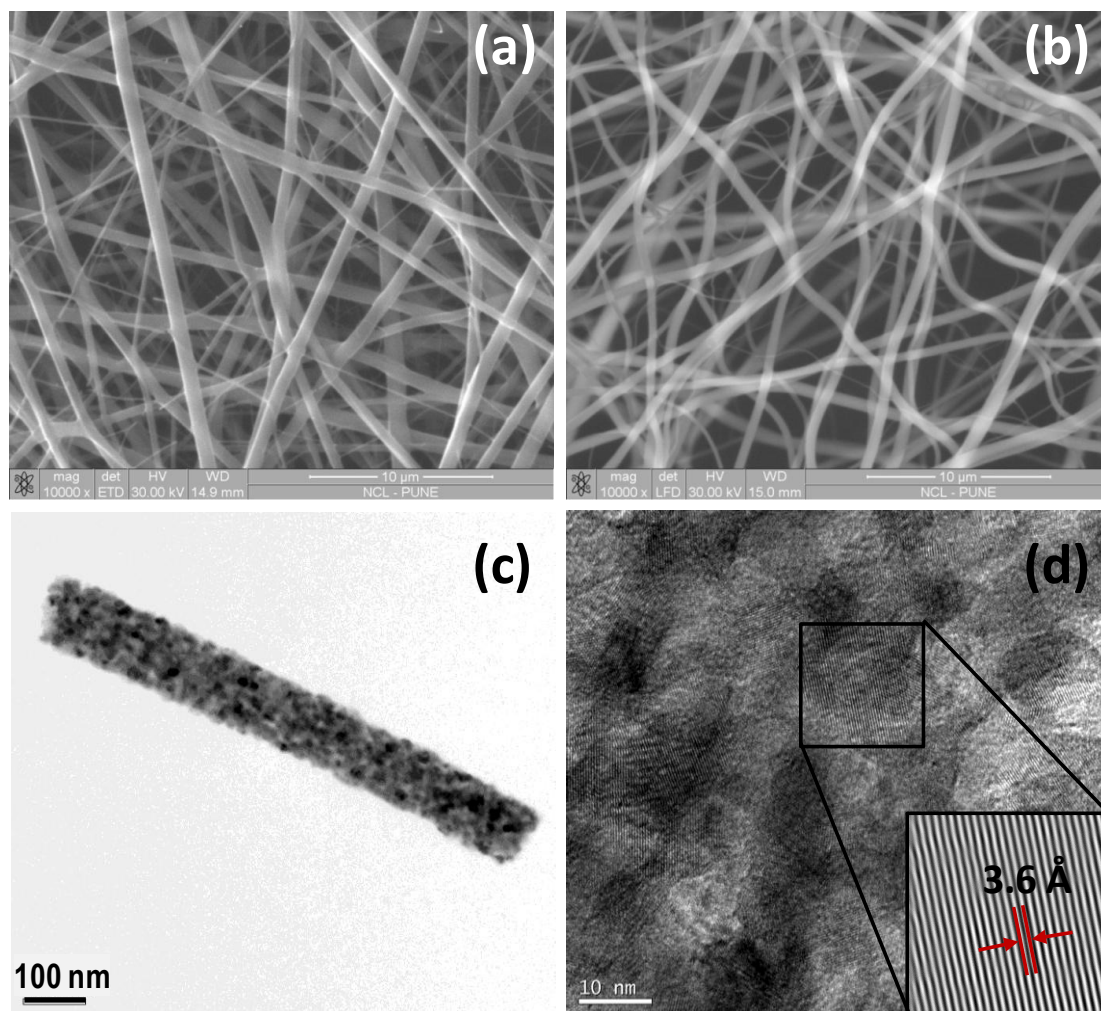


Figure A-I.1: SEM images of (a) as synthesized TiP-PVP nanofibers, (b) annealed TiO₂ nanofibers; (c) TEM and (d) HR-TEM image of single TiO₂ nanofiber; inset of (d) shows d-spacing of single TiO₂ grain

The pure anatase phase of TiO₂ nanofibers was further confirmed by the XRD pattern of the nanofibers as shown in figure A-I.2 and compared with standard JCPDS data #211272. The XRD pattern also shows polycrystalline nature of TiO₂ without any polymeric part after annealing at 500°C for 1 hr, as expected. The anatase phase of TiO₂ is important because it possesses a higher electron transport capability than the rutile phase of TiO₂, leading to a better photovoltaic performance.

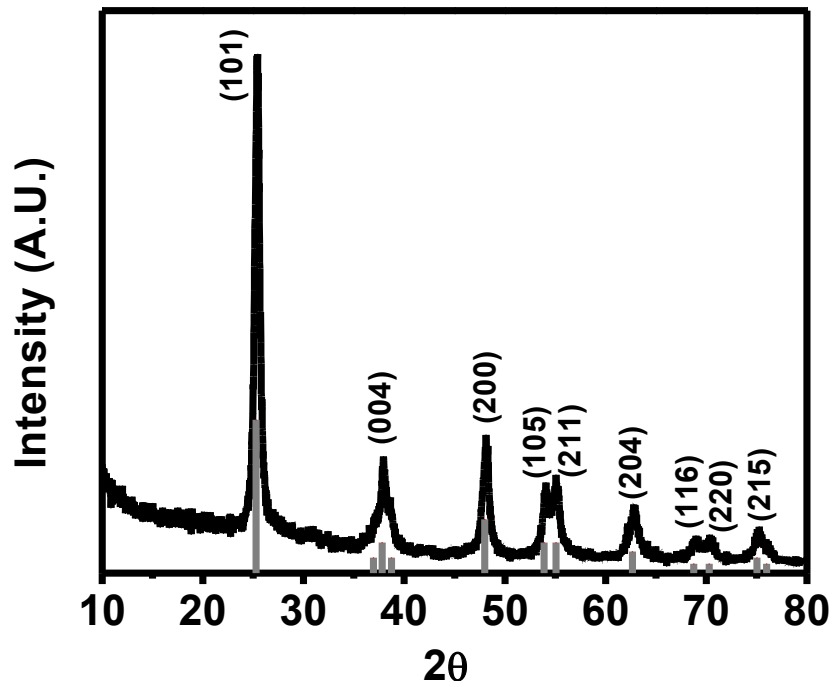


Figure A-I.2: X-Ray Diffraction pattern of annealed TiO₂ nanofibers

A-I.3.2 Photovoltaic characterizations of DSSC

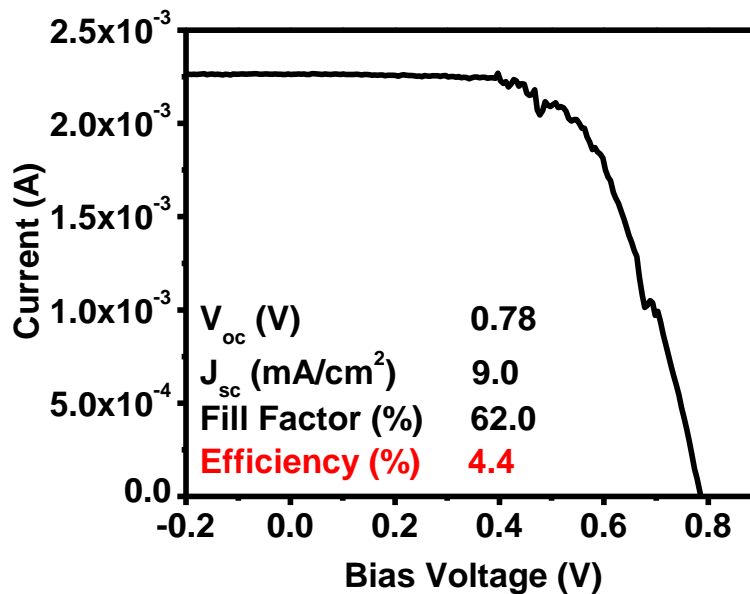


Figure A-I.3: Current- Voltage (J-V) curve for photoelectrode made up of only TiO₂ nanofibers

When only TiO₂ nanofibers were used as active material for photoanode in DSSC, the solar cell efficiency of ~4.4% was obtained. This comparatively low efficiency is due to low dye loading on the electrospun nanofiber films as compared

to the TiO₂ nanoparticles film. This is due to the voids present in between the nanostructured TiO₂ nanofibers film. To fill these voids and to increase the dye loading, we mixed the TiO₂ nanofibers with TiO₂ nanoparticles in specific percentage. This hybrid structure has the advantage of both: good dye adsorption in the case of spherical particle surface, while the presence of nanorods renders faster electron transport rate and favorable light scattering as well. By comparing the J-V curves of only TiO₂ nanofibers case (figure A-I.3) and 30% TiO₂ nanofibers in TiO₂ nanoparticles case (figure A-I.4 (a)), it is clear that there is a drastic improvement in the current (J_{sc}) and hence improvement in efficiency of ~6.5% in case of hybrid structure. This shows improvement in efficiency of ~45% by the use of nanoparticles. It is also worth noting here that in the prepared composite films the electrospun TiO₂ nanofibers were randomly distributed amongst the TiO₂ nanoparticles. The nanofibers scatter the incident light effectively inside the film, resulting in a substantial improvement in light harvesting^[11]. We have studied the efficiency variation by varying the amount of TiO₂ nanofibers and we got maximum efficiency for the photoelectrode consists of 30% nanofibers mixed with 70% nanoparticles, as shown in figure A-I.4 (b).

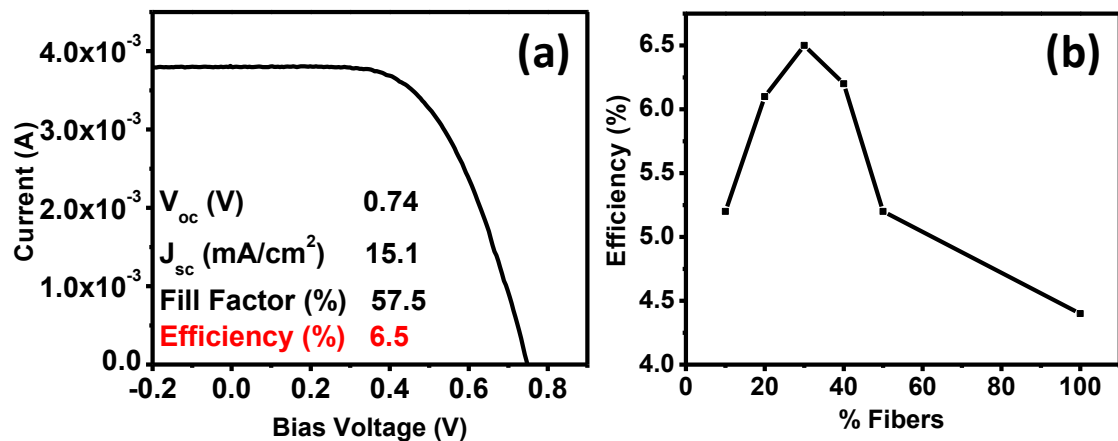


Figure A-I.4: (a) Current – Voltage (J-V) curve for 30% TiO₂ nanofibers in TiO₂ nanoparticles case (b) Efficiency as increasing percentage of nanofibers in nanoparticles

Generally, it is observed that small nanoparticles used in photoelectrode can not scatter the incident light leading to poor light harvesting. Hence it is useful to make thin transparent layer of small nanoparticles below the light scattering layer for

effective light harvesting and hence effective current enhancement in the DSSC. The light scattering layer usually consists of nanoparticles of size $\sim 100 - 200$ nm^[12]. Here, we have used the TiO₂ nanofibers as scattering layer in the DSSC. For this we deposited the transparent TiO₂ (of particle size ~ 20 nm) thin film underneath and deposited a layer of electrospun nanofibers on the top. In this case the electrospun nanofibers proved to be beneficial as the light harvesting layer and gave higher efficiency of 6%, which was higher by almost 36%, as shown in figure A-I.5.

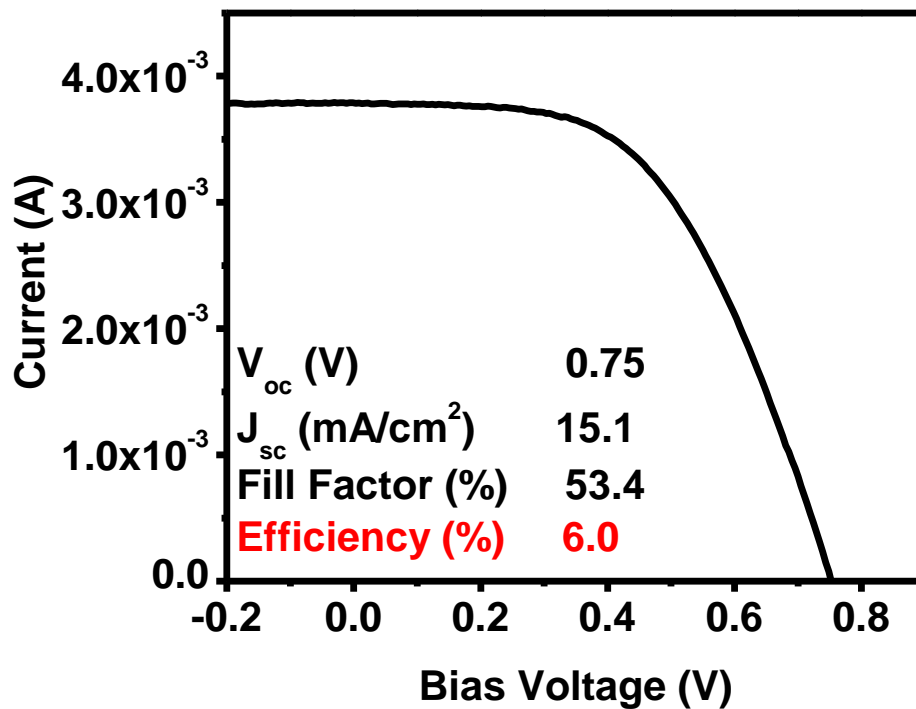


Figure A-I.5: Current- Voltage (J-V) curve for photoelectrode made up of TiO₂ nanofibers as scattering layer on thin TiO₂ nanoparticles film

It is noteworthy that here the inward Mie scattering of light by nanofibers leads to reduction of reflectance which in turn increases the light absorption in the film. The Mie scattering taking place here is most effective for nanofibers of diameter $\sim 100 - 200$ nm^[11, 12]. Thus, by optimizing the electrospinning parameters further we can optimize the efficiency of DSSC. The overall DSSC results are shown in table A-I.1.

Film	V _{oc} (V)	I _{sc} (A)	FF(%)	η (%)
TiO ₂ Nanofibers	0.78	9.0	62.0	4.4
Thin TiO ₂ nanoparticles layer + TiO ₂ Nanofibers	0.75	15.1	53.4	6.0
Film of TiO ₂ nanoparticles + TiO ₂ Nanofibers (30%)	0.74	15.1	57.5	6.5

Table A-I.1: Solar cell parameters of DSSC made from different configuration of electrospun TiO₂ nanofibers

A-I.3.3 Characterization of CdS sensitized TiO₂ film

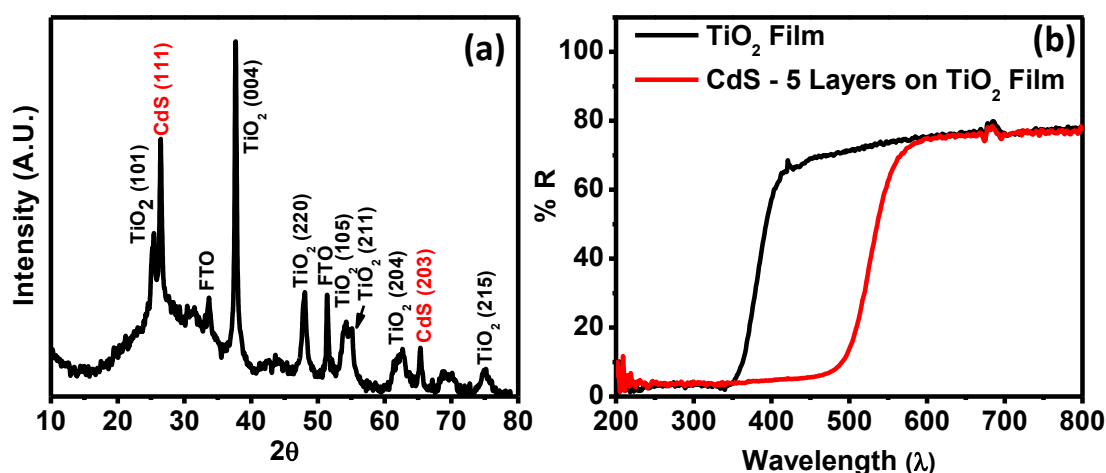


Figure A-I.6: (a) XRD and (b) DRS of CdS (5 layers) deposited on TiO₂ nanofibers film

We also performed experiments on CdS QD sensitized solar cells. The formation of CdS, after 5 SILAR cycles of deposition (most efficient case for QDSSC), on TiO₂ nanofibers film was confirmed by XRD as shown in figure A-I.6 (a). All the peaks are indexed to anatase TiO₂, CdS and FTO confirming with standard JCPDS data. This validates the usefulness of simple SILAR method for the deposition of CdS on TiO₂ nanorods. The Diffused Reflectance Spectra (DRS) of 5 layers of CdS deposited on TiO₂ nanofibers film is shown in figure A-I.6 (b). It is clear that after

CdS deposition the absorption red-shifts corresponding to the visible light absorption of CdS. The band gap of CdS as calculated from the DRS is ~2.5 eV.

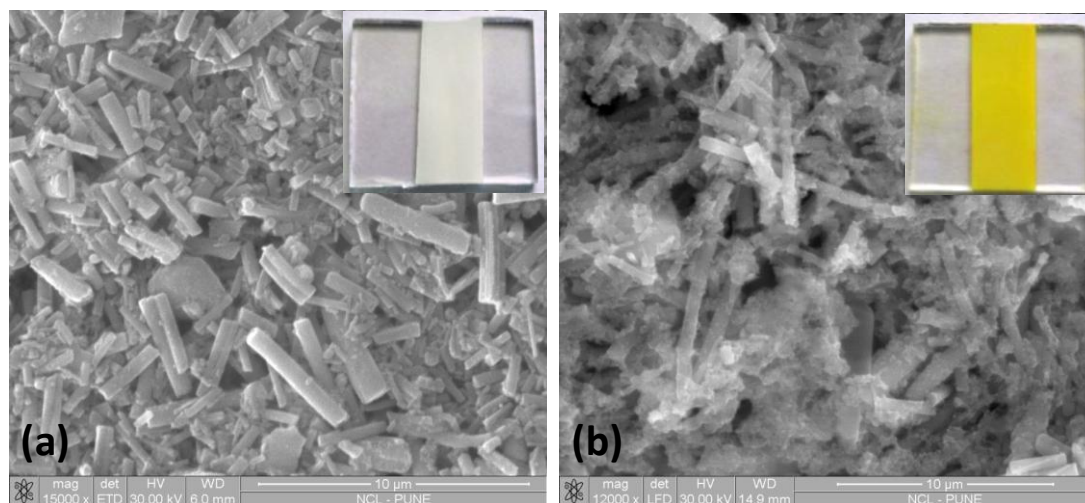


Figure A-I.7: SEM images showing (a) as deposited TiO₂ nanofibers on FTO and (b) CdS (5 layers) deposited on TiO₂ nanofibers, insets show photographs of respective films

The surface morphology of only TiO₂ nanofibers film and 5 layers CdS deposited TiO₂ nanofibers film are shown in figure A-I.7 (a) and (b) respectively. The clear change in color of the film can be seen in the photographs shown in respective insets. As the fibers get crushed when we make TiO₂ films by usual Doctor's blade method, the morphology of only TiO₂ film shows the formation of randomly oriented TiO₂ nanorods, although the 1D nature retains even after the crushing. After 5 SILAR cycles of CdS on TiO₂ film, there is a formation of CdS nanoparticles uniformly on TiO₂, but there is no evidence of formation TiO₂-CdS core-shell heterojunction.

A-I.3.4 *Photovoltaic characterizations of CdS Sensitized solar cells*

The photovoltaic characterization of CdS sensitized solar cells was performed by sandwiching the CdS deposited TiO₂ photoelectrode with Pt coated FTO and inserting iodine/triiodide electrolyte in it. The active area of the cell was kept 0.16 cm². The best performance we achieved was for 5 SILAR cycles case with an open-circuit voltage of 0.7 V, a short-circuit photocurrent density of 3.8 mA/cm², a fill factor of ~69% and an overall power-conversion efficiency of ~1.8%.

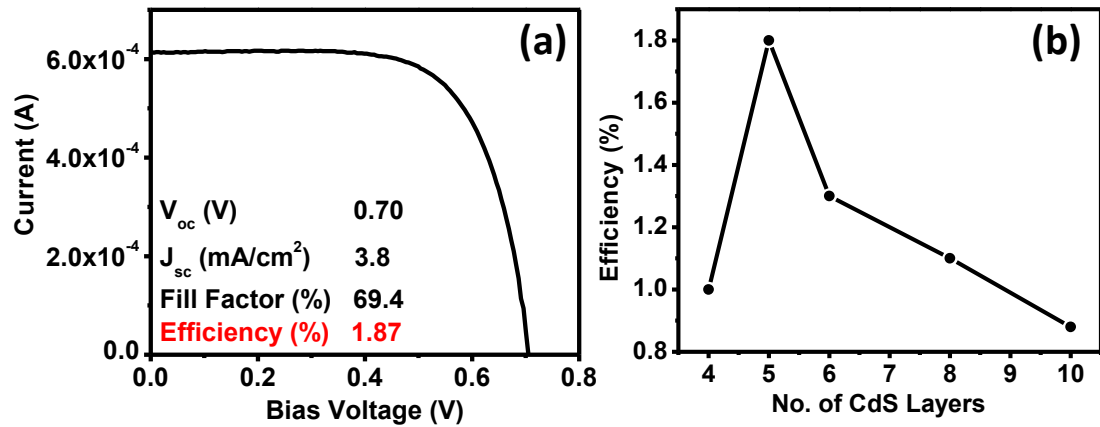


Figure A-I.8: (a) Current – Voltage (J-V) curve for 5 layers of CdS deposited on TiO₂ nanofibers (b) Efficiency as a function of increasing CdS deposition cycles on TiO₂ nanofibers film

The photovoltaic performance realized by varying the SILAR cycles is shown in figure A-I.8 (b). It is observed that less SILAR cycles can not deposit sufficient CdS for maximum absorption of incident light. On the other hand more SILAR cycles lead to overloading of CdS which blocks electrolyte percolation and also serves to enhance recombination^[13]. This leads to decrease in the current density, thus hampering the efficiency. We believe that the 1D nature of TiO₂ nanofibers plays significant role in electron transport and light harvesting for overall enhancement in the efficiency.

A-I.4 Conclusion

In conclusion, we have successfully used TiO₂ nanofibers for both DSSC and QDSSC systems. We achieved the best performance efficiency of ~ 6.5% for DSSC, using TiO₂ nanofibers (30%) - nanoparticles hybrid structure. For the case of CdS sensitized solar cells, we repetitively achieved ~1.8% efficiency for the case of 5 SILAR layers of CdS on TiO₂ nanofibers. To obtain enhancement in the efficiency, further optimization of the solar cell fabrication process as well as optimization of TiO₂ nanofibers synthesis process are needed.

A-I.5 References

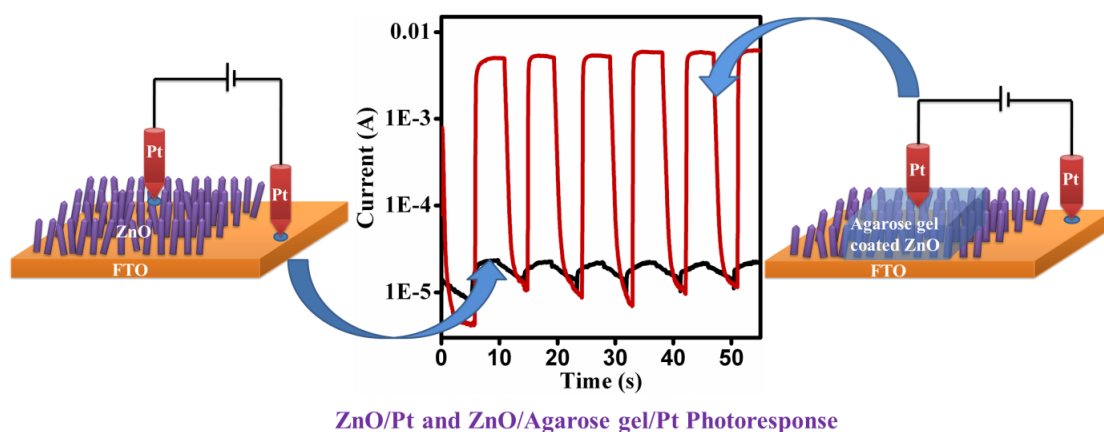
1. B. O'Regan and M. Grätzel, *Nature*, **1991**, 353, 737 – 740.

2. Subas Muduli, Onkar Game, Vivek Dhas, Ashish Yengantiwar, Satishchandra B. Ogale, *Energy Environ. Sci.*, **2011**, 4, 2835-2839.
3. Gopal K. Mor, Karthik Shankar, Maggie Paulose, Oomman K. Varghese, Craig A. Grimes, *Nano Lett.*, **2006**, 6, 215-218.
4. (a) Mi Yeon Song, Young Rack Ahn, Seong Mu Jo, Dong Young Kim, Jae-Pyoung Ahn, *Appl. Phys. Lett.*, **2005**, 87, 113113 (b) Meidan Ye, Xukai Xin, Changjian Lin, Zhiqun Lin, *Nano Lett.*, **2011**, 11, 3214–3220.
5. (a) Xiaofeng Lu, Ce Wang, Yen Wei, *Small*, **2009**, 5, 2349–2370 (b) R. Sahay, P. Suresh Kumar, R. Sridhar, J. Sundaramurthy, J. Venugopal, S. G. Mhaisalkar, S. Ramakrishna, *J. Mater. Chem.*, **2012**, 22, 12953, (c) Dan Li, Jesse T. McCann, Younan Xia, Manuel Marquez, *J. Am. Ceram. Soc.*, **2006**, 89, 1861–1869.
6. Bing Tan, Yiyang Wu, *J. Phys. Chem. B*, **2006**, 110, 15932-15938.
7. Yuh-Lang Lee, Yi-Siou Lo, *Adv. Funct. Mater.*, **2009**, 19, 604–609.
8. Wen-Tao Sun, Yuan Yu, Hua-Yong Pan, Xian-Feng Gao, Qing Chen, Lian-Mao Peng, *J. Am. Chem. Soc.*, **2008**, 130, 1124 – 1125.
9. Shruti A. Agarkar, Roshan R. Kulkarni, Vivek V. Dhas, Ashish A. Chinchansure, Partha Hazra, Swati P. Joshi, Satishchandra B. Ogale, *ACS Appl. Mater. Interfaces*, **2011**, 3, 2440–2444.
10. Hyo Joong Lee, Jiwon Bang, Juwon Park, Sungjee Kim, Su-Moon Park, *Chem. Mater.*, **2010**, 22, 5636–5643.
11. Prakash Joshi, Lifeng Zhang, Daren Davoux, Zhengtao Zhu, David Galipeau, Hao Fong, Qiquan Qiao, *Energy Environ. Sci.*, **2010**, 3, 1507–1510.
12. Yuan-Lian Chen, Yi-Hao Chang, Jow-Lay Huang, Ingann Chen, Changshu Kuo, *J. Phys. Chem. C*, **2012**, 116, 3857–3865.
13. Yang Shengyuan, A. Sreekumaran Nair, Rajan Jose, Seeram Ramakrishna, *Energy Environ. Sci.*, **2010**, 3, 2010-2014.

Appendix – II

A Hybrid Photodetector based on ZnO Nanorods/Agarose Gel with Giant Response in UV-Visible

In this work, a novel photodetector design was conceived and demonstrated based on ZnO nanorods with surface dispensed agarose hydrogel which represents the concept of an ionic-electronic hybrid system. This ZnO-gel device showed a remarkable enhancement (about three orders of magnitude) in photocurrent as compared to bare ZnO nanorods. The observed giant enhancement in photo-response in ZnO / agarose gel device is explained on the basis of interface band bending and related effects.



Ref.: Lily Mandal, Meenal Deo et al. *Adv. Mater.* **2012**, *24*, 3686–3691

This work is primarily a part of the PhD thesis of Lily Mandal in view of the specific focus of her work. The author of this thesis has contributed to specific physical measurements in this work. Hence inclusion here as an Appendix.

ZnO nanorods were grown on transparent conducting substrate (FTO) by simple solvothermal method. The agarose gel was prepared by mixing agarose (2 wt %) in D. I. water by continuous stirring and boiling the solution on a hot plate. This solution was dispensed on the ZnO nanorods film. The gelation occurs directly on the film by cooling it to room temperature. X-ray diffraction and SEM showed that the ZnO nanorods are vertically oriented.

The device structures of ZnO-Pt and ZnO-agarose gel-Pt studied in this work are illustrated in Figures A-II (a) and (b), respectively. A FTO coated glass serves as the bottom electrode and a platinum tip acts as the top contact. Figures A-II (c) and (d) compare the I - V characteristics for the ZnO-Pt and the ZnO-gel-Pt systems under dark and under AM1.5 1 Sun illumination (100 mW/cm^2). In dark the slight non-linearity of the I - V curve in the case of ZnO-Pt interface indicates that the contact between ZnO and Pt is Schottky type. The presence of agarose gel modifies the characteristic, making it more rectifying. It can be seen that the current minimum occurs in between -1V to -2V in the dark, whereas under illumination it occurs at 0V . This shift can be attributed to formation of electrical double layer at the solid /quasi-liquid interface, which results in different capacitances at the interface in the dark. When this interface is illuminated high density of electrons and holes is generated which changes the interface charge distribution, thereby dramatically reducing the capacitances of the interface regions and shifting the current minimum to 0V . Since, the current minimum in the ZnO-gel-Pt occurs at around -2V , maximum photoresponse could be obtained for this bias.

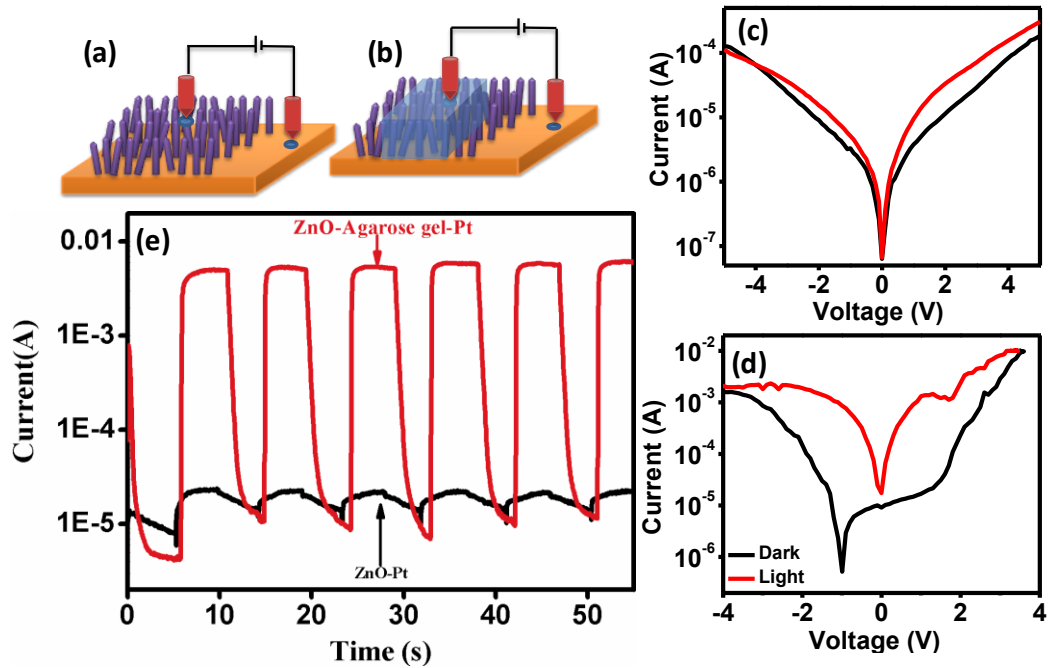


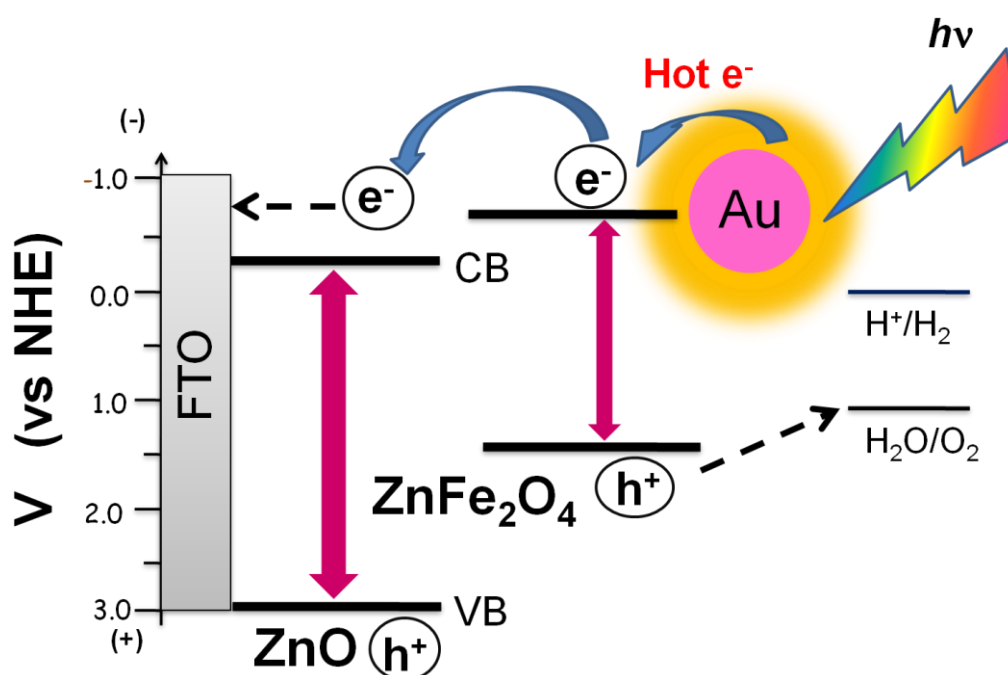
Figure A-II: The Device architecture of the (a) ZnO-Pt and (b) ZnO-gel-Pt systems; I - V under Dark and AM1.5 1 Sun illumination of (c) ZnO-Pt and (d) ZnO-gel-Pt systems and (e) Photoresponse as a function of time with visible light chopping

Figure A-II (e) shows the photocurrent response as function of time for the ZnO-Pt and ZnO-gel-Pt systems. The data represents the current at an applied voltage of -2V under chopped solar simulated light (AM1.5 1 Sun, 100 mW/cm^2) for 10 sec cycle. Upon illumination the current enhances by a factor of 2 in bare ZnO-nanorods case, while in ZnO nanorods-gel-Pt case it increases by almost three orders of magnitude. This remarkable difference is discussed at great length in the paper by Mandal et al. (*Adv. Mater.* **2012**, *24*, 3686–3691)

Appendix – III

Plasmonic Au / ZnFe₂O₄ / ZnO triple heterojunction photoanode for solar photo-electrochemical water splitting

For efficient solar photo-electrochemical water splitting, we have demonstrated a novel plasmonic triple heterojunction photoanode made up of Au / ZnFe₂O₄ (ZFO) / ZnO nanorods. We have observed drastic (factor of 5) photocurrent increment in Au/ZFO/ZnO junction as compared to only ZnO nanorods photoanode. This dramatic effect is attributed to near-field plasmonic enhancement induced by Au nanoparticles.



Ref.: A. Sheikh *et. al.*, *Small*, **2013**, 9, 2091–2096.

This work is primarily a part of the PhD thesis of Ashish Yengantiwar in view of the specific focus of his work. The author of this thesis has contributed to specific physical measurements and analysis in this work. Hence inclusion here as an Appendix.

ZnO nanorods (NR) were grown on FTO coated glass substrate by open aqueous solution deposition method. An ultrathin ZnFe_2O_4 (ZFO) layer was deposited on ZnO nanorods using pulsed laser deposition (PLD) technique. Further growth of Au NPs on the surface of ZFO/ZnO heterojunction was done using DC magnetron sputtering method. For this, Au metal target was sputtered in the Ar at a process pressure of 0.02 mbar at room temperature.

The photoelectrochemical (PEC) performance of pristine ZnO, the heterojunction of ZFO/ZnO and Au NP decorated ZFO/ZnO photoelectrodes, measured under 1.5 AM Sun (100 mW/cm^2) in an aqueous solution of 0.1 M sodium sulphate (Na_2SO_4) is presented in Figure A-III (a). The thickness of the ZFO film was optimized for maximum PEC performance, which was found to be 5 nm, before evaluation of the influence of Au on the ZFO/ZnO heterojunction. As can be seen from Figure A-III (a), the 5 nm ZFO/ZnO heterostructure provides a photocurrent density of 0.57 mA/cm^2 at an applied voltage of $0.8 \text{ V vs. Ag/AgCl}$. This is almost two times higher as compared to the pristine ZnO photoelectrode. This improvement is mainly attributed to the efficient charge separation at the ZFO/ZnO interface and most possibly the significant reduction in the recombination rate in ZnO due to passivation or elimination of the surface defects. Further, the triple junction of Au/ZFO/ZnO shows a dramatic enhancement of photocurrent density rendering $\sim 1.1 \text{ mA/cm}^2$ at $\sim 0.8 \text{ V vs. Ag/AgCl}$. This is almost five times higher than that for the only ZnO case and two times higher than that for the ZFO/ZnO heterojunction case without Au NP.

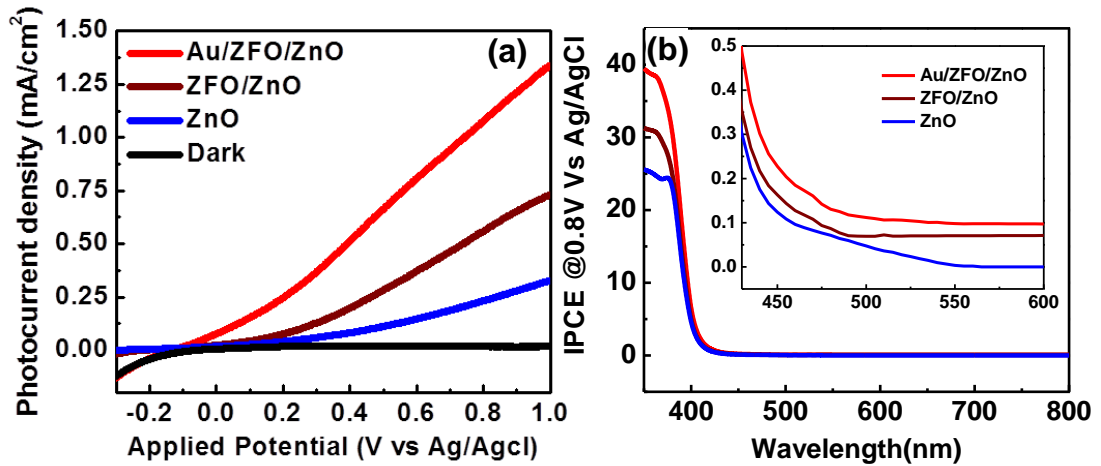


Figure A-III: (a) Photocurrent density (mA/cm²) vs applied potential of pristine ZnO, ZFO/ZnO and Au/ZFO/ZnO films; (b) IPCE data for pristine ZnO, ZFO/ZnO and Au/ZFO/ZnO samples at 0.8 V vs Ag/AgCl. Inset shows the IPCE data of same samples selectively in the visible range of the spectrum

Figure A-III (b) shows the IPCE spectrum of each electrode measured at 0.8 V in 0.1 M Na₂SO₄ under monochromatic illumination. In the case of pure ZnO, it can be seen that negligible photocurrent is generated in the visible region as expected; the small contribution can be due to the surface defects. The ZFO/ZnO and Au/ZFO/ZnO nanostructures are seen to exhibit a substantial progressive enhancement in IPCE. Interestingly, the enhancement effect is seen to be stronger in the UV region than the visible (see inset of Fig. A-III (b)). The enhancement in the UV region for the case of Au/ZFO/ZnO indicates the near-field optical enhancement effect of Au NP on the hetero-junction, which is discussed in detail in the paper by A. Sheikh *et. al.* (*Small*, **2013**, 9, 2091–2096).

List of Publications

- [1] “*From Dead Leaves to High Energy Density Supercapacitor*”, Mandakini Biswal, Abhik Banerjee, **Meenal Deo** and Satishchandra Ogale, **Energy Environ. Sci.**, 2013, 6, 1249-1259.
- [2] “*Near-Field Plasmonic Functionalization of Light Harvesting Oxide-Oxide Heterojunction for Efficient Solar Photochemical Water Splitting: The case of the Au NP / ZnFe₂O₄ / ZnO system*”, Arif Sheikh, Ashish Yengantiwar, **Meenal Deo**, Sarika Kelkar and Satishchandra Ogale, **Small**, 2013, 9, 2091–2096.
- [3] “*Cu₂O/ZnO hetero-nanobrush: hierarchical assembly, field emission and photocatalytic properties*”, **Meenal Deo**, Deodatta Shinde, Ashish Yengantiwar, Jyoti Jog, Beatrice Hannoyer, Xavier Sauvage, Mahendra More and Satishchandra Ogale, **Journal of Materials Chemistry**, 2012, 22, 17055.
- [4] “*A Quasi-Liquid Iontronic–Electronic Light-Harvesting Hybrid Photodetector with Giant Response*”, Lily Mandal, **Meenal Deo**, Ashish Yengantiwar, Arun Banpurkar, Jyoti Jog, and Satishchandra Ogale, **Advanced Materials** 2012, 24, 3686–3691.
- [5] “*Strong photo-response in a flip-chip nanowire p-Cu₂O/n-ZnO junction*”, **Meenal Deo**, Sarfraj Mujawar, Onkar Game, Ashish Yengantiwar, Arun Banpurkar, Sneha Kulkarni, Jyoti Jog and Satishchandra Ogale, **Nanoscale**, 2011, 3, 4706.

- [6] “*Enhanced dielectric permittivity in poly (vinylidene) fluoride/multiwalled carbon nanotubes nanocomposite thin films fabricated by pulsed laser deposition*”, Chetan Chanmal, **Meenal Deo**, Jyoti Jog, **Applied Surface Science** 2011, 258, 1256– 1260.
- [7] “*Strong electric field modulation of transport in PVDF/MWCNT nanocomposite near the percolation threshold*”, Chetan Chanmal, **Meenal Deo**, Abhimanyu Rana, Jyoti Jog, Satishchandra Ogale, **Solid State Communications**, 2011, 151, 1612–1615.
- [8] “*Enhanced nonvolatile resistive switching in dilutely Cobalt doped TiO_2* ”, Kashinath Bogle, Mukesh Bachhav, **Meenal Deo** and Satishchandra B. Ogale, **Applied Physics Letters**, 2009, 95, 203502.